Universidade do Minho
Escola de Engenharia

Francisco Tomé Ferreira Teixeira

Mechanical behavior of PA12 lattice structures produced by SLS

abril de 2021

UMinho | Francisco Tomé Ferreira Mechanical behavior of PA12 lattice structures produced by SLS

Universidade do Minho
Escola de Engenharia

Francisco Tomé Ferreira Teixeira

Mechanical behavior of PA12 lattice structures produced by SLS

Dissertação de Mestrado
Mestrado Integrado em Engenharia de Polímeros

Trabalho efetuado sob a orientação do(a):
Professor Doutor António José Vilela Pontes
Doutora Cátia Samanta Ribeiro da Silva

abril de 2021

DIREITOS DE AUTOR E CONDIÇÕES DE UTILIZAÇÃO DO TRABALHO POR TERCEIROS

ACKNOWLEDGEMENTS

The present dissertation was a great challenge to me, and I wouldn't be more grateful for the possibility to conclude my university career with the research of an interesting and promising technology labeled Additive Manufacturing. It was made possible thanks to several. For this purpose, I could not fail to express my gratitude to several people, in no specific order, who made it possible and accompanied me throughout this journey. With great respect and gratitude, I would like to thank:

- Pr. Dr. António J. Pontes, for his invaluable scientific guidance, support and all the patient, availability, advices and suggestions throughout this research;
- Dr. Cátia Silva and Msc. André Lima, for their continuously guidance and help to circumvent the encountered obstacles;
- To the DONE Lab, for allowing me to perform this research in its facilities;
- To the Department of Polymer Engineering of the University of Minho, for providing me full access to their labs to carry out some of the experimental work. To the technician Manuel Escourido, for the essential collaboration and help in compression tests;
- To the Polymer Engineering Innovation Center (PIEP), for providing me the realization of impact tests, specially, to Eng. Andreia Vilela for the essential help.

To conclude, my sincere gratitude goes to my family, especially my parents and brother, and friends for all the unconditional support during this journey.

STATEMENT OF INTEGRITY

I hereby declare having conducted this academic work with integrity. I confirm that I have not used plagiarism or any form of undue use of information or falsification of results along the process leading to its elaboration.

I further declare that I have fully acknowledged the Code of Ethical Conduct of the University of Minho.

ABSTRACT

Taking into account the rapid technological evolution and the growing demand, for the industrial sector to meet the most diverse needs of the market, Additive Manufacturing (AM) technology appears as a transformative approach to industrial production that enables the creation of lighter, stronger parts and systems. The versatility of this type of technology allows a reduction in production time and energy consumption, as well as, reducing material waste in the production of a product. It is in this last point that the technologies of AM stand out when comparing to the technologies of conventional manufacture. In AM technologies, it is possible to carry out the deposition of material in a controlled manner, where it is really necessary and, at the same time, ensure the necessary mechanical properties to meet the product requirements. Due to its versatility and rapid technological advances, it has become possible to implement typological optimization in AM. In this context, this study aims to investigate the mechanical behavior of lattice structures to support further investigations based on Topology Optimization (TO). The study of the mechanical behavior of these structures allows an intelligent distribution of these structures along a given structure in order to absorb the amount of energy needed for the impact, presenting competitive manufacturing times and costs.

In the course of this research, the manufacturing technique to be used will focus on the Powder Bed Fusion (PBF) process, more specifically in the EOS P396 equipment with the polymeric material polyamide 12 (PA12), that will shape the desired lattice structures, which are constituted by different topologies and volume fractions. The purpose of this development is focused on obtaining the experimental mechanical properties of certain types of cellular structures in order to compare them with the properties obtained from the simulations.

Thus, strut-based (BCC) and Triply Periodic Minimal Surfaces (Schwarz-P and Neovius) lattice structures were defined based on different independent variables, such as, cell size, strut diameter/ surface thickness and shell thickness. The defined structures were evaluated by compression and impact mechanical tests. It was found that beside geometrical design, the relative densities of the unit cells could also significantly influence the impact energy absorption performance.

KEYWORDS: Additive Manufacturing, Compression tests, Energy absorption, Impact tests, Lattice Structures, Lightweight, Selective Laser Sintering.

RESUMO

Tendo em conta a rápida evolução tecnológica e a crescente procura do sector industrial para satisfazer as mais diversas necessidades do mercado, as tecnologias de Fabrico Aditivo (FA) aparece como uma abordagem transformadora da produção industrial que permite a criação de peças e sistemas mais leves e fortes. A versatilidade deste tipo de tecnologia permite uma redução do tempo de produção e do consumo de energia, bem como a eliminação do desperdício de material na produção de um produto. É neste último ponto que as tecnologias de FA se destacam no que diz respeito às tecnologias de fabrico convencional. Nas tecnologias FA, é possível realizar a deposição de material de forma controlada, onde é realmente necessário, e ao mesmo tempo, garantir as propriedades mecânicas necessárias para satisfazer os requisitos do produto. Neste contexto, este estudo destina-se a investigar o comportamento mecânico de *lattice structures* para apoiar investigações posteriores que têm por base a Otimização Topológica (OT). O estudo do comportamento mecânico destas estruturas permite uma distribuição inteligente destas mesmas ao longo de uma determinada estrutura de forma a absorverem a quantidade de energia necessária ao impacto, apresentando tempos e custos de fabrico competitivos.

No decurso desta investigação, a técnica de fabrico a ser utilizada centrou-se no processo de *Powder Bed Fusion* (PBF), mais especificamente no equipamento EOS P396 com o material polimérico poliamida 12 (PA12), que dará forma às *lattice structures*, constituídas por diferentes células unitárias e frações de volume. O objetivo deste desenvolvimento focou-se na obtenção das propriedades mecânicas experimentais das estruturas celulares de maneira a compará-las com as propriedades obtidas a partir das simulações.

Assim, as *lattice structures* baseadas em *strut-based* (BCC) e *Triply Periodic Minimal Surface (TPMS)* (Schwarz-P e Neovius) foram definidas com base em diferentes variáveis independentes, tais como, tamanho da célula unitária, diâmetro da viga/ espessura da superfície e espessura da casca. As estruturas definidas foram avaliadas mecanicamente através de testes de compressão e impacto. Verificou-se assim que, para além do desenho geométrico, as densidades relativas das células unitárias também podiam influenciar significativamente o desempenho de absorção de energia de impacto.

PALAVRAS-CHAVE: Fabrico Aditivo, Ensaios de compressão, Energia absorvida, Ensaios de impacto, Estruturas de treliça, Peso reduzido, Sinterização Seletiva a Laser.

CONTENT

LIST OF FIGURES

LIST OF TABLES

LIST OF ABBREVIATIONS

Acrylonitrile Butadiene Styrene	**ABS**
Additive Manufacturing	**AM**
American Society for Testing and Materials	**ASTM**
Binder Jetting	**BJ**
Body Centered Cubic	**BCC / B**
Body Centered Cubic reference sample	**BR**
Body Centered Cubic shell thickness sample	**BS**
Body Centered Cubic surface thickness sample	**BT**
Carbon dioxide	**CO_2**
Cellular Structure	**CS**
Computer Aided Design	**CAD**
Computer Aided Engineering	**CAE**
Computer Aided Manufacturing	**CAM**
Continuous Digital Light Processing	**cDLP**
Differential Scanning Calorimetry	**DSC**
Digital Light Processing	**DLP**
Direct Energy Deposition	**DED**
Direct Metal Deposition	**DMD**
Direct Metal Laser Sintering	**DMLS**
Drop-On-Demand	**DOD**
Electron Bean Melting	**ELB**
Finite Element Analysis	**FEA**
Finite Element Method	**FEM**
Functionally Graded Materials	**FGM**
Fused Deposition Modeling	**FDM**
Fused Filament Fabrication	**FFF**
Laminated Object Manufacturing	**LOM**
Laser Engineered Net Shaping	**LENS**
Laser Metal Deposition	**LMD**
Lattice Structure	**LS**

Material Extrusion	**ME**
Material Jetting	**MJ**
Melting Temperature	**Tm**
Molecular weight	**Mw**
Multi Jetting Fusion	**MJF**
Nano Particle Jetting	**NPJ**
Neovius	**N**
Neovius reference sample	**NR**
Neovius shell thickness sample	**NS**
Neovius surface thickness sample	**NT**
Polyamide	**PA**
Polycarbonate	**PC**
Polylactic Acid	**PLA**
Powder Bed Fusion	**PBF**
Schwarz-P	**P**
Schwarz-P reference sample	**PR**
Schwarz-P shell thickness sample	**PS**
Schwarz-P surface thickness sample	**PT**
Scanning Electron Microscopy	**SEM**
Selective Laser Sintering	**SLS**
Sheet Lamination	**SL**
Stereolithography	**SLA**
Stereolithography file format	**STL**
Topology Optimization	**TO**
Triply Periodic Minimalistic Surfaces	**TPMS**
Ultrasonic Additive Manufacturing	**UAM**
Ultraviolet	**UV**
United Kingdom	**UK**
United States dollar	**USD**
United States of America	**USA**
Vat Photopolymerization	**VAT**
Three-dimension	**3D**

1. INTRODUCTION

1.1. CONTEXTUALIZATION

Over the last years, technology has transformed every industry, and manufacturers are only beginning to embrace the latest innovations. After overcoming several industrial revolutions, today we are going through the fourth industrial revolution (Industry 4.0), with innovations that can sense the health of equipment, augmented reality, and self-learning and self-healing machines. It leads to the digitalization era: everything is digital.

Since last decade, Additive Manufacturing (AM) technology has been improved rapidly to fulfil the needs of people and various industries. It is often bundled together with robotics, digitization and big data in the "Industry 4.0" vision of the factory of the future. An interesting fact about this technology, is that most of the general public is unaware that it has existed for several decades - the first commercial systems came on the market in the late 1980s. All its versatility, both in terms of processes and materials, allowed a rapid expansion in various industrial sectors, aiming in the near future to replace existing conventional manufacturing methods - standardization of technology.

The ability of freedom to design fully functional products, as well as the ecological/environmental advantage are intrinsic features of AM. However, the undesirable effects that reside in the control aspects of the process consider it a technology of low productivity, poor quality and uncertainty of the mechanical properties of the final parts. Optimization is difficult due to limited modelling approaches and the physical phenomena associated, such as melting/ solidification and vaporization, heat and mass transfer, are complex.

One of the main objectives of the industry is to maximize the performance of a given part, while minimizing its costs. One of these costs is related to the amount of material to be used to produce a part. Nowadays, the use of AM technologies has been more and more frequent due to its potential ability to produce any kind of shape, without any constraints. From here emerges a kind of bio-inspired configurations, based on repeating unit cells, composed by patterning webs or trusses that can, not only save material waste, but also, be self-supporting. These types of structures, commonly known as lattice structures (LS), can be automatically generated in a Computer Aid Design (CAD) systems. Even though they present high strength/low mass ratios by replacing solid material in parts, their prediction still presents several uncertainties, when it comes to shaping parts according to consumer requirements.

According to the potential of the LS, several experimental analyses of additive manufactured parts has been done to support the existing software tools to design and optimize cell structures, involving design considerations of each unit cell.

1.2. INTRODUCTION TO DONELAB

DONE Lab – Advanced Manufacturing of Product and Tools, is a laboratory created at the University of Minho in 2016. The laboratory emerged from a partnership between the University of Minho and Bosch Car Multimedia Portugal, aiming the research & innovation in the field of additive manufacturing, in order to give support to companies to enhance the innovation and time production of products.

1.3. OBJECTIVE

The outcome of this research paves the way for implementing additively manufactured cellular materials. It gives a solid foundation of an experimental analysis of additive manufactured lattice structures with diverse unit cell in compression and impact tests. For this purpose, different topological cellular structures with distinct cellular independent variables were produced from Polyamide 12 (PA 12) powder by implementing Selective Laser Sintering (SLS) technology. Thus, the aim of this investigation promotes the relationship between the specimen relative density value and energy absorption capacity.

1.4. ORGANIZATION OF THE RESEARCH

This dissertation is divided into six main chapters. **Chapter 1** presents a brief contextualization of the dissertation theme, its relevance, and the description of its objective. **Chapter 2** presents a brief description of the history of AM and, its main principles and technologies. It is also described, in more detail, the SLS process used in the fabrication of the samples. Also, basic lattice concepts are presented, including a succinct description of the different topologies. This introductory detailed section presents some general background, in order to allow an easier and better understanding of the other topics covered. **Chapter 3** describes the methodology carried out for the design, shape definition and overall dimensions, material, and process parameters for the production of the cellular samples. The experimental procedure of compressive and impact tests, for the characterization of samples, is also described in this chapter. **Chapter 4** present the analysis and data treatment of the obtained experimental results. In conclusion, **Chapters 5** and **6** cover the conclusion marks and further research to improve AM technology, respectively.

2.LITERATURE REVIEW

The present chapter describes some fundamental concepts in order to facilitate the understanding of the present dissertation. It starts by briefly reporting the history of the AM, presenting, in the following, the various processes attached to it. At another point, a more detailed presentation of the SLS technique is made. Finally, with a greater focus of interest, the section related to lattice structures appears, where the theoretical basis for the prediction of properties are described.

2.1. HISTORY OF ADDITIVE MANUFACTURING

Despite the little use and, consequently, lack of knowledge of AM, this technology has been around for nearly 40 years [1]. Its roots lie in new patterns of consumption and use of products resultant from the second industrial revolution. From here, comes the concept of rapid prototyping, opening doors to the AM technology. Despite their similarities, they present small differences in terms of price, complexity of the printing method, material choices and precision. That said, AM makes reference to any manufacturing technology that uses layer-by-layer deposition and Rapid Prototyping is an application used in the AM [2] [3].

A historical analysis reveals that the first attempt to implement the AM was from topography and photosculpture [4], [5]. The first one consisted of cutting the wax plates along the topographical contour lines firstly, and then, stacking and smoothing these plates in order to produce three-dimensional part. This part corresponds to the terrain indicated by the contour lines. The second one related to the "intersection of two laser beams of differing wavelength in the middle of a vat of resin, attempting to polymerize the material at the point of intersection", that led to appearing of the first commercial SLS printer, in 1990 [5], [6].

During the first decade of 2000, AM technology was seen as a potential fast manufacturing method for very limited purposes as, for example, in the jewelry field, for small quantities of production and with small size parts. That is, it was seen as an auxiliary manufacture technique to the production lines. From 2010 onward, AM began to have its due value where some industries adopted AM technologies as their main method of manufacture. The first companies that adopted this kind of manufacturing system were the in-the ear hearing aids, in 2011. With more complexity applications, such as dental, biomedical and aerospace companies also began to embark in the same way. Simultaneously, metals AM processing technologies also had a significant interest and growth [6] [7].

Nowadays, the evolution of AM is due to the creation of new companies, with interest of companies already implemented in the market, with the creation of the most diversified 3D printers, as well as, with the development of new materials. This constant effort and dedication have enhanced AM to acquire an increasing importance in the most diverse areas from the automotive to the food industry. Considering the technological advances in recent years, the AM success is in constant growth at the industrial market level [3], [6].

2.2. INTRODUCTION TO ADDITIVE MANUFACTURING

The way products are designed, manufactured and distributed to end users is changing by the potentially of AM technology. Additive Manufacturing is a general term, encompassing a wide variety of systems used to create three-dimensional physical parts and models, directly from digital data [8]. American Society for Testing and Materials (ASTM) defined this bottom-up process as "a process of joining materials to make parts from 3D model data, usually layer upon layer, as opposed to subtractive manufacturing and formative manufacturing methodologies" [9]. The term 3D printing is mostly used as a synonym for AM but there are also other, not so frequent, historical terms, such as, additive fabrication, additive processes, additive techniques, additive layer manufacturing, layer manufacturing, solid freeform fabrication, and freeform fabrication [5], [10], [11].

Succinctly, AM processes are based on the fabrication of parts, by creating successive cross-sectional layers, of an object. As showed in Figure 1, AM process begins with a three-dimensional (3D) solid model, which is initially modeled or scanned as a Digital Computer Aided Design (CAD) file, and then sliced into thousands of layers by preparation software as Standard Tessellation Language (STL) file. Finally, each layer is created via the selective deposition of material and/or energy to fuse the raw material to produce a printed part [4], [10]. With the usage of customized material properties, it permits manufacturing intricate and complex shapes much more simply than conventional methods, providing the potential to reduce production costs, energy consumption, and, consequently, ecological footprint [12]. Parts can also be built from 3D imaging data generated by 3D scanning or medical imaging devices. Materials used in AM are broadly classified as liquid, powder, filament or sheets. Polymers were the primary type of materials used in additive manufacturing, but plaster, metals, silica sand, paper, ceramics and biological materials, are also available in AM [13] [14]. AM systems range from large industrial machines, suitable for shop floor and laboratory environments, to smaller desktop printers [12]. Nowadays, this technology counts with several different processes including vat polymerization, powder bed fusion, material extrusion and material jetting as the most popular ones [9], [15].

Although AM has been in use for decades, new advancements and applications are being developed every day [4], [16], [17].

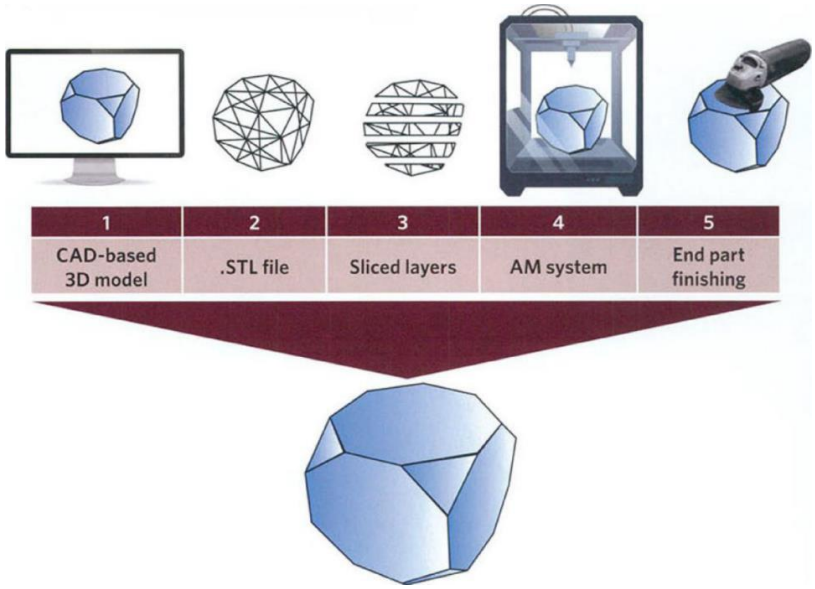

Figure 1 – AM process flow [18].

2.2.1. Processes

Due to the identical procedure presented by the different AM processes, it is wrong, but common, to assign the term AM to all the processes involved.

Throughout the history of AM, the constant and successive development of new processes and materials has forced certain researchers to rethink how to classify them. In order to choose the process that best suits a given application, several classifications have been released [19]. The task was not easy because each process offers variations in dimensional accuracy, surface finish and post-processing requirements. Over the past few, the American Society for Testing and Materials (ASTM) committee ASTM F42 – Additive Manufacturing has been formed to come up with terminology and standards that help grow the industry and let different stakeholders talk to each other on the same terms. In 2010, it formulated a set of standards that classify the range of Additive Manufacturing processes into 7 categories such as Vat Photopolymerization, Powder Bed Fusion, Material Extrusion, Material Jetting, Binder Jetting, Direct Energy Deposition and Sheet Lamination. This classification is based on the type of material to be used, on the machine technology and on the expected functions [1].

2.2.2. Materials

As stated in the previous point, the choice of the appropriate material is related to the type of process to use [20]. For a material to be reliable to any AM technology, it must include the ability to produce the raw material in a manner compatible with the specific AM process, adequate processing of the material through AM, the ability to be post-processed to improve geometry and properties, and manifestation of the performance characteristics required in service [14]. In general, a specific material class is associated with a certain technology and application.

Initially, AM was implemented with the intention of producing plastic products, regardless of the process to be used [15]. Over intense years of research and development, AM has begun to embark on new paths, capable of producing complex parts using other materials. Actually, a wide range of materials that can be used in AM include a diversity of polymers, ceramics, metals, and composites can be used for AM [8]. Materials can be found in liquid, filament, powder and solid sheet states, depending on the process in question.

A polymer is a large molecule made up of chains or rings of linked repeating subunits, which are called monomers. Polymers tend to have high molecular masses due to the join of many monomers. The versatility, adaptability and properties makes polymers the most used class of materials in AM [21].

Among the currently commercial materials, Table 1 shows that material extrusion processes use, in majority, amorphous polymers but also semi-crystalline, those of vat photopolymerization are limited to photosensitive thermosets, material jetting typically uses photosensitive thermoset polymers, powder bed fusion is mostly limited to semi-crystalline polymers, metal powder bed fusion uses metal alloys that are suitable in casting or welding, while binder jetting and some sheet lamination use practically any raw material as long as it can be converted into powder or foil and, finally, Directed energy deposition resources to metallic powder or wire feedstock [14].

Table 1 – Current commercial materials directly processed by AM [14].

	Amorphous	Semi-crystalline	Thermoset	Material extrusion	Vat polymerization	Material jetting	Powder bed fusion	Binder jetting	Sheet lamination	Direct energy deposition
ABS	X			X						
PC	X			X						
PC/ABS Blend	X			X						
PLA	X			X						
Polyetherimide (PEI)	X			X						
Acrylics			X		X	X				
Acrylates			X		X	X				
Epoxies			X		X	X				
PA (Nylon) 11 and 12		X					X			
Polystryrene (PS)	X						X			
Polypropylene (PP)		X					X			
Polyester (“Flex”)							X			

Polyetheretherkeyton e (PEEK)	X	X	X			
Thermoplastic polyurethane		X	X			
Chocolate	X	X				
Paper					X	
Aluminium alloys			X	X	X	X
Co-Cr alloys			X	X		X
Gold			X			
Nickel alloys			X	X		X
Silver			X			
Stainless steel			X	X	X	X
Titanium, comercial purity			X	X	X	X
Ti – 6Al – 4V			X	X	X	X
Tool steel			X	X		X

2.2.3. Applications of Additive Manufacturing

At the start of this new manufacturing ideology, AM began to be applied in the area of rapid prototyping and then tooling [20]. With the progressive development of innovation, AM has been able to make positive progress in the latter and thus, attract greater attention from the most diverse industrial sectors. The parts that were previously produced as prototypes are, nowadays, produced as final products.

In the aerospace sector, in which it needs to produce highly complex aviation components from advanced materials, is one of the examples of its application [22], [23]. In this area, complex additive manufacturing processes must be developed to meet the industry's stringent requirements and to ensure the robust performance of parts, comparing to traditional manufacturing methods [24], [25]. Another milestone in the AM was when NASA launched the first 3D printer in International Space Station to experiment printing parts in zero gravity [3]. In the automotive sector, although AM is limited to the production of end-use parts, in low volume, for luxury or racing vehicles, it is a source of cost savings when it comes to industrial production. Due to the fact that this sector is constantly changing, the development of a new product is critical. For this, the work in AM is fundamental because it reduces cycle times, and production and product costs, when a visual analysis or quality control is intended [26].

In the medical sector, the parallel development of biomaterials has provided the development and expansion of certain AM processes. Its application, with promising expansion, is now present in the customization of, for example, implants, prostheses and organ replacement [27]–[29].

With the current environmental concern to reduce CO_2 emissions and consumption of natural resources, there are ample opportunities in the energy sector where AM can be crucial. In highlight is the rapid production of prototypes to reduce the cost and lead-time of research and the development of new products. Adding to this, the energy efficiency and power density can be explored by creating newer prototypes [30], [31]. In the architecture sector, the use of AM facilitates the construction of models, of complex ideas difficult to reproduce on paper [32].

Among other sectors where AM is an asset, it is an ideal technology in the repositioning of spare parts, craft and hobby items, educational uses, unique requirements and fashion accessories [33]. When it is intended to make a product for a particular application, not all AM processes are able to perform it. Therefore, depending on the application in question, the AM process that best meets the desired needs is chosen.

Regardless of the sector in which AM technology is applied, its overview will always be seen from a planning, simulation and evolution perspective, until the day it is fully implemented in the industrial production lines.

2.2.4. Advantages vs drawbacks

With the usage of AM technology, development has become easier than ever before. Nowadays, any project can be manufactured using nothing but a 3D printer and the desired raw material [34].

This has paved the way for customized products as it allows the creation of fully customized 3D-designs by simply modifying the 3D model in the software and get them printed by a time and cost efficiency production. Instead of traditional manufacturing methodologies, such as, conventional injection molding or machining/subtractive technologies, the AM dramatically reduces or completely avoid the use of tools, reducing the speed and the cost of end-use parts productions. AM allows the fabrication of complex geometries, with high precision, efficient material usage, design flexibility, and also the production of customized products according to any requirement of the consumer. It may even generate new employment opportunities [8], [21], [32], [35]. When comparing to injection molding production, it is estimated that AM methods are most cost-effective for targeted fabrications runs ranging from 50 to 5000 units [36]. In comparison with machining technologies, although the waste associated with AM is low, a significant percentage of it is still recyclable [10]. The development of production processes, the AM technologies can be a potential to support environmental sustainability in the manufacturing field [37].

Without exception to existing technologies, AM also has certain disadvantages which have been counteracted by successive investigations. It presents higher costs for large production runs and in materials, size restrictions, poor surface finish and accuracy, and needs software improvement for standardization [4], [32], [38].

2.2.5. Main future issues

The rise of AM is making a significant impact on how parts and products are designed and manufactured. It is also directed by the part geometry and application need. Despite its great development over the last few years, its implementation in industries is still not fully accepted.

In the near future, AM's main goals will be to reduce machine, material and maintenance costs. So that, the change of conventional manufacture by AM is possible with the enlargement, development and identification of applications exclusively for its use [39]. To achieve these goals, AM technology and its applications require significant further research and development in terms of designs, materials, new processes and machines, process modeling, process control, bio-additive manufacturing, and energy and sustainability applications, as well as, the improvement of certain processing parameters of existing technologies [8], [15].

The advantages that AM claims to differentiate itself from traditional manufacturing need further research for it to become a more practical alternative, but the new research towards these developments is slow due to the interfaces of research laboratories and commercial machine manufacturers gaps between academia and industrial settings.

2.3. AM TECHNIQUES

Through extensive research over the past years, significant progress has been made

in the development of new AM technologies. In the early 1990s, Kruth starts to categorize additive manufacturing techniques from liquid-based, powder-based and solid-based systems according to different material creation. And direct-3D and 2D-layers techniques according to different shape building [19]. Most recently, ASTM F42 committee has classified AM techniques into seven different categories. This section begins by briefly describing the different existing techniques, ending with a more thorough approach to the technology used in this research: SLS.

2.3.1. Vat photopolymerization (VAT)

Vat-photopolymerization consists in a process of taking a vat of photosensitive resin and then, curing that resin through selective exposure to, usually, UV light range. A laser or light source generates a UV beam that cures focused surface areas point-by-point or layer-by-layer. In either case, it initiates with the polymerization to create the desired part, in a layer-by-layer fashion on a top-down construction platform (Figure 2). The materials are photocurable epoxy or acrylate resins. Ceramics or metals are not suitable. High accuracy, flexibility for the production of small and large parts and smooth surface finish are some of its advantages [21], [40], [41].

Some commercialized technologies are Stereolithography (SLA), Digital Light Processing (DLP) and Continuous Digital Light Processing (cDLP) as direct technologies [13].

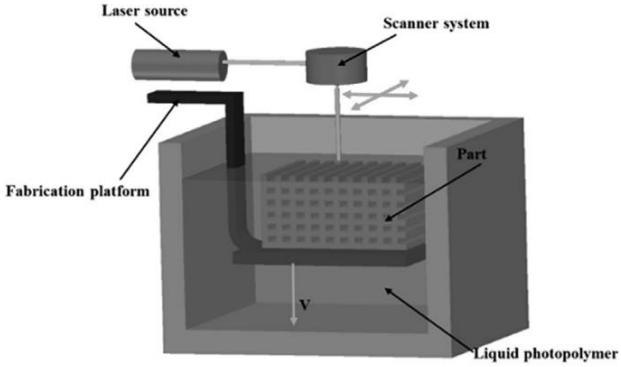

Figure 2 - VAT polymerization AM technology [40].

2.3.2. Powder Bed Fusion (PBF)

All PBF technologies use the same basic techniques to manufacture parts layer-by-layer. It starts by spreading a thin layer of powder across the building platform using a counter rotating levelling roller or a blade. The powder material is delivered by feed cartridges. Then, a heat source, moved by two mirror galvanometers, is focused on some powdered material on a build surface to selectively heat layers in the cross sections of a part, according to a digital design (Figure 3) [42]. The most common heat source is a laser. However, electron beams or infrared heaters may also be employed. Once a cross-section has been traced onto the powder, the build platform moves down by the height of one layer and the next layer is scanned. This lowering and scanning process is repeated until the whole part has been manufactured. Finally, once it has cooled and been taken out of the build chamber, any excess powder is removed The whole build chamber is sealed and filled with the protective inert gas to prevent the powder degrading.[13], [20].

PBF systems use polymers, ceramics, metals or composites. In addition, powder bed systems are being used to directly manufacture end use parts, rather than just prototypes. With this technic, the processing technology are Direct Metal Laser Sintering (DMLS), Multi Jetting Fusion (MJF), Selective Laser Sintering (SLS) and Electron Bean Melting (ELB) [15]. This research will use SLS techniques to fabricate the lattice structures for experimental testing. The report about the experimental tests provides a more profound explanation of the technology and strategies.

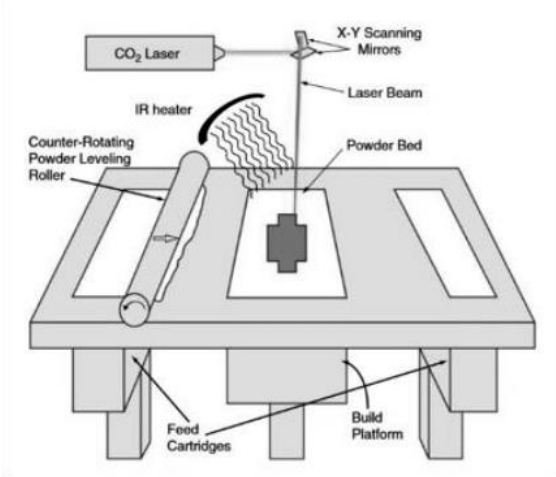

Figure 3 -Powder Bed Fusion AM technology [13]

2.3.3. Binder Jetting (BJ)

Binder Jetting (BJ) technique starts by spreading a powder layer of a specific thickness and then, a liquid binder is selectively deposited on a powder bed to produce a part. This liquid bonding agent join or 'glue' the powder particles at the desired locations (Figure 4). The binder agents are, usually, polymers and the powder can be ceramics, polymers or metals [42]. Its benefits are the production of fairly multi-color accurate parts and it can manufacture very large and complex parts, which are not limited by any thermal effects (e.g. warping) [43]. In terms of limitations, produced parts achieve lower mechanical properties, due to their higher porosity. Furthermore, resulting parts are not always suitable for structural parts due to the use of binder material [13].

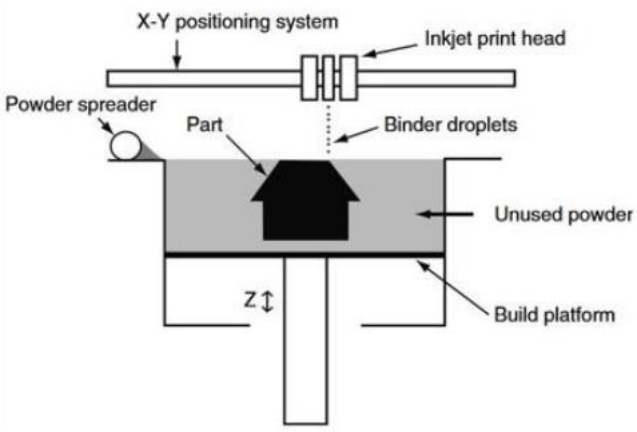

Figure 4 - Binder Jetting AM technology [13]

2.3.4. Material Jetting (MJ)

Material jetting AM processes are similar to the inkjet 2D printing process, in which ink UV curable or hardened droplets are transferred from the fluid channel onto the paper substrate in a drop-by-drop manner [44]. In this process, photopolymers, metals or wax droplets are directly deposited layer-by-layer. Undesired droplets are deflected by a charging field and recycled. The process is comparable to a simple paper print system (Figure 5). This technology includes Material Jetting (MJ), Nano Particle Jetting (NPJ) and Drop-On-Demand (DOD) sub-processes [45]–[47]. PolyJet is a famous technology using this technique. Fabricated parts have a smooth surface and dimensional accuracy, but the investment is very costly [17], [42].

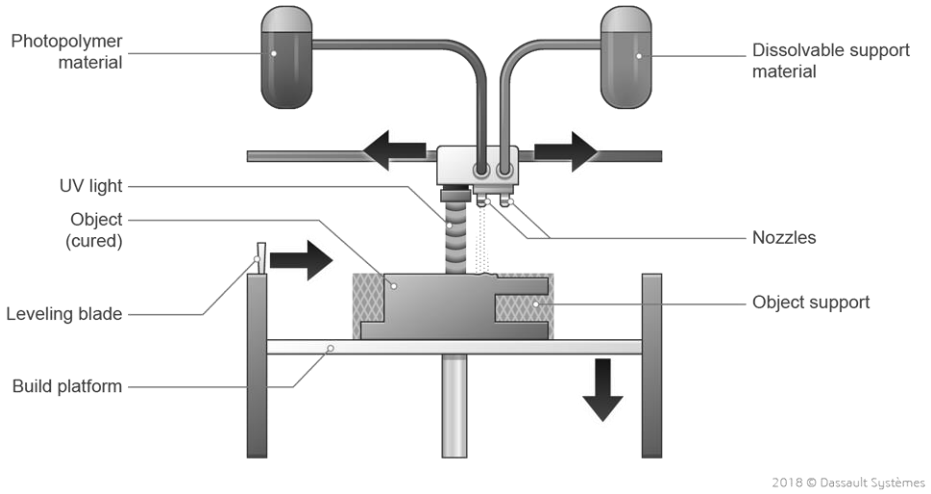

Figure 5 - Material Jetting AM technology [48].

2.3.5. Sheet Lamination (SL)

Sheet Lamination (SL) technology includes Ultrasonic Additive Manufacturing (UAM) and Laminated Object Manufacturing (LOM) processes. The procedure of this technology focuses on the same principle for both processes, with differences in the material and the type of bond between layers. UAM uses the ultrasonic welding between metal sheets and LOM uses paper or composite as material and adhesive as bonding [13], [49]. Two approaches are possible: form-then-bond or bond-then-form. In the former, the laminate is first cut to shape and later bonded with the underlying laminate. The latter approach follows the opposite sequence. The laminate is placed on the previous layer and glued together. Then a knife or laser cuts the laminate according to the slice contour (Figure 6) [50]. SL can provide unique opportunities for the

manufacturing of multiple materials structures, fiber embedment during manufacture, and embedding of electronics and other features to form smart structures [51], [52].

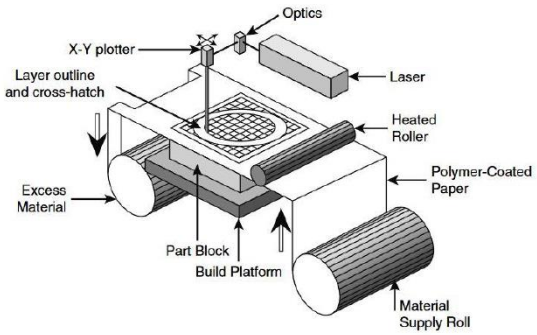

Figure 6 - Sheet Lamination AM technology [13].

2.3.6. Material Extrusion (ME)

Material extrusion technology starts by the load and melt of the filament, inside a heated nozzle channel, to a temperature slightly above its melting point. Similar to a hot melt glue gun, uncoiled and pressurized material is slowly extruded through a heated nozzle at a constant flow rate. The extruder head is typically carried on a plotting system that allows movement in the horizontal plane to make 2D contours. A layer is formed by printing a series of contours. The build platform moves down until either prototype or end use parts are produced (Figure 7) [8], [15]. The technique is also known as Fused Filament Fabrication (FFF). This is a very low-cost technology commercialized under the name Fused Deposition Modeling (FDM). The popular low-budget 3D printers operate according to this principle [1]. The main drawback is weak dimensional accuracy [53].

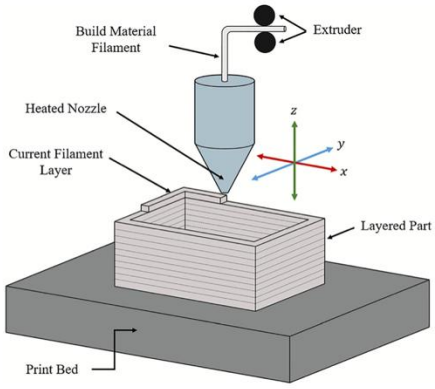

Figure 7 -Material Extrusion AM technology [54].

2.3.7. Direct energy deposition (DED)

DED technique enables the creation of parts by melting and depositing material from powder or wire feedstock [8]. According to the type of mechanism in use, both the feed nozzle and the heat source can be coupled or not, but they are always mounted on the same gantry system or robotic arm (Figure 8). Although this approach can work for various materials, it is predominately used for metal powders. The focused energy can be either a laser, electron beam or plasma arc [4]. It can also be referred to as Laser Metal Deposition (LMD), Laser Engineered Net Shaping (LENS), Direct Metal Deposition (DMD), or laser cladding [15]. Its use is advantageous for repairs and production of large components. However, complexity and dimensional accuracy of the parts are limited, which causes poor surface finish [8].

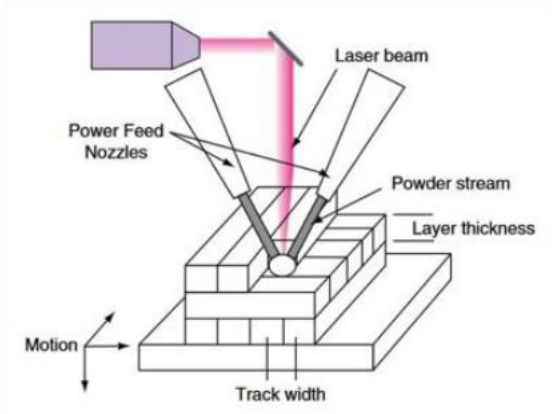

Figure 8 -Direct Energy Deposition AM technology [13].

2.4. POWDER BED FUSION – SLS

Previously, in section 2.3.2, the basic operating principle of PBF technology was described, as well as its surrounding processes. This section describes, in more detail, one of its processes, the SLS technology. Throughout it several topics will be reported, starting with a short introduction to the technology. It will be followed by topics describing the technology, parameters, materials and the recycling of matter. At the end, the advantages and disadvantages of this process are presented, as well as, the description of the applications that most use this technique.

2.4.1. Introduction

Some of the earliest AM systems were based on laser technology that uses the laser processing, as curing or heating, to cause the solidification of the liquid resin, or cure, and to cause powder melting or cut through a layer, respectively [55]. The SLS technology, developed by Carl Deckard and Joe Beaman at the University of Texas at Austin's Department of Mechanical Engineering, was the first commercialized powder bed fusion process, in 1986. Some years later, in 1989, the potential of SLS technology has been driven by the DTM Corporation of USA and the Electro Optical Systems (EOS GmbH) of Germany [13], [55], [56]. The overall SLS equipment market, inclusive of equipment and material, is expected to grow from USD 339.5 million in 2018 to USD 947.4 million by 2023, at a compound annual growth rate of 22.8% during 2018 – 2023 [57].

Although the basic working principle of PBF processes is the same for every technique, each one has been individually changed in order to improve its productivity. The expansion of the quantity of powder materials available for AM was one of the main drivers of these changes [13].

As showed in Figure 9, an SLS printer consists of a camera, two powder feed tanks, a device that successively spreads and flattens the powder layers, a construction platform and a laser coupled to an optical system (scanning mirror capable of sintering the powder particles). In terms of production yields, this technology is ideal for the production of small to medium quantities of highly complex parts [58].

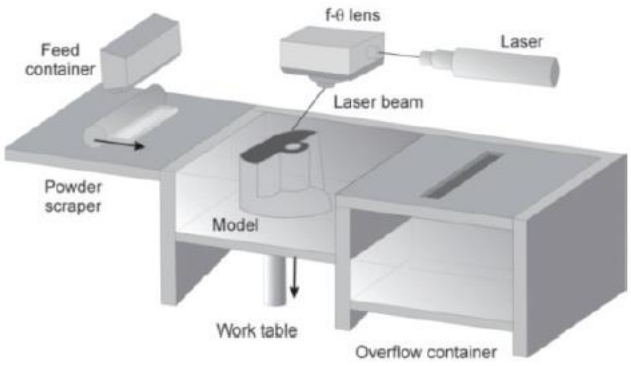

Figure 9 – Representation of SLS process [59].

2.4.2. Technology

SLS is a powder-based thermal 3D printing manufacturing process that uses thin layers in the order of one-tenth of a millimeter thick [13]. It uses a laser to sinter or melt layers of powder to grow the part.

It starts with the integration of a 3D CAD file to create 2D slices. The entire build area is heated up too close to the melting temperature of the material, and then, there's a laser that actually melts thermally the powder where the 3D CAD file want to the solid part be. This warmup is achieved due to the presence of infrared heaters, above the building platform and above the feed tanks, to minimize and prevent the deformation of the part due to non-uniform thermal expansion. The sintering occurs due to physico-chemical reaction [13], [60]. The atmosphere of the chamber is composed by an inert gas, typically nitrogen, in order to minimize oxidation and degradation of the powdered material. The build platform drops down as each layer is grown and the new layer of powder is added on top. This procedure is performed repeatedly until the solid part is obtained. The end of the process is a cooling period, proportional to the sintered volume. This prevent powder degradation when exposed to the atmosphere (oxygen), and possible warping due to uneven thermal contraction [61]. Parts and involving non-sintered powder can only be removed after reaching glass transition temperature or below 45 – 60 ºC. Since the raw material is polymeric, the non-sintered material is easily brushed away and parts can be excavated like an archeology dig. Optionally, parts can go through a custom post-processing phase, such as painting, sanding or surface finishing, depending on the customer's requirements or needs, or the application. There are varied options after that part comes out of the machine [62]. The process explained above is summarized in Figure 10.

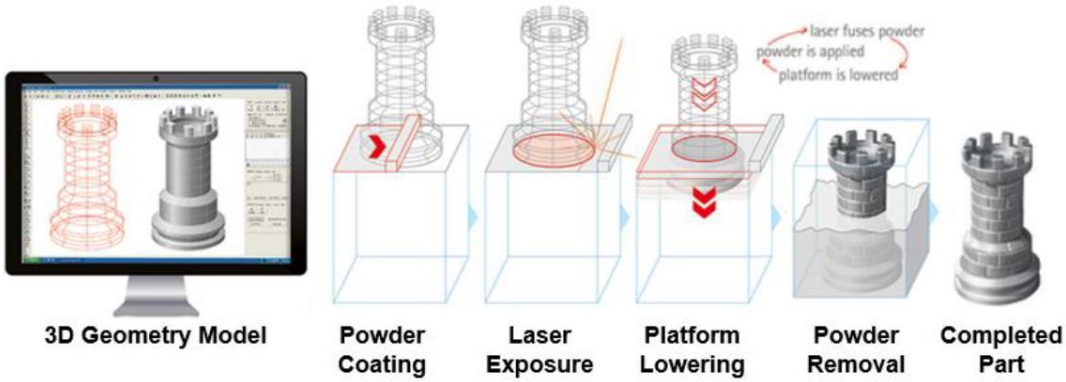

Figure 10 - SLS process sequence [63].

2.4.3. Process parameters

Parts' accuracy in SLS can arise from a strongly independent parameters that can be controlled and varied for a particular application. Thus, they can be classified into (1) powder-related parameters (particle shape, size and distribution, powder bed density, layer thickness, material properties); (2) laser-related parameters (laser power, spot size, pulse duration, pulse frequency); (3) temperature-related parameters (powder bed temperature, powder feeder temperature, temperature uniformity); (4) scan-related parameters (scan speed, scan spacing, and scan pattern); and (5) part parameters (part orientation, part position) [13], [64].

(i) Powder parameters

Powder parameters can be divided into several factors that are interrelated. The different properties of SLS powders can be divided into intrinsic (e.g., thermal, optical and rheology) and extrinsic ones (particle and powder). Intrinsic properties are typically determined from the molecular structure of the polymer itself and cannot be influenced easily, whereas production of powder controls extrinsic properties [65]. These characteristics play a significant role in powder performance that compromises the performance of the final product [66].

Since the powder is distributed by roller or blade systems, the particles should have spherical form to induce a free flowing behavior and the powdered raw material formed by these particles must have a certain particle size distribution. Thus, the potato shaped particle and the distribution from 20 µm to 80 µm are the most commonly used for commercial PA 12 powder [65], [67].

The irregular and random packing of particles forms the porosity. It tends to be larger on the surface of the layer, than inside the part, and increases with the decrease of the laser energy due to the incomplete fusion of the particles.

Regarding the molecular weight, M_w, of the powder, there is a suitable optimum range. Polymers with high M_w allow to obtain functionally strong parts. However, they can lead to difficulty in spread the powder because of high viscosities, but can reduce shrinkage and, consequently, improving dimensional accuracy [68].

Coupled with the M_w is the density of the powder. Powder densities generally range from 50% to 60%, for most commercially available powders. Generally, the higher the powder packing density, the better the mechanical properties of the part [69].

The layer thickness is another important parameter. Its decrease results in more time part processing. The increase in layer thickness beyond limits results in an increase of the stair

stepping problem, poor sintering, rougher surfaces on parts and the part cannot be produced properly. To ensure that the powder fusion occurs at direct contact of the laser on the particle, the layer thickness is recommended to be at least two times the average size of the particle [69], [70].

(ii) Laser/ temperature parameters

Similar to laser cutting and laser welding, SLS uses a linearly traversing laser beam to selectively fuse powder particles. All the laser irradiation incident with the powder surface is assumed to be absorbed or reflected according to the optical properties of the powder. So, there must be a balance between the laser power and the bed temperature [71].

High laser power and bed temperature produce dense parts with a partial growth, poor recycling and difficulty in cleaning. For low laser power and bed temperature, the dimensional accuracy of the produced parts is improved but it results in lower density parts with a great tendency for layer delamination. High laser power combined with low bed temperature have a tendency for non-uniform shrinkage and accumulation of residual stresses [13]. Increasing the laser power incident in the powder can fabricate higher strength parts. This increase is made until the thermal degradation of the powder [69]. Relatively to bed temperature, it is increased as high as possible but, $3^{o}C - 4^{o}C$ below the melting temperature of the powder for semi-crystalline polymers. This increase is also good for reducing consumption of energy due to the need of lower laser power, but it can result in an unwanted binding [13], [72]. The desirable re-crystallization of the powder occurs at low bed temperatures, but at very low bed temperatures, the mechanical properties are poor due to non-uniform fusion of powder particles and increased porosity [73].

In order to find the suitable operating window of the LS process, the distance between the melting and crystallization peaks of the Differential Scanning Calorimetry (DSC) peaks can be used to indicate it. The distance between the melt and recrystallization peaks is the processing window for the bed where the corresponding area promotes good control of sintering when the powder absorbs energy from the laser and allows effective part consolidation by avoiding premature crystallization on cooling [74].

(iii) Scan parameter

Scan spacing or hatch spacing is the distance between parallel laser scans. Scan spacing has a significant effect on all mechanical properties, such as, ultimate tensile strength, elongation, yield strength, and Young's modulus. That is, for shorter distances are required high laser energy, resulting in over sintering. However, too large scan distance results in incomplete sintered cross-section. As stated by S. Singh et al., scan spacing is proportional to the energy density used [69].

Scan speed is a process parameter that controls the part build time and is directly related with the laser power. A higher scanning speed decreases the degree of melting of the particles as the particles do not have enough time to melt. Lower scanning speed can degrade the particles. At these scan speeds, laser power has limited effect on sinter width. If power applied is less, no binding reaction occurs, and melting could not take place properly. Having said this, there must be a balance between the scanning speed and laser power for a correct part production [75].

(iv) Part parameters

The orientation of the part is an important parameter that describes the rotation of the part, in the build space, around the axes of the machine's coordinate system [76]. It is an important parameter due to its influence not only on the resulting surface quality but also on stair stepping effect. Also, the accuracy of part's details and the building time and costs, due to the building height, are strongly influenced by the build orientation. Research conducted by Ajoku et al. [77] found that parts built parallel to the layer orientation (0°) had better tensile properties than parts built perpendicular to layer orientation (90°). Another research made by Caulfield et al. [78] found similar results where the perpendicular orientation resulted in a better geometric accuracy but in a lower density, yield strength, tensile modulus, and fracture strength than the parallel oriented parts (Figure 11).

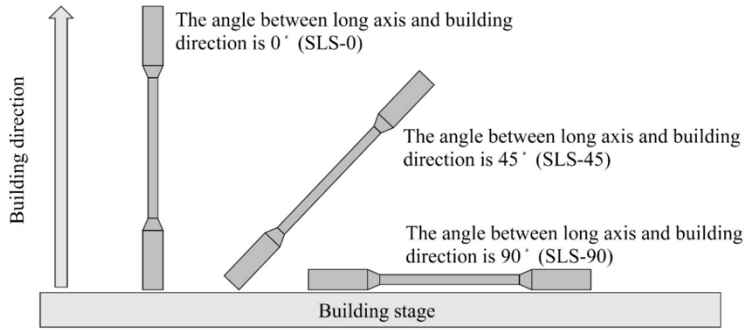

Figure 11 - Building direction of SLS parts [79].

2.4.4. Materials

SLS technology starts with the usage of polymers due to their ability to be easily processed by melting, and their good mechanical properties. PC was initially used as the starting materials for both experimentation and modeling in SLS [64]. With the progressive development of this technology, the approach applied to this process with polymer powders was, posteriorly, extended to metal-polymer powders, where the polymer acts as a binder, metal and ceramics [80].

Within the existing types of polymers, SLS technology mostly uses thermoplastics. Depending on the use of amorphous or semi-crystalline thermoplastics, these determine the SLS manufacturing parameters and limit the purpose of the parts produced. Amorphous polymers, like PC powders, are able to produce parts with very good dimensional accuracy, feature resolution and surface finish (depending on the grain size). However, they are only partially consolidated. As a consequence, these parts are only useful for applications that do not require part strength and durability. Semi-crystalline polymers, like nylons (e.g. PA12), on the contrary, can be sintered to fully dense parts with mechanical properties that approximate those of injection molded parts. The good mechanical properties of these nylon-based parts make them particularly suited for high strength functional prototypes [81].

According to the specific properties of PA12, its use, as well as the mixtures it provides, is quite attractive. It exhibits good resistance to solvents, high strength and wear resistance. PA12 based powders, including PA2200 supplied by EOS GmbH, appears as the most used materials in laser sintering process for rapid manufacturing of functional parts [62].

2.4.5. Recycling of material

An average of 10% – 20% of the powdered material in the LS building chamber is sintered and could be reused. However, the powder properties deteriorate along the builds, which ultimately affects the quality of produced parts. These differences are due to the process conditions, such as, temperature and time, the LS machine design, and properties of the powder used for parts fabrication [62].

A standard technique of material recycling is to mix the recycled powder collected from previous builds with new powder and use it in the next build. The part quality is dependent on the input material properties and powder management. The older the material is, the newer material is required and vice versa. However, it is impossible to know the recycled powder quality, and therefore, exactly how much new material is needed to refresh it. At some point, the old material should be fully discarded in order to avoid dramatic deterioration of the part quality and waste of new material [62].

When you want to recycle material, it is necessary to take into account (i) the percentage of virgin and recycled material to be used and (ii) the number of times the recycled material was used. In order to promote a good balance between the cost of the raw material and the properties of the final part, the EOS's machines recommends a mixture in a range of 30% - 50% virgin PA2200 material with 50%-70% of powder from the part bed [82]. In this research, was used a mixture ratio of 30% of virgin with 70% of processed material in the manufacture of the samples.

2.4.6. Advantages vs Disadvantages

Most importantly, SLS allows users to process a wide range of thermoplastic materials including engineering and high-performance plastics with specific mechanical properties and lowered anisotropy. Because of this advantage, laser sintered parts are durable enough to be used in applications where they are subjected to mechanical loads. Another positive side of SLS, it can fabricate lightweight parts, due to porosity, which may be employed in applications that require large surface areas, for example, scaffolds for cell growth in tissue engineering. SLS presents a wide range of materials that can be reused. This leads to a reduction in emissions due to the need to produce less raw materials [17], [82], [83].

On the other hand, the SLS parts present rough surfaces and poor reusability of non-sintered powder. In the interface between solidifying layers and ready-built portions of the manufactured part, both thermal gradients and densification due to sintering induce residual stresses. The relaxation of these stresses may result in warpage or breakage influenced by powder properties and processing parameters. Its dimensional accuracy is limited by the size of particles of the material and by after melting, attachment of non-melted particles or waviness and roughness of struts. Also, the oxidation needs to be avoided by executing the process in an inert gas atmosphere and for the process to occur at constant temperature, near the melting point [17], [74], [83].

2.4.7. Applications

In general, SLS technology started with the creation of visual prototypes, as a form of validation. However, the advance and development of the technology opened the range to different possible applications.

Nowadays, the parts produced by SLS technology are not mere prototypes, but final parts. That said, it is possible to find SLS technology in different applications, such as medicine, aerospace, heat exchangers, lightweight structures and others, like, micro-tooling [10], [34], [84].

2.5. LATTICE STRUCTURES (LS)

As stated in section 1.1, AM techniques offer great possibilities to develop parts with high complexity and customizability, such as, Cellular Structures (CS) which are ubiquitous in biological systems, structural engineering and materials science (Figure 12). Their concept, including foams, honeycombs, lattices, and similar constructions, comes from keeping material

only in the vital regions of a part to attain a lightweight structure, while maintaining the high specific mechanical properties, such as, strength and energy absorption [85], [86].

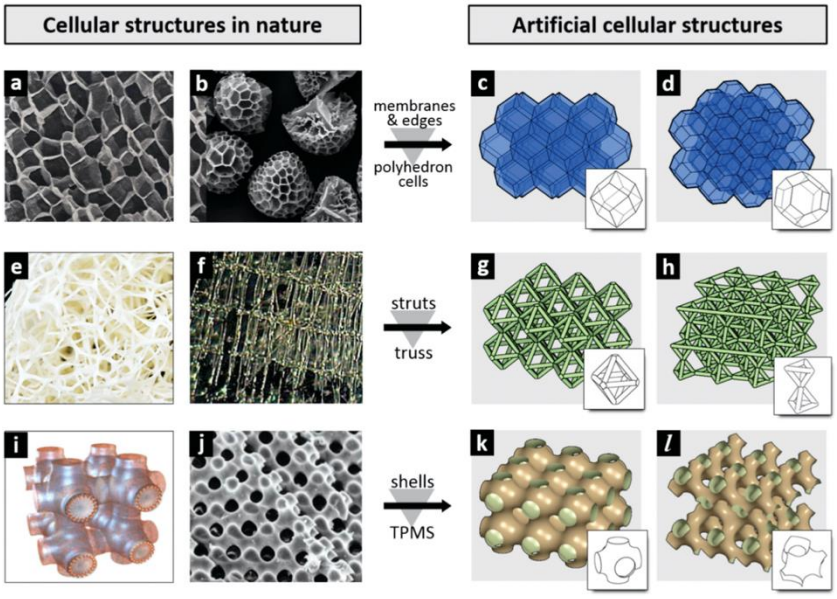

Figure 12 - The figures on the left are photos of cellular structures from nature, while those on the right are configurations of the corresponding artificial cellular structures with their unit cells. a) Cork, b) pollen particles of club moss, c) rhombic dodecahedron cells, d) tetrakaidecahedron cells, e) Luffa, f) glass sponge, g) cells with octahedron trusses, h) cells with Kagome trusses, i) "plumber's nightmare" structure of amphiphilic membranes separating oil and water, j) cross section through a sea urchin skeletal plate, k) cells with P-surface, and l) cells with D-surface [87].

The first traditional methods to manufacture LS appear in the form of weaving, braising and casting [88], [89]. The production of Lattice Structures (LS) is difficult, tedious and time consuming, if not impossible, to produce using conventional manufacturing processes.

Nowadays, LS have become more prominent recently, which are capable to reduce (1) the amount of material utilized in the manufacturing process, (2) the amount of time taken to produce an object, (3) the amount of energy utilized in the manufacturing process and (4) optimize the strength of the produced object while minimizing the weight [90]–[92]. When comprising a single material, LS are easily recycled [90]. They fill a fragment in manufacturing satisfying the requirements of energy absorption, acoustic and vibrational damping, high strength-to-weight ratios and thermal management [94], [95].

With the advance in micro and nanoscales manufacturing, the use of LS has been increasing, which corresponds directly to an increase in the use of AM technologies [93]. LS fabrication is limited to the restrictions of AM processes due to the dependence on AM methods, such as, speed, build space and resolution [92].

The development of new LS solutions requires a review of the existing published research and innovation, as well as, a summary of the latest trends in structure research, which makes possible the identification of potential future research areas [96]. The large amount of potential LS is a great advantage for any given purpose to be utilized in innovative and unique designs, exploiting the innate natures and benefits of the LS [93], [97].

2.5.1. Brief unit cell description

The structure of a crystalline solid is best described by considering its simplest repeating unit, which is referred to as unit cell. It is well known as primitive cell [98]. The unit cell consists of lattice points that represent the locations of atoms or ions under the action of suitable crystal translation operators. The entire structure then consists of this unit cell repeating in three dimensions, as illustrated in Figure 13 [99].

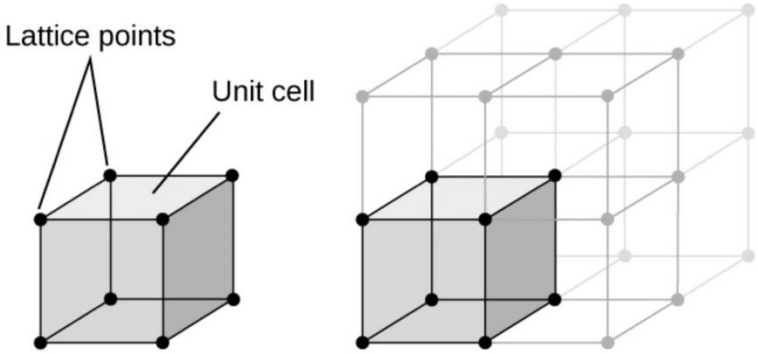

Figure 13 – Representation of a unit cell and it lattice points repeating in all directions.

Analogously, the structure of solids can be described as if they were 3D of a piece of wallpaper, specifying the size, shape, and contents of the simplest repeating unit in the design. Wallpaper has a regular repeating design that extends from one edge to the other. Crystals have a similar repeating design, but in this case, the design extends in three dimensions from one edge of the solid to the other. A description of a 3D crystal can be made by specifying the size, shape, and contents of the simplest repeating unit and the way these repeating units stack to form the crystal.

In short, the unit cell is the simplest repeating unit in the crystal which opposite faces are parallel, and the edge of the unit cell connects equivalent points.

2.5.2. Design of lattice structures

For the fabrication of each part by AM, the LS can be created and stimulated, manually or mathematically, by various CAD software.

To create LS, there are available commercial 3D software tools that aid in the design, such as Autodesk Within Medica (Autodesk, Inc., USA), Materialise Magics (Materialise NV), nTopology Element (nTopology, Inc., USA) and Simpleware CAD (Simpleware, Exeter, UK). But the merging of LS with the objects, the availability of a small selection of unit cell types, the lack of Finite Element Analysis (FEA) integration and the limited optimization capabilities are some of the issues of these softwares. Finally, a STL file format of a particular 3D CAD model is achieved containing only the geometry surface [100]. The other way to produce LS is by using lattice generator which is a free open-source program, that can automatically generate various lattice geometries in STL file format [101].

(i) Unit cell design

The unit cell plays a key role in characterization of the whole LS. It can be drawn from two different methods: primitive based method and implicit surface-based method. The primitive based method relies on Boolean operations of simple geometric primitives, in which, the unit cell consists of some geometric primitives. Figure 14 shows the example of two primitive based topologies (Figure 14 -- a and b) and some strut-based LS (Figure 14 – c).

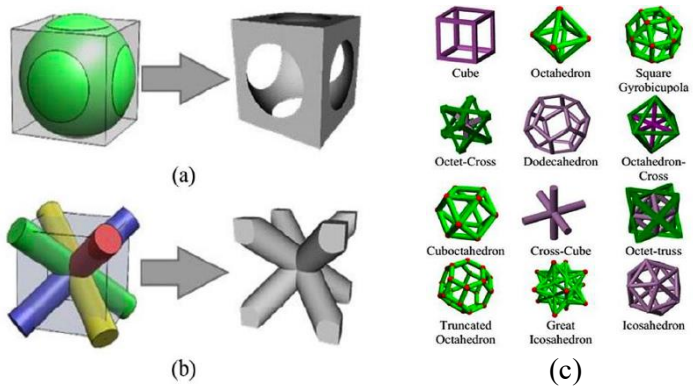

Figure 14 - Schematics of the primitive based method: (a) Boolean subtraction of the cube and a sphere, (b) Body Centered Cubic (BCC) strut-based LS and (c) others strut-based LS [102], [103]

The implicit surface-based method uses mathematical equations to represent the surface of a unit cell in 3D space. These equations form the well-known TPMS which overall mechanical properties are significantly influenced by the porosity of the unit cell (Figure 15). In contrast to the primitive based method, this porosity can be parametrically controlled by specifying different terms in the equations [104].

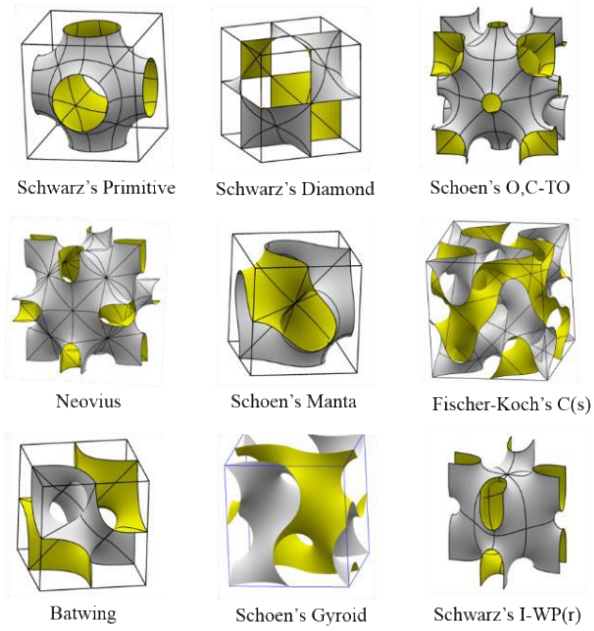

Figure 15 - TPMS unit cell topologies [105].

(ii) Pattern strategies

According to the configurations of the LS, each configuration has its own characteristics, being therefore more prone to a certain application. LS result from the patterning of unit cells in a 3D space. Pattern design can create LS from an array of unit cells using different methods, such as:

- Direct patterning, also called uniform patterning or periodic LS, copies the unit cell along the x-, y- and z-axis creating parallelepiped shaped three-dimensional arrays., in which the unit cells are translationally repeated Figure 16 [106]–[108].

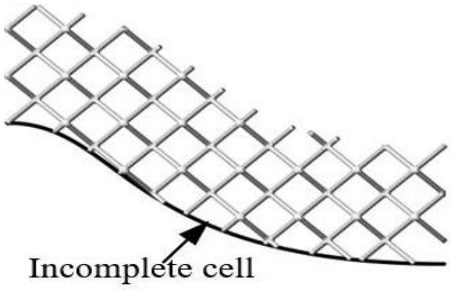

Figure 16 – Direct patterning of LS [109].

- Conformal patterning, in which the units are repeated conforming to a given surface geometry, that is able to guide the population of unit cells to conform to the shape of a design space (Figure 17). The integrity of the unit cell is retained, which can distribute the load throughout the whole structure [110].

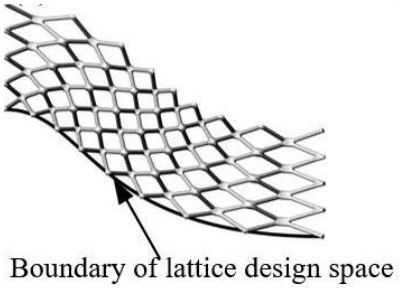

Figure 17 – Conformal patterning of LS [109].

- TO, which can be used to not only optimize the material distribution in a single unit cell, but also to organize the spatial replication of the unit cell through the whole design space. It can be used either in cell design or pattern design [110]. As no exception, TO can design FGM too (Figure 18).

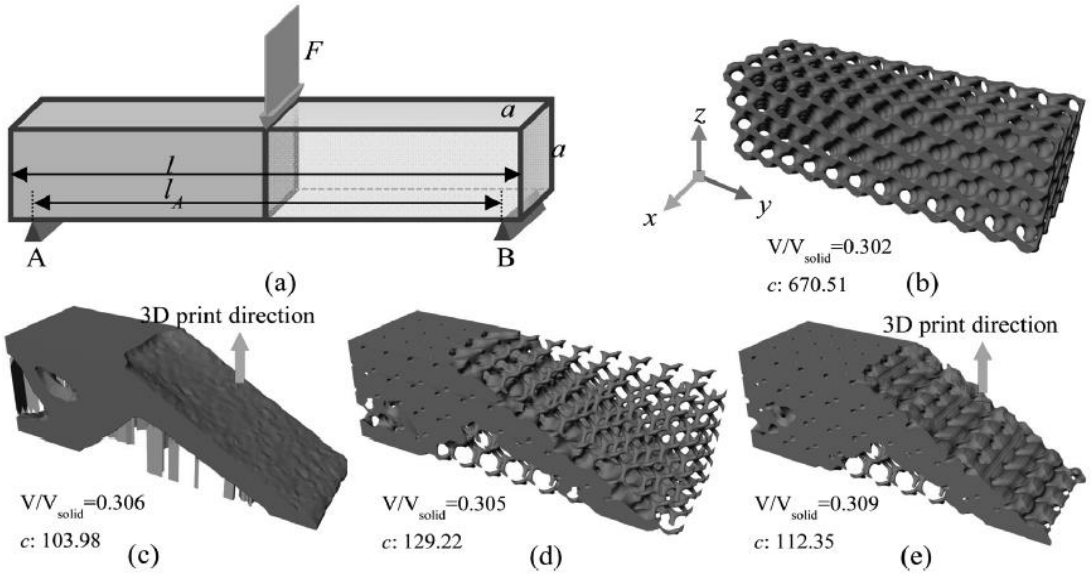

Figure 18 - Different optimization strategies of TO with (a) load and boundary condition of beam; (b) traditional lattice design method with uniform gyroid; (c) standard TO approach; (d) our shape-retained FGM optimization method; (e) our direction-constrained FGM optimization method [91].

Inside of each method described above, the patterning of LS unit cells can form a homogeneous (Figure 19 - a) or heterogeneous (Figure 19 – b) lattices. From the heterogeneous lattices arise the best-known Functionally Graded Materials (FGM) which can gradually change the porosity of the unit cell in overall dimensions. Their mechanical properties vary smoothly and continuously from one surface to the other [110], [111].

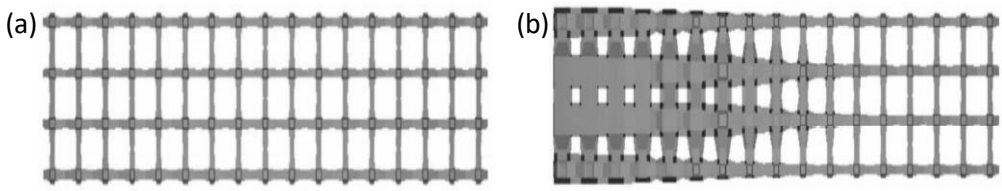

Figure 19 -Difference between (a) homogeneous lattice and (b) heterogeneous lattice.

2.5.3. Topologies of lattice structures

To be considered a LS, the unit cell must be fully characterized in terms of structure design, the method of generation and the inherent properties.

Actually, there is a small amount of LS (<40), of which a significant amount is extracted from structures found in traditional geometries. To create a new one, it should possess unique

capabilities that make them superior in comparison to others, such as, increased strength or energy absorption to weight ratios [96], [112], [113].

Due to their simplicity in nature, manually generated LS can be broken down to very basic geometric shapes. Some examples of them are: Octet truss [114], 3D Kagome structure, Tetrahedral structure [113], Body centered cubic [110], [111]. On the other hand, some examples of mathematically generated LS, better known as TPMS LS include: Primitive, Neovius, Diamond, Gyroid and I- WP surfaces [117]–[119].

From the existing topologies, BCC, Schwarz-P and Neovius were selected for this study. Thus, the following subsections report, briefly and individually, certain fundamental facts.

(i) Body-Centered Cubic, BCC

As a strut-based unit cell, the BCC lattice can be obtained by adding a second lattice point, at the center of each cubic cell, of a simple cubic lattice [120]. Thus, the unit cell of each BCC lattice can be considered as two interpenetrating simple cubic primitive lattices. In fact, there are two alternate ways of considering it as a lattice, either with a simple cubic lattice formed from the corner points with a lattice point at the cube center, or with the simple cubic lattice formed from the lattice points at the center and the corner points located at the center of the new cubic lattice. In either case, each one of the eight lattice points at the corner of a cubic cell is shared by eight adjacent cubic cells, while the lattice point at the center of the cubic cell exclusively belongs to that cell [98]. As showed in Figure 20, it can be described by four geometrical parameters: the lattice strut diameter, the angle between strut elements, the elementary unit cell height (L) and the cross-sectional shape. The angles of struts, to each other, within the unit cells are a function of varying unit cell side lengths, and so, do not need to be tested on their own [121].

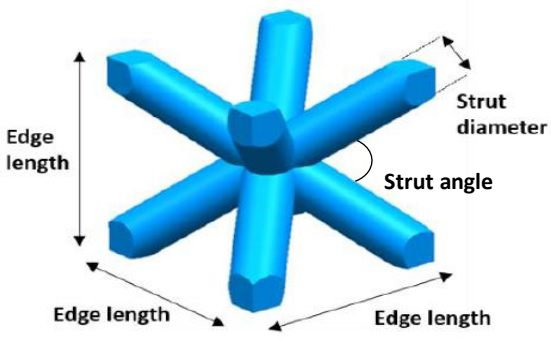

Figure 20 – BCC geometrical parameters.

(ii) Schwarz – P

As a TPMS unit cell, the creation of the Schwarz-P unit cell uses mathematical surface renderings. It is the simplest and the most well-known of the TPMS containing six openings centered on the faces of a cube (Figure 21). With a desired symmetry, topology, and volume fraction, Schwarz P structures were formed using the Equation 1 [122]–[124]:

$$F(x, y, z) = \cos x + \cos y + \cos z \tag{1}$$

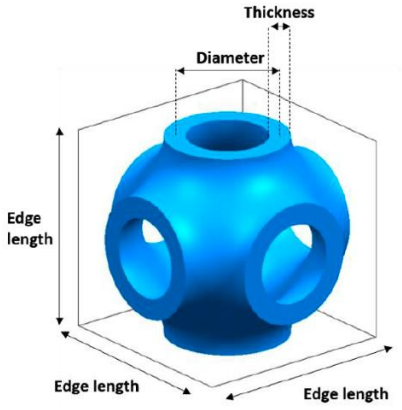

Figure 21 - Schwarz-P surface.

(iii) Neovius

Edvard Rudolf Neovius was a student of Hermann Amandus Schwarz. His surface, published in 1883, is by far the most complicated minimal surface discovered in the 19th century [125]. The Neovius surface is a triply periodic minimal surface the fundamental patch of which, reproduced opposite, has 12 openings centered on the edges of the cube, hence at the vertices of a cuboctahedron. Its surface, showed in Figure 22, can be made thanks to the Equation 2. The complete Neovius surface splits the space into to connected components, isometric to one another, like the Schwarz P surface [126].

$$3 \cdot (\cos x + \cos y + \cos z) + 4 \cdot \cos x \cdot \cos y \cdot \cos z = 0 \tag{2}$$

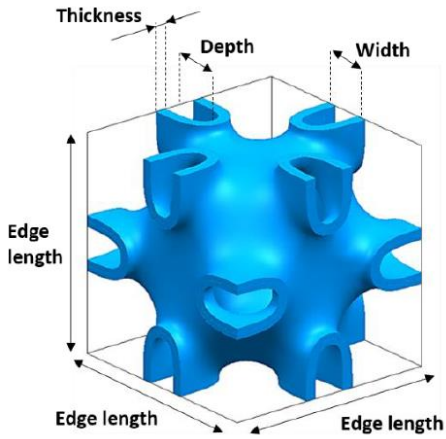

Figure 22 – Neovius surface.

2.5.4. Mechanical characterization of lattice structures

The mechanical properties of a LS, such as, Young's modulus, yield strength, brittleness, ductility, etc., are dependent on the material, architecture that organizes the material distribution, porosity, that is inversely proportional to the relative density of the material and, on the processing conditions [110]. Based on their mechanical response, by implementing different types of loadings, LS can be classified into stretching dominated and bending dominated, where LS are defined by its own cell topology [90], [100].

Figure 23 shows a typical nominal stress-strain behavior of a cellular material under compressive loading. It can be simplified into three definite regions: elastic, plastic and densification. At small strains, usually less than 5%, the cell edges bend giving a linear elastic deformation, with a slope equal to the Young's modulus of the sample. At a certain stress level, the cell walls begin to collapse by elastic buckling, plastic yielding or brittle crushing, depending on the mechanical properties of the cell walls. As the load increases, in plastic region, a subsequent collapsing progress at roughly constant load, giving a plateau strength, $\sigma_{pl.}$, until the opposing walls in the cells meet and touch, at a densification strain, ε_D. From here, the densification causes the stress to increase steeply [127], [128]. A typical stretch-dominated stress-strain curve has a large slope in the elastic deformation region, achieves a high yield strength before a softening post yielding response. Then there is a basin region due to the continuous collapse of the struts, after which, the stress increases dramatically because the internal pores vanish, and the struts merge together. Its mechanical behavior is suitable for lightweight structure design, where high specific stiffness and strength are desired. The bending-dominated architecture has a shorter linear region, with a relatively lower yield strength, but a broad plateau region before the densification phenomena. Its design priority is for energy absorption

applications due to the ability to endure large deformation at a relatively lower stress level [129], [130].

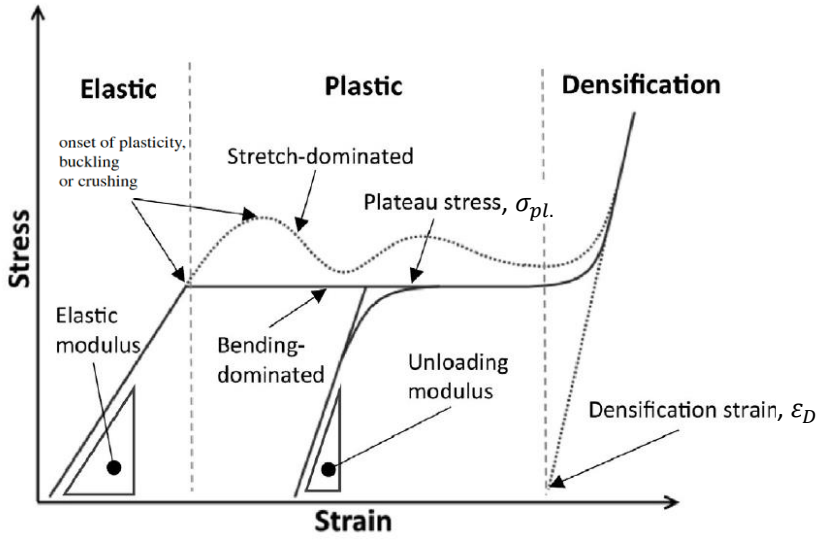

Figure 23 - General compressive behavior of stretch and bending-dominated lattice structures during their distinct regions [90].

With regard to instrumented falling weight impact tests, the respective force-deflection curves, which contains the details of a complete impact, including the type of deformation, fracture initiation and propagation, can take many different shapes. As an idealized behavior, Figure 24 - a shows a typical force-deflection curve for a tough polymer, which exhibits yielding with cup formation (zero slope at maximum force), followed by diametrical splitting of the cup (sudden drop in force) and stable tearing. Figure 24 - b represents another example of a test on a fiber reinforced material that can show many more features. A 'first damage' peak (at F_D, S_D) occurs before the maximum force is reached. Such peaks are often associated with localized splitting, resulting in the load drop and change in specimen compliance. The local damage then stops growing, requiring increased force and energy for the damage to progress further at maximum force, F_M. It also shows that considerable energy is required to progress the damage beyond the puncture deflection, S_P, to produce total penetration of the specimen by the striker. The concept of puncture deflection is a deflection at which the force has dropped to half the maximum force [131]. Adding the impact characterization of LS specimens, these curves can take other forms [132].

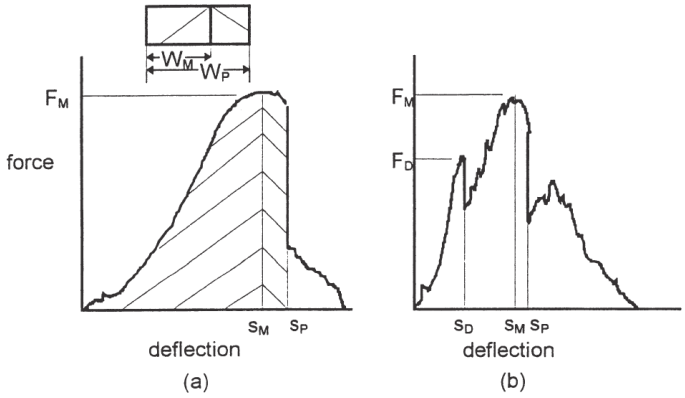

Figure 24 - Force-Deflection curves: (a) Typical curve for tough polymer, (b) Curve for a fiber reinforced material [131].

(i) Maxwell's criterion

Strut-based topologies can be characterized by their Maxwell number, M, from the Equation 3, which is dependent on the number of struts, s, and nodes, n.

$$M = s - 3n + 6 \tag{3}$$

If M < 0, there are too few struts to equilibrate external forces without equilibrating moments induced at the nodes, causing bending stresses to develop in struts and leading to bending-dominated behavior. If M ≥ 0, external loads are equilibrated by axial tension and compression in struts meaning that no bending occurs at nodes, making these structures stretch-dominated [130].

Due to these phenomena, the stretch-dominated architectures are more stiff and strong (higher modulus and yield strength) compared to the bending-dominated architecture with the same relative density [129].

(ii) The Gibson–Ashby model

The most significant theoretical work regarding the deformation and mechanical properties of cellular solids is that of semi-empirical formulae of Gibson and Ashby, treating foams as arrays of connected beams and provided a series of equations relating their mechanical properties to their relative density, such as Young's modulus, plateau strength, and densification strain. For cellular solids, made from materials that have a plastic yield point, Gibson and Ashby

introduced the Equations 4 a - c, where the relevant physical properties are given in Table 2 [133], [134]:

$$\frac{E_{latt.}}{E_{sol.}} = C_1 \cdot \left(\frac{\rho_{latt.}}{\rho_{sol.}}\right)^n \tag{4a}$$

$$\frac{\sigma_{pl.\ latt.}}{\sigma_{y\ sol.}} = C_5 \cdot \left(\frac{\rho_{latt.}}{\rho_{sol.}}\right)^m \tag{4b}$$

$$\varepsilon_D = 1 - \alpha \left(\frac{\rho_{latt.}}{\rho_{sol.}}\right) \tag{4c}$$

From the equations described above, the prefactors C1, C5 and α play a significant role in determining the mechanical properties and deformation behavior of LS. For the prefactors C1 and C5, which include all of the geometric constants of proportionality, Gibson, Ashby et al. provide a range of values from 0.1 -- 4.0 and 0.1 -- 1.0, respectively, while n and m are about 2 and 1,5, respectively, when deformation occurs by bending of the cellular struts or walls. For the value of α, it varies between 1.4 -- 2.0. [133].

Table 2 - Physical and mechanical properties for the description of lattices under compression [134].

Notation	Physical or mechanical property
$\boldsymbol{\rho_{latt.}}$	Density of the lattice structure
$\boldsymbol{\rho_{sol.}}$	Density of the material constituting the lattice struts or walls
$\boldsymbol{\rho^*}$	Relative density, or volume fraction, of the lattice; equal to $\rho_{latt.}/\rho_{sol.}$
$\boldsymbol{\varepsilon_D}$	Densification strain of the lattice
$\boldsymbol{E_{latt.}}$	Elastic modulus of the lattice structure
$\boldsymbol{E_{sol.}}$	Elastic modulus of the material constituting the lattice struts or walls
$\boldsymbol{E^*}$	Relative elastic modulus of the lattice; equal to $E_{latt.}/E_{sol.}$
$\boldsymbol{\sigma_{latt.}}$	Effective stress of the lattice structure
$\boldsymbol{\sigma_{pl.latt.}}$	Plastic collapse strength, or plateau strength, of the lattice
$\boldsymbol{\sigma_{y\ sol.}}$	Yield strength of the material constituting the lattice struts or walls
$\boldsymbol{\sigma^*}$	Relative collapse strength of the lattice; equal to $\sigma_{pl.latt.}/\sigma_{y\ sol.}$

To use the equations above for effective LS design, either by manually selecting an appropriate volume fraction or through implementation of a combined lattice TO approach, one

must know the Gibson-Ashby prefactors and exponents for the chosen lattice cell type. They may be determined from experimental compressive tests, by manufacturing and testing lattice specimens of varying their relative densities, and then, applying appropriate fitting to the mechanical data [135]–[137], by finite element calculations and by the construction of analytical models based on structural failure mechanisms [138], [139].

(iii) Finite Element Analysis, FEA

FEA is an alternative approach delivering insight in the mechanical characteristics. The loading conditions are simulated in CAE software and the computer numerically calculates an estimation of the effective mechanical response using the Finite Element Method (FEM). This strategy completely relies on computational procedures and does not require the fabrication of physical parts. This makes the measurement of the mechanical properties a faster and low-cost than experimental tests. Engineers often adopt FEA in conceptual stages to avoid fabricating numerous prototypes. Inherently, the method is only an estimation and produces errors, constituting a drawback. Powerful computers and advanced CAE systems are required to minimize errors and obtain accurate solutions [92], [140].

For this report, mechanical compression and impact tests to know the properties of each structure were considered to facilitate the prediction of the theoretical behavior. According to the technical datasheet of the material in question, the simulations were performed. If, in a first attempt, the simulation corresponds to the experimental tests, it is excellent. Otherwise, it is necessary to understand the mechanical tests of the structure in question and make certain adjustments until reliable simulations are obtained. Once this similarity, between the real and the virtual, for a given parameter has been achieved, it is varied twice more in order to improve and extend the software capabilities, for future applications of these structures on parts with pre-established requirements. This way, it is possible to optimize the topology of LS. The smaller the difference between the simulations and the experimental tests, the more time is gained when you want to reach the final product, and the less money is spent on prototype production.

2.5.5. Advantages vs Disadvantages

LS are an attractive option for many design applications, particularly lightweight applications, due to the high specific strength and stiffness provided by their porous structure. The deformation behavior of cellular structures also means they are useful for energy absorption applications [90]. On the other hand, complex LS with overhang areas needs support structures to ensure an accurate building process [141].

2.5.6. Applications

A wide variety of industries exploit the benefits of LS. This type of structures is widely employed in the medical industry, where they ca be useful by replacing tissues and bones. LS drastically decreased invasiveness and recovery time [86], [108]. Another application for LS is in the automotive industry, due to the weight reduction and increased ease of recycling of automotive parts [142]. In aerospace, LS aim to increase the performance-to-weight ratio, in order to build efficient vehicles with strong and lightweight parts [143]. LS can also be employed in protective applications due to the energy-absorption properties. Energy-adsorption is based in the ability of distributing an impact shock across the object [144]. In addition to presents applications fields, LS can also be applied in architecture industry.

3.METHODOLOGY

Maintaining the process conditions of SLS technology, the objective of this research is to investigate the effect of changing both the architecture and as-built morphological properties of 3 different topologies types of LS on their mechanical behavior. This section presents the description of the experimental part of this report, involving the mechanical response of 3D regular cellular structures, with different topologies, subjected to uniaxial compressive and impact tests.

3.1. DESIGN OF LATTICE-BASED SPECIMENS

In the current study, strut based and TPMS cells are used to create architecture cellular materials. The CAD software used for the 3D modeling of the samples was Siemens NX CAD.

Therefore, one-unit cell of the type of manually generated structures (strut-based) and two of the type of mathematically generated structures (TPMS) were chosen. Within the first type, the Body Centered Cubic cell (**BCC**) was chosen as the driving cell for this new way of producing functional and lightweight parts and its simplicity of design (Figure 25 - a). Within the second, the Gyroid unit cell was initially chosen due to its interesting mechanical performance, when applied to end use parts. This unit cell was eventually changed due to its complex and ingenious three-dimensional modeling in the CAD software during linear patterning in order to obtain the overall sample shape. That is, the unions of the surfaces were not smooth according to the equation which constitutes the unit cell. Instead of this, Schwarz-P (**P**) and Neovius (**N**) unit cells were selected, classified as open cells (Figure 25 – b, c). The choice of three cellular units has allowed broader results to be obtained as a means of comparing the mechanical performance of each structure.

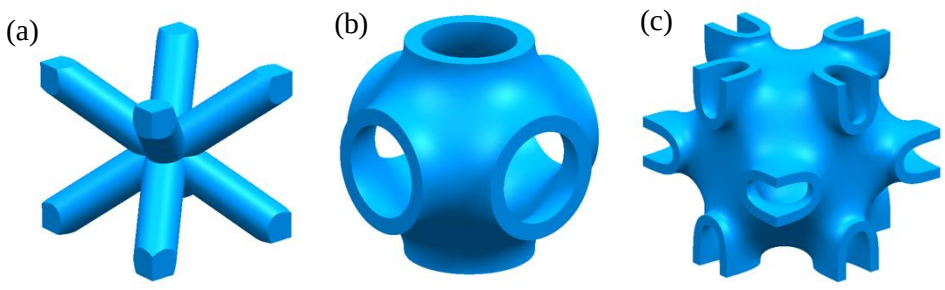

Figure 25 –(a) BCC, (b) Schwarz-P and (c) Neovius unit cells modelled by Siemens NX CAD.

3.1.1. Overall dimensions

It is known in advance that, depending on the type of mechanical test to be performed, a certain shape and dimensions of the test sample are required. As previously mentioned, for this study, mechanical compression and impact tests were performed. That said, the forms adopted for the compression and impact tests were quadrangular (parallelepiped) and circular (cylinder) primers, respectively.

According to a study carried out, by several researchers, and related to the mechanical properties of LS, a minimum number of 2 cellular units present in each x, y and z axis is sufficient to obtain reliable results in the compression tests [145]. Thus, the adopted overall dimensions were 40 x 40 x 80 mm according to the test norm ASTM D 695 - *02*. For the impact tests, the overall dimensions used in the production of the flat discs were 60 mm in diameter and 20 mm in height. The diameter of the test samples was pre-established according to ISO 6603-1-2000, while the height value was defined considering the available height space of the testing machine (Figure 26).

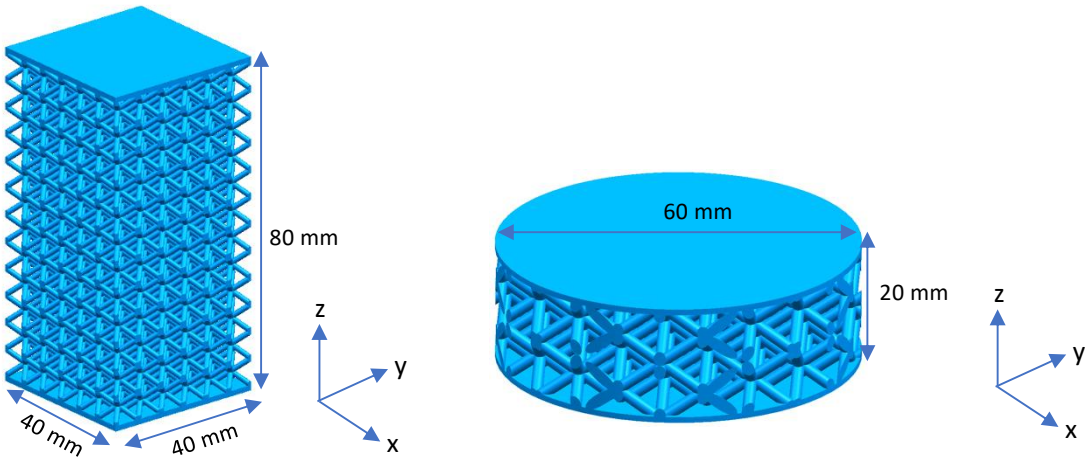

Figure 26 -Overall dimensions of compressive test samples (left image) and impact test samples (right image).

In an intuitive way, the dimensional accuracy of SLS specimens is expressed by error S_1. For each sample, three measurements were made for each axial x, y and z axis. Thus, the dimensional accuracy of the SLS in each axis can be defined from the Equation 5,

$$S_1 = \left[\frac{A_1 - A_0}{A_0}\right] \times 100\% \quad (5)$$

where A_0 is the design size given by the computer and A_1 is the real size measured by a vernier caliper. If the S_1 error value is positive, it means that the polymeric powder expands and if it is negative, the powder contracts [146].

3.1.2. Variable parameters of unit cells

As described in section 2.4.1, LS are composed of several unit cells, with specific parameters that determine the mechanical performance of the part. From the possible parameters include cell size, shell and surface/strut thicknesses for compression tests, and shell and surface/strut thicknesses for impact tests were selected in this study (Figure 27). It should be noted that the strut diameter of the strut-based unit cell and the surface thickness of the TPMS unit cells are both the same parameter. In order to simplify the presentation and understanding of the results, the term surface thickness was used for both cases.

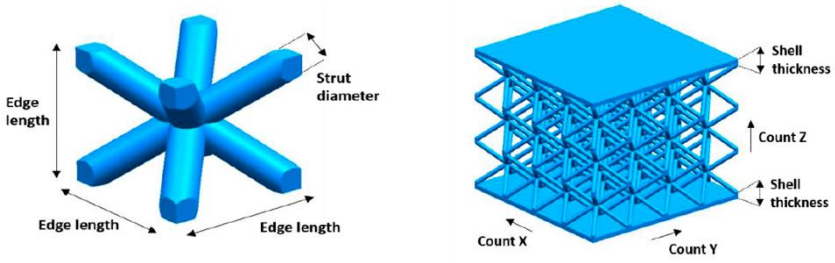

Figure 27 – Variable paramters of the research.

The original structures topologies modelled by Siemens NX CAD have different mass-inertia properties. In order to understand the behavior of each parameter on the produced samples, Equation 6 represents the way to determine the value of a relative density of different cell topologies based on measured structure dimensions and defined densities:

$$\rho_r = \frac{\rho_v}{\rho_m} \quad ; \quad \rho_v = \frac{m}{V} \tag{6}$$

where ρ_r – relative density of the cellular structure, ρ_v – density of the structure, ρ_m – material density, m – produced model mass, V – produced model volume.

Due to the large number of samples to be studied, the list below represents the nomenclature assigned, where the numbers 1 and 2 represent the variation of the parameter in question:

BCC (B)	**Schwarz – P (P)**	**Neovius (N)**
BR - B Reference	**PR** - Reference	**NR** - Reference
BT1 - B Surface Thickness 1	**PT1** - Surface Thickness 1	**NT1** - Surface Thickness 1
BT2 - B Surface Thickness 2	**PT2** - Surface Thickness 2	**NT2** - Surface Thickness 2
BC1 - Cell size 1	**PC1** - Cell size 1	**NC1**- Cell size 1
BC2 - Cell size 2	**PC2** - Cell size 2	**NC2** - Cell size 2
BS1 - Shell thickness 1	**PS1** - Shell thickness 1	**NS1** - Shell thickness 1
BS2 - Shell thickness 2	**PS2** - Shell thickness 2	**NS2** - Shell thickness 2

To make possible the understanding of the mechanical behavior of cellular structures by varying each parameter of the respective unit cell topology, the relative density must be maintained. So that, Appendix 1 shows the relative densities of the overall LS used in this research ($17\% > \rho^* > 23\%$ for compressive tests and $21\% > \rho^* > 39\%$ for impact tests). Here, it is necessary to add a fundamental point regarding the unit cell size parameter. In order to maintain the relative density, when the cell size is varied, the walls thickness of the cells must be varied, which in no way interferes with the objective in study. From here, the base values showed in each parameter tables dictate the reference sample, **R**.

(i) Surface/diameter thickness, T

In the three different unit cells the surface thickness has been varied 3 times. That said, according to the Table 3 it is possible to observe, in more detail, how this parameter varies.

Table 3 -Variation of surface thickness parameter (T).

	Surface thickness [mm]
BT1	1,70
BR	2,00
BT2	2,30
PT1	0,57
PR	0,76
PT2	0,98
NT1	0,38

NR	0,51
NT2	0,65

(ii) Cell size, C

In order to understand the influence of the unit cell size, three sizes of each unit cell topology were chosen that best fit the defined overall dimensions of the structure. Table 4 shows that variation. The study of this parameter was only made in the compression tests. That is, since two is the minimum number of unit cells present in each of the three-dimensional Cartesian axes to obtain consistent results [145], the cell size did not enter in the impact tests due to the fact that the maximum sample height specified by the test machine used is 20 mm. However, since the size of the reference cell is at least 10 mm high, only two cells on the z-axis can be manufactured.

Table 4 - Variation of unit cell size parameter (C).

	BCC	Schwarz-P	Neovius
Cell size [mm]	10 x 10 x 10		
	13,33 x 13,33 x 13,33		
	20 x 20 x 20		

(iii) Shell thickness, S

With regard to shell thickness, the overall dimensional integrity of the samples was maintained, that is, the total height of 80 mm was maintained. As showed in Table 5, the shell thickness was changed between 0, 1, 2 for compression tests and 1, 2 and 3 for impact tests.

Table 5 - Variation of the shell thickness parameter (S).

	BCC	Schwarz-P	Neovius
	Compression tests		Impact tests
Shell thickness [mm]	0		1
	1		2
	2		3

3.2. EXPERIMENTAL TESTS

Typically, any scientific study concerning material characterization requires testing at least three test samples of the same design configuration and dimensions. The same was done in the present experimental work in order to obtain reliable results, averages and standard deviations. Considering all the parameters mentioned in the previous section, the number of times each one

of them varies and their respective clones, a total of 108 tests were performed: 63 compression tests and 45 impact tests. Each sample has been duly identified with the nomenclature referred to in section 3.1.2 in order to facilitate its recognition after extraction of the parts after production and subsequently in the respective mechanical tests.

3.2.1. Material and technology

PA12 powders are the most used materials in the SLS process. The PA12 molecule structure, constituted by carbon atoms and amide group, provide strong bonds, mainly the hydrogen bonding, that determine mechanical and thermal properties of the molecule [147], [148]. It is a semi-crystalline polymer and has a highly heterogeneous microstructure due to containing both amorphous and crystalline phases. The mechanical properties of semi-crystalline polymers are a function of the amount and morphology of the crystalline regions. The crystalline region is responsible for the strength, whereas the amorphous region provides ductility by allowing the polymer to yield without breaking [149].

According to some studies, the mechanical properties of PA 2200 manufactured samples well match with the datasheet data. In [150], the tensile elastic modulus of PA 2200 was obtained as 1,35 ± 0.04 GPa and the yield strength as 23,3 ± 0.5 MPa; while compressive elastic modulus and yield strength as 1,14 ± 0.03 GPa and 48,1 ± 0.9 MPa, respectively. In [134], the tensile elastic modulus obtained was 1,80 ± 0,05 GPa and the yield strength was 29,1 ± 0,8 MPa; the results for the compressive behavior using cubes of size 20 mm^3 were compressive elastic modulus as 1,59 ± 0,02 GPa and respective yield strength as 44,5 ± 0,3 MPa.

Appropriately modified for its implementation in the AM, the raw material that constituted the research samples was PA 2200 composed by 70% of recycled material and 30% of virgin material. In the Table 6 it is possible to check its traction properties at a speed of 10 mm/min with a 50 kN load cell, at room temperature. Further details about the PA 2200 can be found in the technical sheet provided by the supplier (Appendix 2).

Table 6 - Mechanical properties of PA 2200 in tension tests (70% recycled with 30% virgin material) [151].

Property [Unit]	**E [MPa]**	**σ_{Yield} [MPa]**	**σ_{Break} (MPa)**	**ε_{Yield} [%]**	**ε_{Break} [%]**
Part at 0º (70% - 30%)	1531,65 ± 20,77	44,68 ± 0,71	43,12 ± 0,65	11,17 ± 0,11	17,53 ± 0,85

Note: **E –** Young's Modulus **σ_{Yield}** – Yield stress **σ_{Break}** – Break stress **ε_{Yield}** – Yield strain **ε_{Break}** - -Break strain

The laser sintered test samples modelled by Siemens NX CAD software were built on EOS P396 machine with a build orientation of 0º. Although the most relevant processing parameters used in the current study are shown in Table 7, its Technical Data is showed Appendix 3. As already mentioned here, they were maintained throughout production.

Table 7 - SLS parameters used in the production of the lattice structures for mechanical testing.

SLS parameter	
Laser power (Hatching)	40 W
Laser power (contour)	34 W
Beam offset	0,320 mm
Layer thickness	0,12 mm
Process chamber temperature	173 ºC
Removal chamber temperature	130 ºC

3.2.2. Characterization of lattice structures

In order to successfully develop a product, it is necessary to know the behavior of the material that constitutes it and its performance. Hence, its characterization is a crucial step in the project. In order to characterize the present sample structures, the mechanical compression and impact tests were done.

The compression test procedure was once again governed by standard ASTM D695. The compression machine used was the INSTRON 5969 Dual Column Tabletop Testing System (without extensometer) with a maximum load capacity of 50 kN. This process was monitored and recorded using the Bleuhill software. According to the standard, the samples were compressed with traverse velocity 1,3 mm/min in a perpendicular direction to their direction of construction in order to achieve the modulus of elasticity, E, the compressive yield strength, σ_Y, and respective yield strain ε_Y with an offset of 0,2%, the densification strain, ε_D, the plateau stress, $\sigma_{pl.}$, and the energy absorption, W_D (which is the area under the stress – strain curve). The capability of absorption energy of each LS was calculated until the possibility to damage the objects or injury the human body, that is, until the densification strain [150]. To determine this optimal energy absorption of LS, it was considered the energy efficiency method, which is defined by [152]:

$$\eta(\varepsilon) = \frac{1}{\sigma(\varepsilon)} \int_0^{\varepsilon} \sigma(\varepsilon) d\varepsilon \quad (7)$$

$$W_D = \int_0^{\varepsilon_D} \sigma(\varepsilon) d\varepsilon \quad (8)$$

To correctly perform the tests and achieve maximum valuable and reliable information, it is necessary to mention two aspects that have been previously established. The first one is the use of Teflon sheets on both surfaces of compressor plates (Figure 28-a). This was considered to reduce the friction, between the surfaces of the plates and the sample, in order to consider it as a free body. Also, it would allow to determine more clearly the compression force exerted by the plates, disregarding the remaining forces, they also facilitate future simulations. The second one is the marking of strategic points on the front face in order to understand possible reading errors by the machine (Figure 28 - b). To this end, photographs were taken, every 30s, using a digital camera NIKON COOLPIX B700. The process was stopped after a clear check of the densification of the samples, at 75% of deformation.

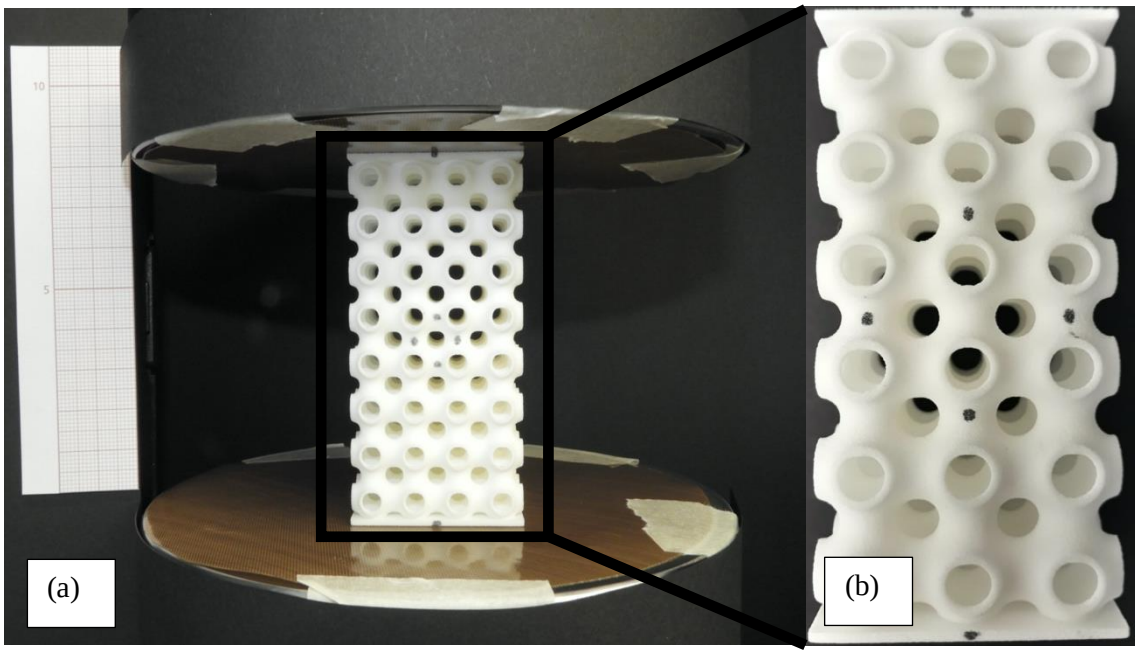

Figure 28 – (a) Pre-set of compressive tests and (b) strategic points on the front face.

In regarding to the impact tests, typically, they are performed when the behavior of a given product is to be studied for a specific application, that is, when the variation of the parameters to be studied is already known in advance. An example of this variation is the

characterization of the amount of energy and/or deformation to which the product will have to resist.

With no precedent, this study was carried out with the FRACTOVIS PLUS impact machine capable of launching the strike at a maximum height of 1m with a weight variation between 5 kg and 70 kg (Figure 29 - a, b), and with a sampling frequency of 250 kHz. The clamping system adopted with an external diameter of 100 mm and an internal diameter of 40 mm is showed in Figure 29 - c. All the specimens were tested with a pneumatic clamping force of 2 N. The strike used has a 20 mm diameter hemispherical head and presents an impact velocity of 4,429 m/s. Based on ISO 6603-1-2000, the stipulated height of the strike drop was 1 m. Initially, one sample of each variable parameter of the **B** topology was used in an attempt to find out whether the strike was capable of penetrating them completely. Here, the impactor mass used was 5,044 kg. When preliminary tests were carried out to define the test parameters, it was found that, without addition of load, the speed variation was over 20%, which is not recommended by the standard. To decrease the speed variation there were two possibilities, either to increase the height or to add an increment mass on the strike. But as the maximum height governed by the standard as well as the maximum height permitted by the equipment was already in use, all that remained was to increase the mass, hence the addition of an increase of 5 kg. However, the impactor mass used in the impact experiments was 10,044 Kg. This effect allows a linear drilling of the impactor. Once the test parameters were known, the impact tests were carried out at room temperature to predict the maximum force, F_M, the deflection at maximum force, S_M, the energy at maximum force, E_M, the puncture deflection, S_P, and the puncture energy, E_P (Figure 24).

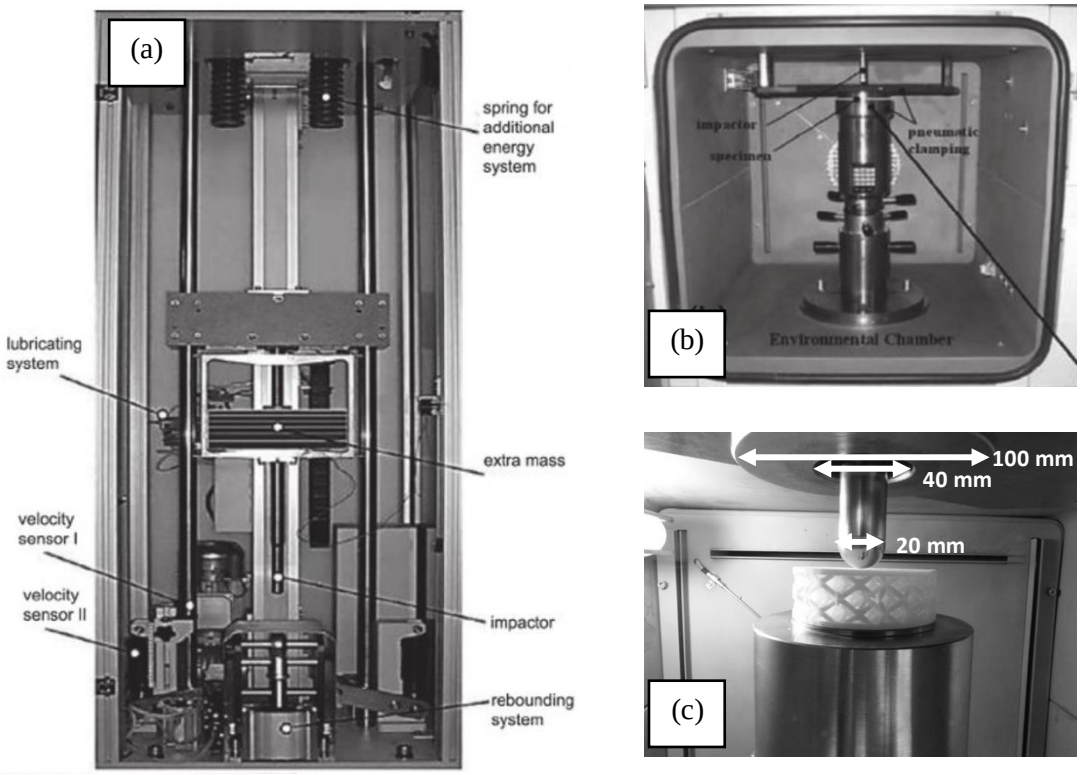

Figure 29 - FRACTOVIS PLUS impact machine: a) impactor (top of the machine); b) sample chamber (bottom of the machine); and c) sample placement.

4. RESULTS AND DISCUSSION

Chapter 4 presents the results and discussion in regarding to the mechanical behavior of the LS. The effect of overall dimensions on the mechanical response of the LS is investigated to ensure that the results represent the effective response. The chapter is divided in compressive and impact tests and the results are described in regarding to the characterization tests discussed above. Chapter 4 starts to present the dimensional accuracy, followed by the relative density. Then, the reference samples are examined. At the end, are presented the effect of cellular parameters on the mechanical response of the **B**, **P** and **N** cellular structures at respective relative densities.

4.1. COMPRESSION TESTS

Several researches in the scope of understanding the influence of the independent variables of the unit cell, were carried out from compression tests [90], [145], [150].

Throughout this section, the graphs presented report the behavior of cellular structures when subjected to uniaxial compression, but first, it needs to address the dimensional accuracy and the relative density of the produced samples in order to make reliable comparisons.

First of all, dimensional accuracy has been measured and the results are shown in Table 8. The results indicate that the samples shrink in x and y-axis and expands in the z axis. From a general point of view, all the cellular structures shrink when comparing their respective volumes with a maximum error of 0,08% ± 0,33% for **N** samples. These divergences were mainly caused by the additive characteristics of the manufacturing process and the size of the adopted PA2200 powder grains.

Table 8 - Dimensional accuracy of compressive test samples.

	S1 (%)		
	BCC	**Schwarz – P**	**Neovius**
X	-0,21 ± 0,05	-0,34 ± 0,10	-0,37 ± 0,04
Y	-0,21 ± 0,13	-0,29 ± 0,07	-0,30 ± 0,10
Z	0,14 ± 0,06	0,49 ± 0,07	0.01 ± 0,06
Volume	-0,01 ± 0,18	-0,01 ± 0,21	-0,08 ± 0,33

After that, the experimental relative densities of cellular samples are shown in Table 9. Comparing this data with estimated values on the basis of the CAD model, some disagreements between relative density values were noticed. These discrepancies could be explained by the particular features of the technological manufacturing process used, by the density of base

material provided by the supplier datasheet, by the accuracy of the layer connection, or by the inability to remove the entrapped powder from inside the sample.

Table 9 - Experimental and modelled relative densities of compressive test samples.

	Relative density [%]				
	Experimental	CAD model		Experimental	CAD model
BR	20 ± 0,08	19			
PR	20 ± 0,13	19			
NR	23 ± 0,40	18			
BT1	15 ± 0,18	14	**BT2**	24 ± 0,07	23
PT1	17 ± 0,12	14	**PT2**	26 ± 0,02	23
NT1	23 ± 0,60	14	**NT2**	29 ± 0,38	23
BC1	19 ± 0,13	19	**BC2**	19 ± 0,07	19
PC1	19 ± 0,15	19	**PC2**	20 ± 0,10	19
NC1	20 ± 0,31	19	**NC2**	20 ± 0,14	19
BS1	17 ± 0,08	17	**BS2**	21 ± 0,02	20
PS1	17 ± 0,22	16	**PS2**	22 ± 0,16	20
NS1	21 ± 0,34	17	**NS2**	25 ± 0,17	20

Relatively to experimental results showed in Table 9, it is possible to make a comparison within each parameter. For the reference samples, **R**, the largest deviation between experimental and modelled relative densities belongs to **NR** (5% deviation). Regarding the surface thickness, **T**, the sample with the greatest discrepancy between relative densities is **NT1**. A more detailed analysis shows that the above values are not feasible. The fact that **N** is an open cell, but of greater complexity, the extraction of non-sintered powder becomes, in theory, more difficult the greater the thickness is. Since **NT1** has a smaller surface thickness (0,38 mm), its experimental relative density is, in fact, lower than **NR** and **NT2**, but it presents an exaggerated deviation of 9% comparing to CAD model density. Appealing to the logical sense, this relative density should be lower as lowering thickness due to the fact that there is a greater amount of "air" inside each unit cell (lower relative density), which facilitates the extraction of non-sintered dust. As for cell size, **C**, all topologies have close relative densities, excluding **NR** samples. This means that 13,33 x 13,33 mm is the ideal base size of **N** topology for eventual experimental tests and possible comparisons. Regarding the shell thickness, **S**, the larger range corresponds to **N** cellular structures due to the difficulty caused by being a closed cell. The largest difference of 5% in **NR** and **NS2** samples is due to the fact that the general sample sizes remain constant, causes the shell to overlap with the cells. As illustrated in Figure 30, the amount of material encased between the

cells in contact with the shell and the shell is higher in the **NR** samples (shell thickness of 1 mm), which makes the discrepancy larger.

Figure 30 - Shell thickness of Neovius samples: a) without shell (NS1), b) 1 mm (NR) and c) 2 mm of shell thickness (NS2).

In general, the comparison between each cell topology is more precise when it comes to the independent variable **C**, followed by **S** and **T**. However, the **N** cellular structures are the ones that present the greatest discrepancies when compared to the modelled structures. Next, are **P** and, finally, **B**. In order to minimize these discrepancies, it is necessary to take into account the minimum size of the structural cells, essentially in the case of TPMS cells of greater complexity, in order to facilitate the extraction of non-sintered powder. This is because, at the end of each mechanical test, by shaking the sample or even the simple fact of put it on the table, it was possible to observe the non-sintered powder coming out of its interior. During these tests it was also possible to verify the presence of PA2200 powder on the lower Teflon sheet. This happened in greater abundance in **N** samples. Adding to this, possible overheating may have occurred during the manufacture of the samples, inducing the sintering of the neighbor powder.

From the discrepancies described above, it is possible to conclude that the non-sintered powder, present in the samples, did not completely affect the respective mechanical performances of the samples with "defective" relative densities (Figure 31). The mechanical tests were carried out in the same way.

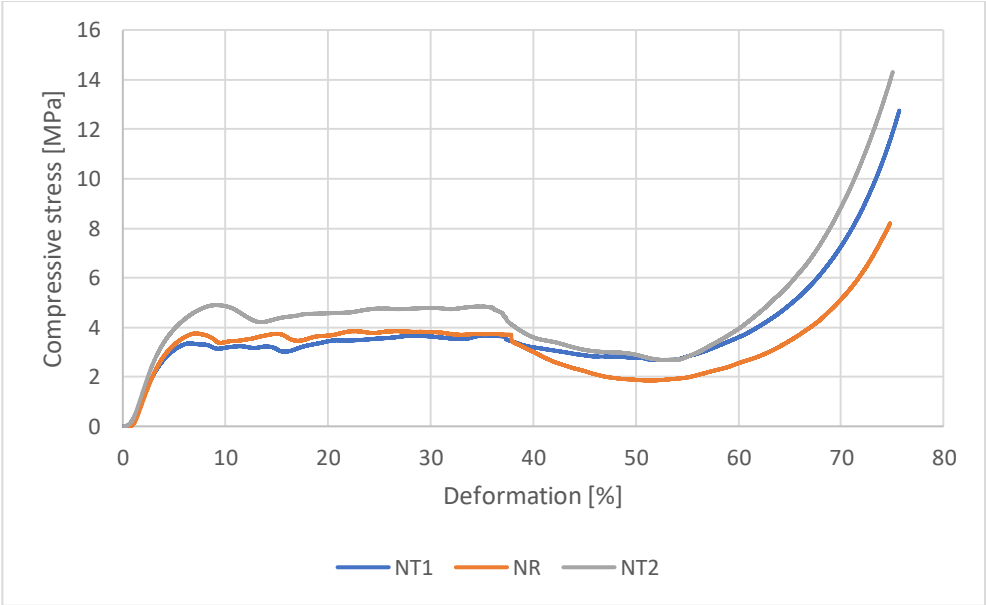

Figure 31 - Compressive stress-strain curves of Neovius surface thicknesses (NT).

4.1.1. Reference samples, R

The study of out-of-plane properties highlights the mechanisms by which cellular solids deform and fail. Starting with the comparative principle that **R** samples are the base variable of each parameter, in each 3 different topologies, their values serve as a comparison for the parameters presented in the following sections.

According to Figure 32, it presents a typical stress-strain curve characteristic of compressive deformation in plastically yielding open cellular solids. That is, the three stages of the deformation of **B**, **P** and **N** lattice structures, such as linear-elastic, plastic plateau and densification stages are showed. So, at a first stage, when the samples are compressed elastically in the z-direction, bending of the cell walls contributes to a homogeneous deformation of the lattice samples. It finishes at yield point which is, approximately, at a strain of 5% for **B**, 3% for **P** and 4% for **N**. At this point, the deformation starts to localize at a plastic plateau of roughly constant strength which sets the post-yield behavior. This differentiating feature of LS samples corresponds as bending-dominated for **B** due to overlapping underlying layers without the occurrence of rupture. Stretching-dominated for **P** and **N** due to the concavities present in stress-strain curves relative to the layer breakage. It ends, approximately, at 45%, 56% and 50% densification strains, in the respective order. The densification occurs between this point until 75% strain.

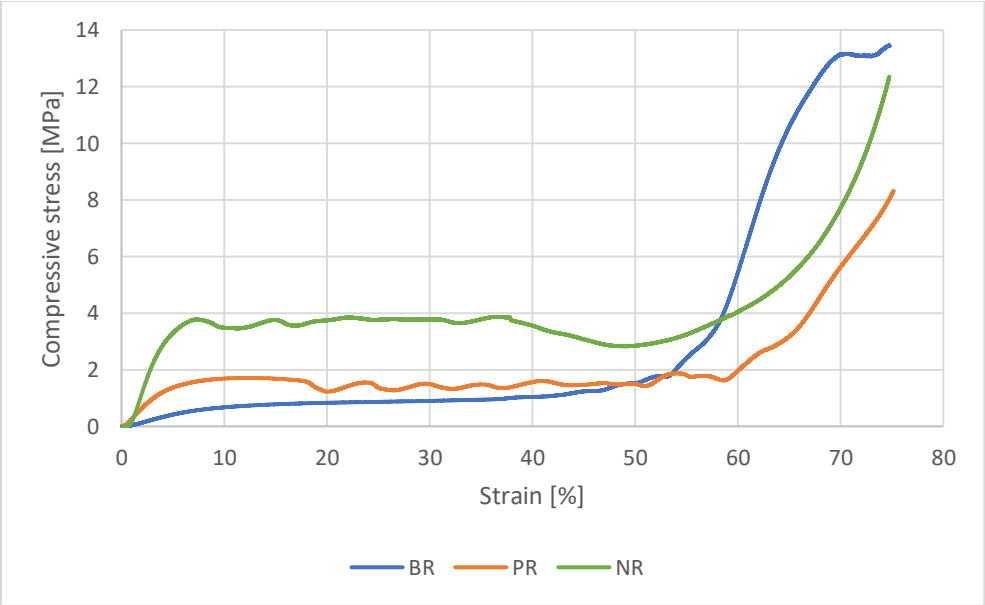

Figure 32 - Compressive stress-strain curves of reference samples (R).

Focusing on the **NR** compressive stress-strain curve, it shows a decrease in strength at, approximately, 38% strain before reaching the densification region. Its wide amplitude that goes beyond the plateau strength draws attention to the fact that there was no cell breakdown, but a significant flexion that provided a slip between the samples and the compressive plates (Figure 33). At a specific strain, the overlapping of the cells provides the slippage of the Teflon sheets which it does not interfere in the results obtained because the densification occurs before these sheets move.

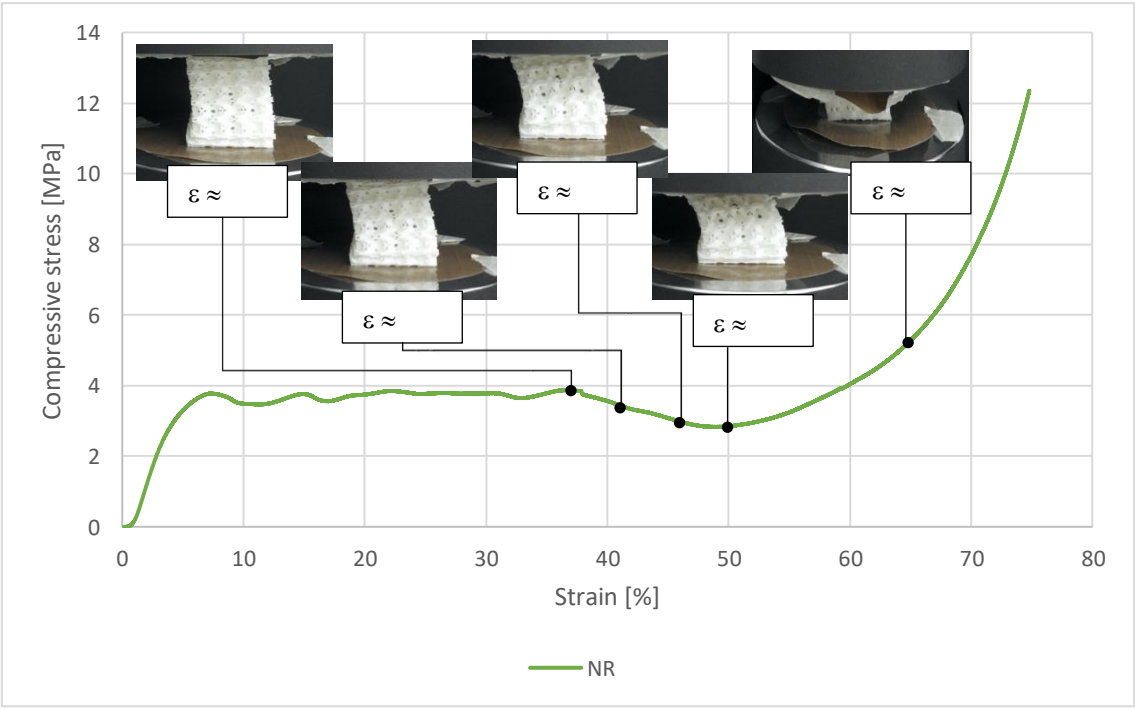

Figure 33 - Representation of the slippage of Teflon sheets during the compressive test.

In general, it is possible to conclude that the compressive behavior is ductile, due to the post peak softening that tends to stabilize in a horizontal plateau, with residual resistance. It should be noted that the critical stresses of the **NR** structure, in comparison with the other topologies, stand out. From the above chart, it was possible to obtain the mechanical properties shown in Table 10.

The **NR** lattice achieves its yield point at a compressive strength and strain of 4,4 kN, and 3,76%, respectively, At this point, **PR** resist around 1,5 kN at 2,98% and **BR** around 0,7 kN at 5,07%. As the yield point occurs to similar strains, the **NR** is the one that presents an improved performance for higher stresses. That is, it would be the most correct option to preserve the structures integrity when submitted to compressive forces. Although the yield point of the three structures seems to occur relatively early, the structures do not recover their initial shape after bearing a load of approximately 67 kg, 153 kg and 432 kg when using BR, PR and NR, respectively. With a remarkable advance, the modulus of elasticity and the plateau strength of **NR** are the largest ones, that is, it is the most rigid structure. This is caused by the fact that the cell is more closed and, by the larger contact area between the unit cells when they are replicated. Due to its high and extended plateau regime, until 50,9 %, a higher energy absorption capacity of 170,7 J is guaranteed.

Although the maximum range between the three densification strains is of 11%, it can be concluded that the absorbed energy is mainly influenced by plateau strength. The greater the plateau strength, the greater the energy absorbed by the lattice structure.

Table 10 – Compressive mechanical properties of reference (R) LS.

	E	σ_Y	ε_Y	ε_D	σ_{pl}	W_D
Units	[MPa]	[MPa]	[%]	[%]	[MPa]	[J]
BR	10,16 ± 0,47	0,42 ± 0,01	5,07 ± 0,10	45,15 ± 2,02	0,86 ± 0,03	35,50 ± 2,66
PR	39,32 ± 0,21	0,96 ± 0,01	2,98 ± 0,05	56,16 ± 3,55	1,50 ± 0,02	81,40 ± 6,20
NR	99,53 ± 2,04	2,72 ± 0,16	3,76 ± 0,20	50,94 ± 1,00	3,53 ± 0,19	170,73 ± 8,26

Note: **E** – Young's Modulus σ_Y – Yield stress ε_Y – Yield strain ε_D – Densification strain σ_{pl} - Plateau stress W_D - Energy absorption

4.1.2. Unit cell parameters

In order to understand the mechanical performance of the LS, this point addresses, in a detailed and individual way, the influence of the surface thickness, unit cell size and shell thickness on the LS.

(i) Surface thickness, T

As one of the most important parameters in the variation of the relative density, the surface thickness has a high importance in the mechanical performance of cellular structures. From Table 3, it is possible to observe the variations in the thickness of the surfaces relative to the reference unit cell, being **T1** of lower thickness and **T2** of upper thickness. Here, the comparison between the results was made separately between the 3 thicknesses, according to each different relative density. Therefore, first the results for **T1** and then **T2** were discussed.

Figure 34 represents the results referring to the lower surface thickness, **T1**. From it, it is possible to observe a better mechanical performance by **NT1**. It reaches a compression yield strength at 3,89 kN. Next one finds the **PT1** with, approximately, 1/3 of the **NT1** force with 1,07 kN. Finally, with a lower compression force at the yield point, comes the **BT1** with 0,35 kN. Regarding the yield strain, it is higher for **BT1** (6,9%), followed by **NT1** (3,5%) and **PT1** (2,9%). The modulus of elasticity of **NT1** is much higher than the other cellular structures, hence being the most rigid structure (Table 11). The plateau region extends to strains of 51,0% for **BT1**, 57,7% for **PT1** and 53,1% for **NT1**. Since the range of densification strains is small, and the plateau strength increases in the order of B, P and N, it is possible to see, from the Figure 37 - c, that the energy absorbed by **NT1** is higher and that of **BT1** is lower. In addition, **PT1** withstands higher loads than **BT1**, equaling between 57% and 65% deformation. From 65% to 75% deformation, **BT1** ends up being stronger than **PT1**. Thus, for the lower surface thickness parameter, the energy absorption is higher for **NT1**.

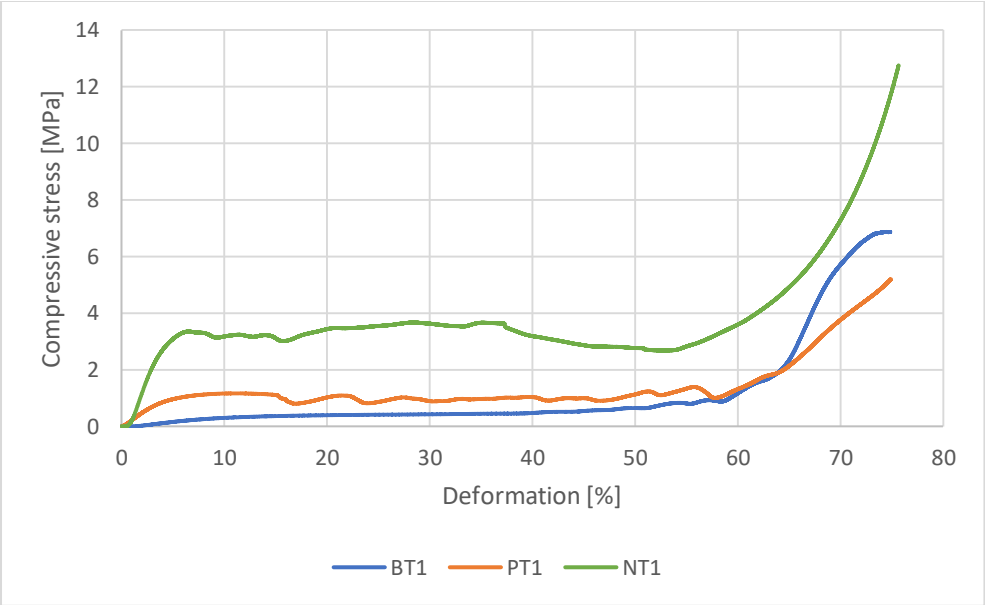

Figure 34 - Compressive stress-strain curves of lower surface thickness (T1).

To enable comparison between results, the Figure 36 represents the curves relating to an increase in surface thickness of the reference unit cells, **T2** (upper surface thickness). But first, it is necessary to report an important fact during the compressive tests of **NT2** that interfere with the coherence of the obtained results: a significant slippage occurred between the tested samples and the compression plates before the densification strain (Figure 35). From the graphic, this effect starts at a strain of, approximately, 36%. ***ρ***

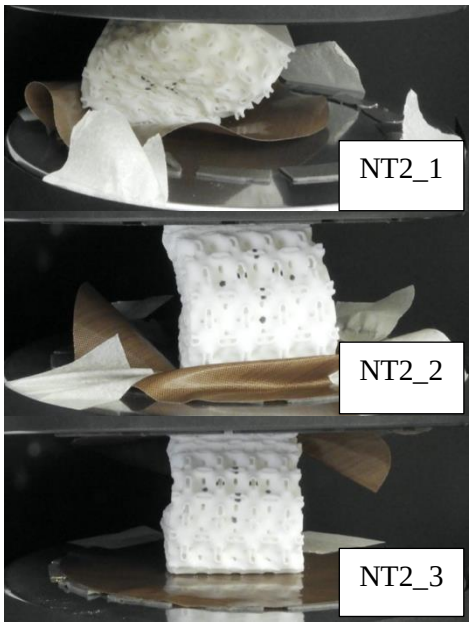

Figure 35 - Slippage of NT2 specimens before the densification strain.

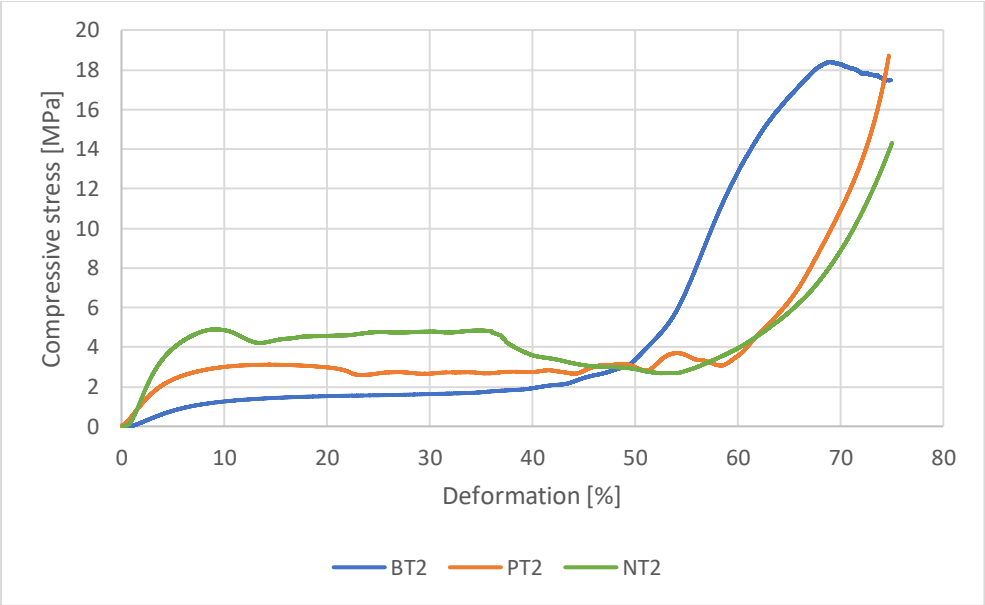

Figure 36 - Compressive stress-strain curves of upper surface thickness (T2).

From Table 11, the resistance of the structures to the compression force at the yield point was higher for **NT2** with a capacity of 5.0 kN, followed by **PT2** with 2.7 kN and **BT2** with 1.1 kN (approximated values). The plateau region extended to 43,1%, 59,0% and 52,7% strain for **BT2**, **PT2** and **NT2**, respectively. Between 49% and 74% of strains, **BT2** has a higher mechanical resistance than the other two, but from 68% strain, its performance is losing quality due to the disassociation of the cells in contact with the shell. Regarding **NT2** and **PT2**, already in the densification regime, they maintained an identical behavior until the end of the test, with **NT2** having a higher resistance.

Despite of the circumstances, the **NT2** structure presents a higher modulus of elasticity as well as a higher capacity of energy absorption. This is due to the fact that there is a larger contact area between the unit cells. An increase in the thickness of cell walls of cellular structures increases the relative density. Then the resistance to cell wall bending and cell collapse goes up, giving a higher modulus and plateau strength. Due to the slip effect that occurred during the trials it can be concluded that it affected the densification strain and plateau strength values. The larger the slippage of the sample, the later the densification occurs.

Table 11 -Compressive properties varying the surface thickness parameter (T).

	E	σ_Y	ε_Y	ε_D	σ_{pl}	W_D
Units	[MPa]	[MPa]	[%]	[%]	[MPa]	[J]
BT1	4,07 ± 0,15	0,22 ± 0,00	6,94 ± 0,03	51,00 ± 0,08	0,43 ± 0,01	19,72 ± 0,45

BR	10,16 ± 0,47	0,42 ± 0,01	5,07 ± 0,10	45,15 ± 2,02	0,86 ± 0,03	35,50 ± 2,66
BT2	21,43 ± 0,41	0,72 ± 0,01	4,62 ± 0,06	43,05 ± 0,12	1,54 ± 0,02	60,53 ± 0,96
PT1	27,07 ± 0,20	0,67 ± 0,00	2,90 ± 0,02	57,69 ± 0,36	1,02 ± 0,01	56,88 ± 0,27
PR	39,32 ± 0,21	0,96 ± 0,01	2,98 ± 0,05	56,16 ± 3,55	1,50 ± 0,02	81,40 ± 6,20
PT2	65,49 ± 4,53	1,68 ± 0,10	2,99 ± 0,01	59,02 ± 0,95	2,74 ± 0,05	155,88 ± 5,60
NT1	97,01 ± 1,30	2,44 ± 0,15	3,51 ± 0,17	53,07 ± 0,92	3,24 ± 0,21	163,83 ± 9,47
NR	99,53 ± 2,04	2,72 ± 0,16	3,76 ± 0,20	50,94 ± 1,00	3,53 ± 0,19	170,73 ± 8,26
NT2	116,61±5,81	3,15 ± 0,18	3,65 ± 0,19	52,65 ± 1,13	4,16 ± 0,29	208,31 ± 12,12

Note: **E** – Young's Modulus σ_Y – Yield stress ε_Y – Yield strain ε_D – Densification strain σ_{pl} - Plateau stress W_D - Energy absorption

In short, the compressive modulus and strength increase with increasing thickness and, consequently, with relative density. From the Figure 37 it is possible to observe that the **N** cellular structure presents better mechanical performance, which is higher the thicker of the surface is. It is also be noted that the variation from **R** structures to **T2** structures is higher than the variation from **T1** to **R** structures.

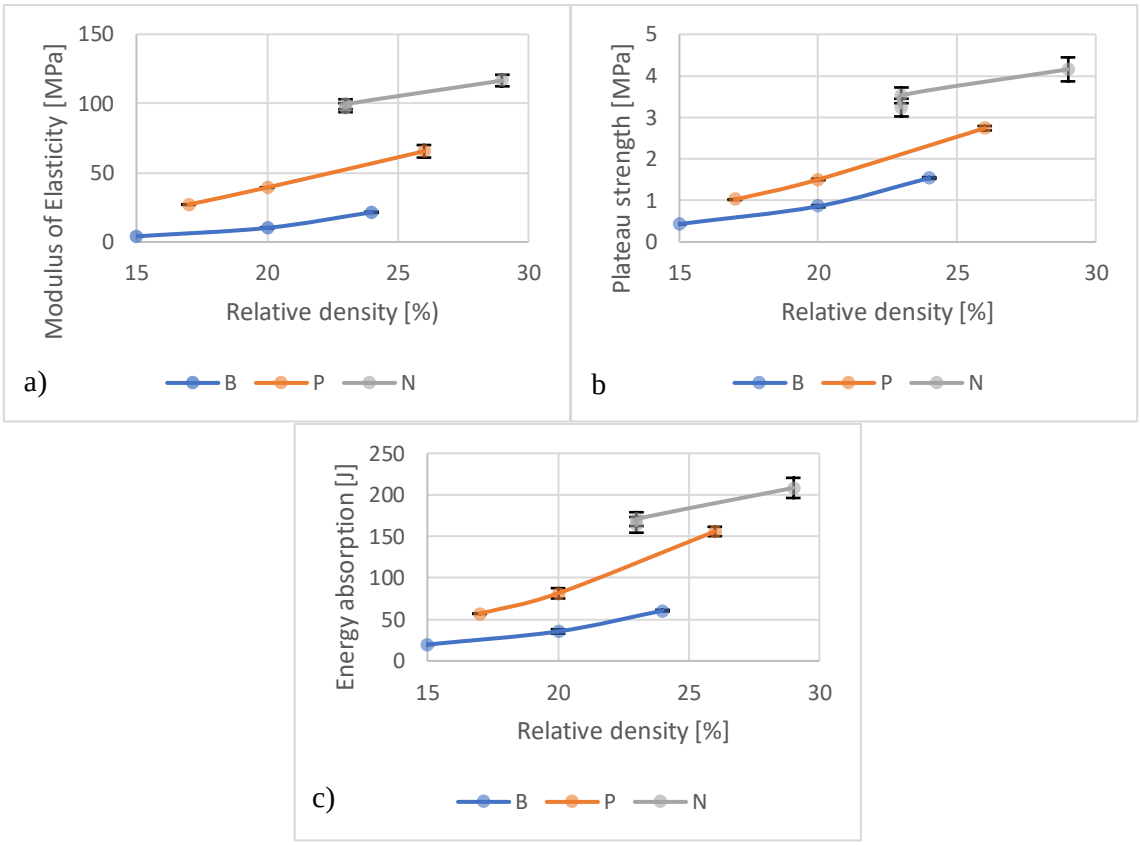

Figure 37 – Compressive (a) modulus, (b) plateau strength and (c) energy absorbed of B, P and N lattice structures at a strain of 1,3 mm/min varying the surface thickness (T).

(ii) Cell size, C

Unlike the parameter described in the previous point, this point deals with the influence on the structural mechanical performance, when the cell size variation is given. Here, the relative density of the standardized unit cell about 17,8% is maintained. Having said this, Figure 38 and Figure 39 represent the compressive stress-strain curves for **C1** and **C2** variations, corresponding to the cubic unit cell sizes of 13,33 mm and 20 mm edge, respectively. The third variant is the reference cell size with 10 mm edge, which was previously discussed in section 4.1.1. As in the reference sample, **NC1** cellular structure suffered the same slippage effect before reaching its densification region, affecting the obtained experimental values, such as, the plateau strength and the densification strain.

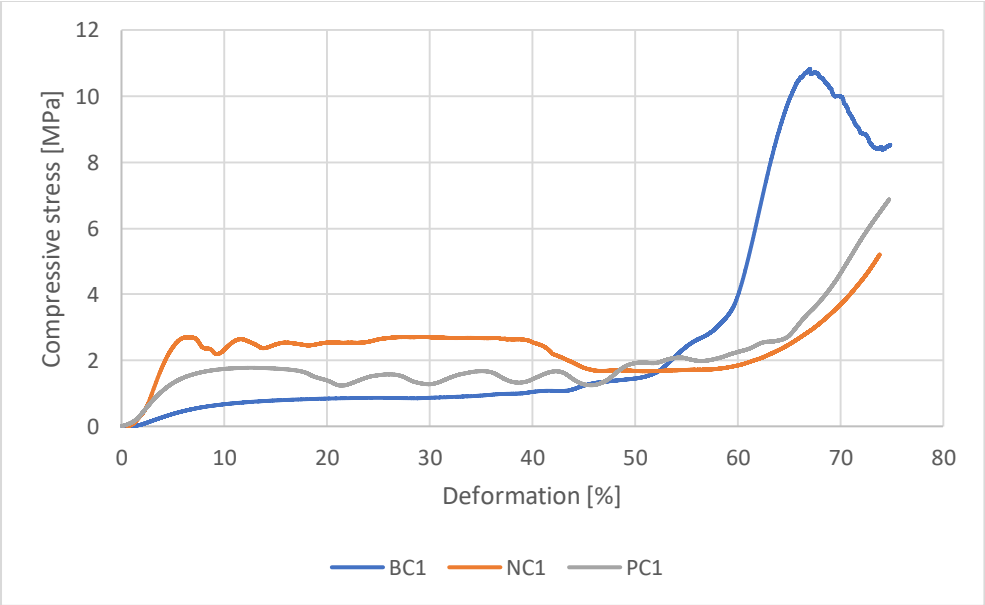

Figure 38 - Compressive stress-strain curves of 13,33 mm cell size (C1).

According to the reported data, Table 12 shows their mechanical properties. Even though certain tabulated values do not correspond to the exact experimental values due to the slippage, **NC1** lattice leads the mechanical performance with a modulus of elasticity of 94,1 MPa and a plateau strength of 2,3 MPa, where densification begins at a deformation of 55,9%. Next comes **PC1** in which the densification begins at 49,4% deformation and, finally, **BC1** with a densification deformation of 45,2%. **BC1**, **PC1** and **NC1** present a planar regime that stagnates at compression forces of approximately 0,8 MPa, 1,5 MPa and 2,3 MPa, respectively, **NC1** being capable of absorbing a greater amount of energy.

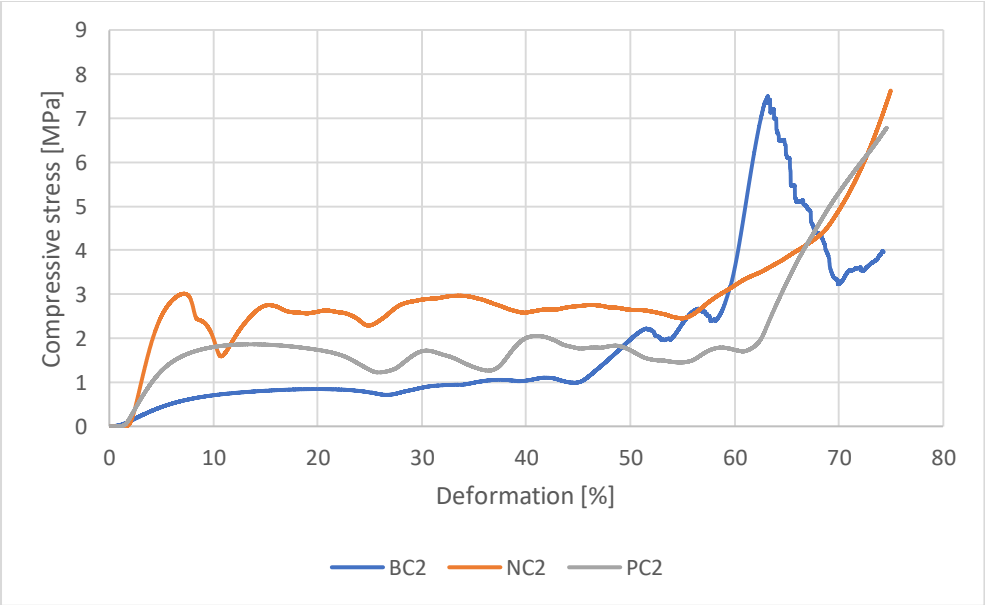

Figure 39 - Compressive stress-strain curves of 20 mm cell size (C2).

Comparatively, it is possible to verify, from the tabulated values extracted from the Figure 39 that the rigidity of **NC2** is greater than other ones when the cell is increased to 20 mm of edge. This structure presents a compressive modulus and strength of 99,6 MPa and 2,6 MPa, respectively, and is capable of absorbing 134,3 J of energy, along a deformation of 54,6%. The second most rigid LS is **PC2** followed by **BC2**. Between the deformation range of 49% - 68%, the **BC2** structures presents higher compressive stress values than **PC2**.

Regarding the final peak, represented in the compressive stress-strain curves for the samples **BC1** and **BC2**, it symbolizes the densification of the cells in the middle of the structure, on the ascent, and the disassociation of the cells with the shell, on the descent.

Table 12 - Compressive mechanical properties by varying the cell size parameter (C).

	E	σ_Y	ε_Y	ε_D	σ_{pl}	W_D
Units	[MPa]	[MPa]	[%]	[%]	[MPa]	[J]
BR	10,16 ± 0,47	0,42 ± 0,01	5,07 ± 0,10	45,15 ± 2,02	0,86 ± 0,03	35,50 ± 2,66
BC1	11,22 ± 0,24	0,39 ± 0,01	5,23 ± 0,32	43,36 ± 0,49	0,84 ± 0,02	32,71 ± 0,48
BC2	11,91 ± 0,27	0,40 ± 0,01	4,54 ± 0,23	44,86 ± 0,45	0,85 ± 0,01	34,92 ± 0,64
PR	39,32 ± 0,21	0,96 ± 0,01	2,98 ± 0,05	56,16 ± 3,55	1,50 ± 0,02	81,40 ± 6,20
PC1	39,51 ± 2,48	1,06 ± 0,11	3,83 ± 0,70	49,39 ± 5,17	1,54 ± 0,10	71,98 ± 10,96

PC2	40,65 ± 0,80	1,11 0,02	±	4,45 0,03	±	61,11 ± 1,03	1,66 0,03	±	95,79 ± 0,76
NR	99,53 ± 2,04	2,72 0,16	±	3,76 0,20	±	50,94 ± 1,00	3,53 0,19	±	170,73 ± 8,26
NC1	94,08 ± 7,73	2,16 0,14	±	4,44 0,02	±	55,94 ± 2,00	2,34 0,24	±	123,04 ± 7,50
NC2	99,63 ± 3,07	2,24 0,06	±	4,51 0,05	±	54,56 ± 1,13	2,62 0,09	±	134,25 ± 5,56

Note: **E** – Young's Modulus σ_Y – Yield stress ε_Y – Yield strain ε_D – Densification strain σ_{pl} - Plateau stress W_D - Energy absorption

According to Figure 40, it is possible to observe how the modulus of elasticity, plateau strength and the energy absorption vary according to the individual use of each topological cell. Having said this, the cell structure with the best mechanical performance is the **NR**. In general, the cellular structures **N** present a mechanical performance superior to the others, with averages values elastic modulus, plateau strength and energy absorption of 97,7 MPa, 2,8 MPa and 142,7 J, respectively. Besides being the most rigid, it presents a greater capacity to absorb energy. According to the topology to be used, the variations in cell sizes **C1** and **C2**, the mechanical performance is identical in **B** and **P** and distinct in **N**. For the first two ones, this means that the increase in cell unit size has little influence on the performance of the cell structures produced.

For the last one, it can show that increasing the cell size parameter, the rigidity of cellular structures is maintained (Figure 40 – a) but altered the energy absorption capacity showed by a significant concavity (Figure 40 – b, c).

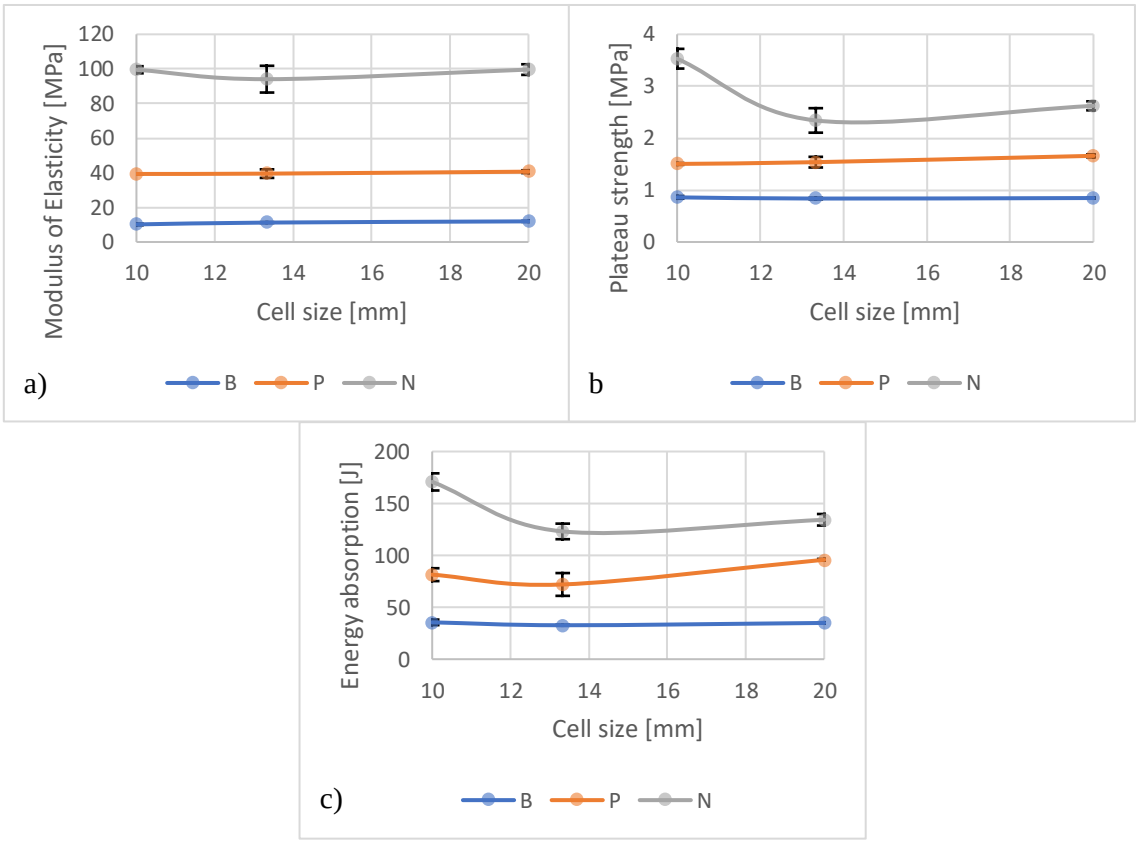

Figure 40 - Compressive a) modulus, b) plateau strength and c) energy absorbed of B, P and N lattice structures, at a compression velocity of 1,3 mm/min varying the cell size (C).

(iii) Shell thickness, S

As the last independent parameter of the unit cell appears the thickness shell. As mentioned in section 3.1.2-c, a variation between 0 to 2 mm has been chosen in order to understand its influence on the mechanical performance of LS. From the compression tests performed, it was possible to trace the stress-strain curves represented in the Figure 41 and Figure 42.

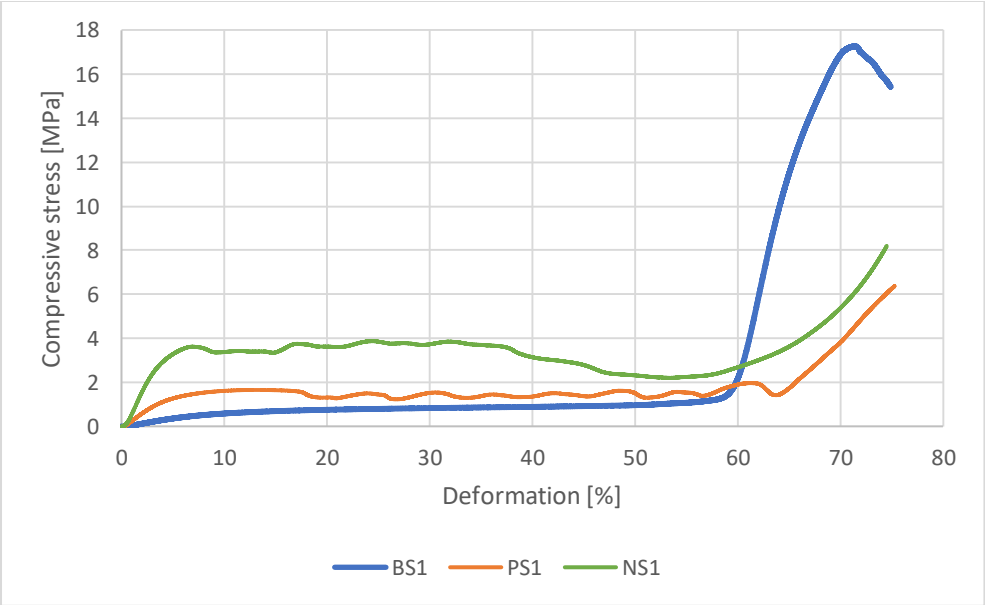

Figure 41 - Compressive stress-strain curves of no-shell thickness (S1).

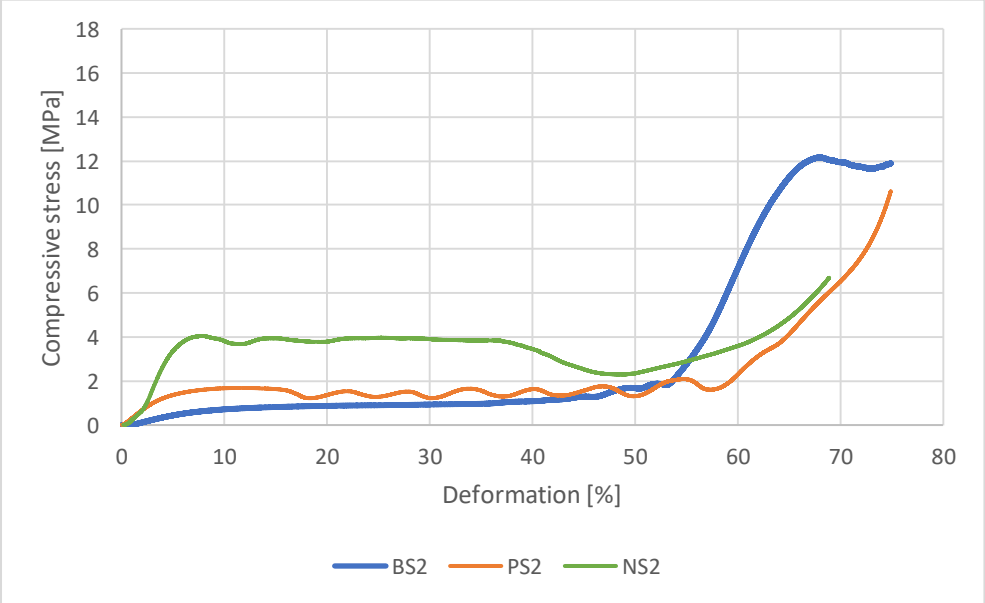

Figure 42 - Compressive stress-strain curves of 2 mm shell thickness (S2).

From the above graphs, it is possible to observe that, by removing the shell (**S1**) or increasing its thickness by 1 mm in relation to the reference thickness (**S2**), there are few differences between the curves, being the densification strain the one that leaps most in sight. For the **BS1** sample, the reason for presenting a later densification strain is that the cells in contact with the plates (without any constraints) behave, throughout the tests, in the same way as the cells present in the center of the sample, which leads to a compressive force applied throughout the

tests being distributed over a larger number of free cells. Such freedom, topology and interaction between neighboring cells provides a higher energy absorption and, consequently, later densification. In the case of **BS2**, where the shells overlap the underlying cells, they maintain their structural integrity throughout the tests and, only in the end, in the region of densification, where they are subject to increased stresses exerted by the neighboring cells, do they deform. These eventually flex or stretch and may even break. This results in the anticipation of densification. The same explanation is adopted for the P and N samples.

After an analysis of the results obtained, Table 13, presents the mechanical properties of the samples in question in order to contribute to a better understanding of the previous paragraph. Regarding the modules of elasticity, these present relatively close values in samples **B** and **P** (9,86 ± 1,11 MPa and 37,65 ± 1,50 MPa, respectively) because the area of contact of the cells, with the increase in shell thickness, is maintained. For **N** samples, it is possible to verify that the increase of the modulus of elasticity increases with the increase of the shell thickness. This indicates that the shell helps to maintain the integrity of the structure, especially of the cells in contact with the shell, due to the increase in the contact area between them (Figure 30). In general, the increase in shell thickness causes a slight increase in plateau strength, and a decrease in densification strain, with a greater amplitude from **S1** to **R**. From **R** to **S2**, there is still a decrease, of lesser amplitude, in the **N** structure, but a slight increase in the **B** and **P** structures. Having said this, it is possible to verify that the absorption energies for **B**, **P** and **N** are around 38,31 ± 2,29 J, 85,74 ± 4,19 J and 170,45 ± 4,26 J, respectively.

Table 13 - Compressive mechanical properties by varying the shell thickness parameter (S).

	E	σ_Y	ε_Y	ε_D	σ_{pl}	W_D
Units	[MPa]	[MPa]	[%]	[%]	[MPa]	[J]
BS1	8,38 ± 0,05	0,36 ± 0,00	5,12 ±.0,05	55,24 ± 0,25	0,80 ± 0,00	41,10 ± 0,38
BR	10,16 ± 0,47	0,42 ± 0,01	5,07 ± 0,10	45,15 ± 2,02	0,86 ± 0,03	35,50 ± 2,66
BS2	11,05 ± 0,21	0,46 ± 0,00	5,22 ± 0,06	46,21 ± 0,12	0,91 ± 0,01	38,33 ± 0,38
PS1	35,69 ± 0,22	0,88 ± 0,01	3,01 ± 0,05	64,10 ± 0,73	1,48 ± 0,01	91,40 ± 1,51
PR	39,32 ± 0,21	0,96 ± 0,01	2,98 ± 0,05	56,16 ± 3,55	1,50 ± 0,02	81,40 ± 6,20
PS2	37,93 ± 0,59	0,99 ± 0,01	3,01 ± 0,04	57,63 ± 0,48	1,52 ± 0,01	84,43 ± 0,49
NS1	96,68 ± 1,56	2,51 ± 0,02	3,20 ± 0,18	55,36 ± 2,16	3,29 ± 0,14	175,52 ± 12,99
NR	99,53 ± 2,04	2,72 ± 0,16	3,76 ± 0,20	50,94 ± 1,00	3,53 ± 0,19	170,73 ± 8,26
NS2	128,36 ± 3,33	2,90 ± 0,05	4,16 ± 0,59	48,72 ± 1,00	3,62 ± 0,19	165,09 ± 6,81

Note: **E** – Young's Modulus σ_Y – Yield stress ε_Y – Yield strain ε_D – Densification strain σ_{pl} - Plateau stress W_D - Energy absorption

In a more succinct and visual way, it is possible to conclude from Figure 43 that the shell thickness is a parameter with little influence on the mechanical performance of cellular structures, when subjected to compression forces. Once again, the discrepancy between the modulus of elasticity of **NR** and **NS2** represented in Figure 43 – a is due to the slippage of the samples in the course of the experimental tests.

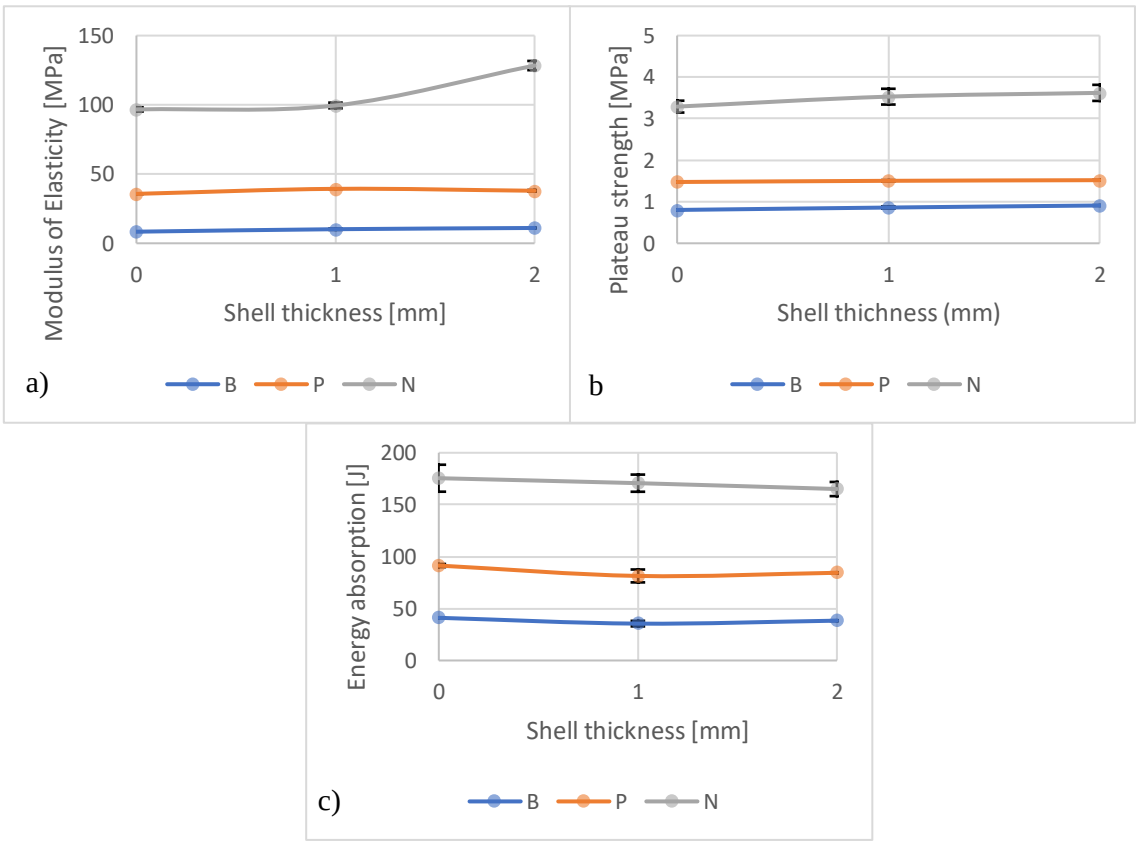

Figure 43 - Compressive a) modulus, b) plateau strength and c) energy absorbed of B, P and N lattice structures, at a compression velocity of 1,3 mm/min varying the shell thickness (S).

4.1.3. Gibson-Ashby formula coefficients

According to the Gibson-Ashby formula, the mechanical properties of cellular materials can be predicted by the Equations 4 a – c described in section 2.5.4 - (ii). Based on previous matrix material test and mechanical parameters of each lattice structure showed in Table 11, Table 12 and Table 13, the compressive elastic modulus and yield strength of matrix material were set as 1532 MPa, and 45 MPa, respectively. In conformity to the relative densities of each lattice structure showed in Table 9, the bending-dominated behavior for **B** and the stretching-dominated

for **P** and **N**, the pre-factors of performance characterization stated as C1, C5, and α were obtained and summarized in Table 14.

Table 14 - Gibson-Ashby formula coefficients of several lattice structures.

	C1	**C5**	**α**		**C1**	**C5**	**α**
	0,1 – 4,0	0,1 - 1	1,4 - 2		0,1 – 4,0	0,1 - 1	1,4 - 2
BR	0,13	0,18	2,43				
PR	0,11	0,15	1,94				
NR	0,24	0,29	1,83				
BT1	0,09	0,13	2,85	**BT2**	0,18	0,23	2,04
PT1	0,09	0,12	2,19	**PT2**	0,14	0,20	1,36
NT1	0,25	0,28	1,82	**NT2**	0,23	0,28	1,42
BC1	0,14	0,17	2,51	**BC2**	0,15	0,18	2,44
PC1	0,11	0,15	2,24	**PC2**	0,12	0,16	1,72
NC1	0,27	0,23	1,95	**NC2**	0,29	0,26	2,01
BS1	0,13	0,19	2,19	**BS2**	0,12	0,16	2,17
PS1	0,12	0,17	1,85	**PS2**	0,10	0,13	1,64
NS1	0,26	0,30	1,81	**NS2**	0,29	0,28	1,77

The C1 and C5 pre-factors of **B**, **P** and **N** structures are within the given ranges. The coefficients of α exceed 2 in all **B** and in **PT1** and **PC1** lattice structures, which is related to the matrix material of PA2200. The toughness of PA2200 is comparatively lower than ordinary plastic lattice after SLS processing. Thus, the densification strain gets smaller in the lattice structures obtained.

4.2. IMPACT TESTS

As in the compression tests, this section reports and discuss the results obtained during the impact tests, according to the two different independent variables of the unit cell, such as, surface and shell thicknesses. During these tests, the impactor energy of 98 J was maintained. For this purpose, in a first analysis, the results relative to the reference sample, R, are addressed. Then, each cell parameter in order to access the impact properties of the produced samples are addressed individually.

Before proceeding to the detailed analysis of the results obtained, it is necessary to mention the dimensional precision and the resulting relative densities. According to the Table 15, it is possible to verify that the produced samples shrink in diameter but expand in height in a higher proportion. Comparing to the modelled dimensional volume, it is obtained the general expansion of the produced samples in a maximum value of 0,67% ± 0,10 belonging to sample **N**.

Table 15 - Dimensional accuracy of impact test samples.

	S1 (%)		
	BCC	**Schwarz – P**	**Neovius**
Diameter	-0,16 ± 0,06	-0,17 ± 0,03	-0,16 ± 0,05
Height	0,81 ± 0,08	0,99 ± 0,26	0,99 ± 0,12
Volume	0,48 ± 0,16	0,64 ± 0,24	0,67 ± 0,10

In comparative terms, between the modelled and experimental relative densities of the produced samples, it is possible to verify, based in Table 16, that there was greater discrepancy between the **N** samples. Such deviations are due to the geometry of the structural cell, making it difficult to extract the non-sintered powder. Once again, the non-sintered powder did not affect the impact properties obtained.

Table 16 - Experimental and modelled relative densities of impact test samples.

	Relative density [%]				
	Experimental	CAD model		Experimental	CAD model
BR	28 ± 0,36	25			
PR	28 ± 0,40	25			
NR	30 ± 0,72	24			
BT1	23 ± 0,15	21	**BT2**	32 ± 0,21	29
PT1	24 ± 0,04	21	**PT2**	32 ± 0,09	29
NT1	25 ± 0,16	20	**NT2**	33 ± 0,99	28
BS1	36 ± 0,25	32	**BS2**	44 ± 0,38	40
PS1	36 ± 0,18	32	**PS2**	44 ± 0,77	39
NS1	37 ± 0,78	32	**NS2**	47 ± 0,12	40

4.2.1. Reference samples, R

The impact tests were performed considering the methodology described above. Figure 44 presents the Force-Deflection curves relative to the R samples. In a general way, the three different curves present an initial ascension of the until a first damage peak. This represents the force necessary to penetrate the upper shell and it occurs before reaching the lattice core. Such peaks are often associated with localized splitting, resulting in the load drop and change in specimen compliance. Then, the local damage stops growing, requiring increased force and energy for the damage to progress further, at maximum force. For **NR** sample, the test ends at a maximum point, where the compaction of the cell layers occurs before the strike reaches the lower

shell. The strike ends up penetrating the sample in its entirety by drag force. In **PR** sample, the unitary constituent cells are capable of further deformation and, consequently, delay the complete penetration of the strike. The fact of the existence of the bottom shell, it also contributed to this delay. Graphically, this effect is represented by the prolongation of the curve, after the maximum peak, and before an abrupt fall of force occurs. For the **BR** sample, after the first damage peak, the force required to break the successive cell layers remains practically constant until the strike penetrates the bottom shell.

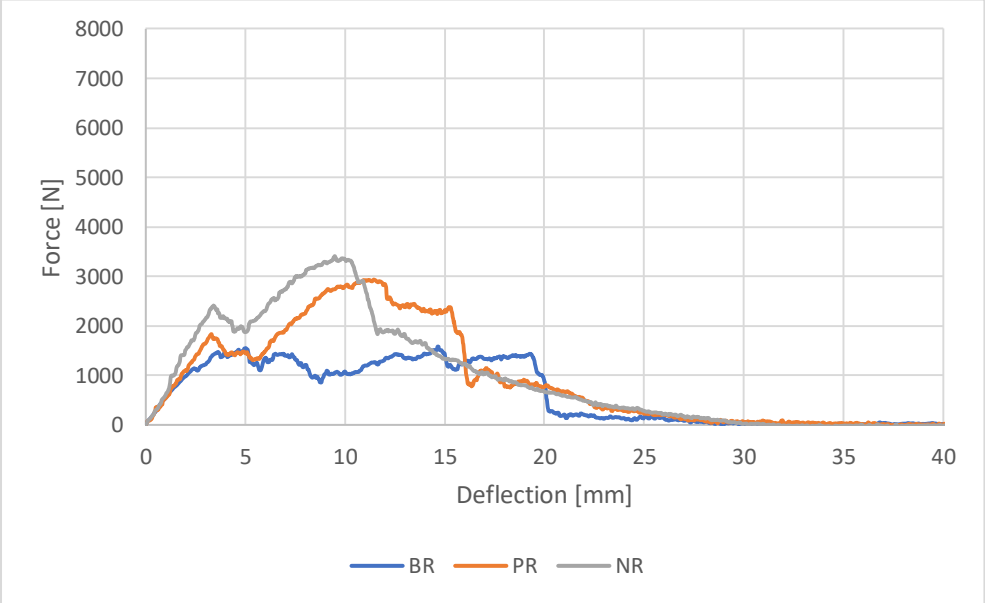

Figure 44 – Impact force-deflection curves of reference test samples (R).

Table 17 represents the **R** impact properties obtained in the experimental tests. From the presented values, it is possible to conclude that **NR** sample resists a maximum impact force of 3527,4 N, followed by **PR** with 2987,3 N and, finally, **BR** with 1930,2 N. Still referring to the maximum peak, although **BR** presents a lower impact capacity than the remaining samples, it is capable of absorbing a greater amount of energy. This is related to the fact that it is reached when the dart is very close to the lower shell, after approximately 17,93 mm. Such maximum peak occurs at deformations of 12,02 mm and 10,03 mm for **P** and **N**, respectively. At the end of the tests, when the puncture point is reached, **PR** is the structure with the highest absorption energy (30,88 J), followed, orderly, by **NR** (28,03 J) and **BR** (22,65 J). The greatest interval of energies, between the maximum point of force and the puncture point, belongs to the **PR** with 9,18 J, which also presents a greater interval traversed by the dart between these same points, with the value of 3,82 mm. That said, **NR** cellular structure is the one with the best of impact force, but **PR** lattice

structure is the one with the best impact absorber. The impact failure of **R** lattice structures consists on a yielding followed by stable cracking.

Table 17 - Impact mechanical properties of the Reference Samples (R).

	Maximum force	Deflection at maximum force	Energy to maximum force	Puncture deflection	Puncture energy
Units	[N]	[mm]	[J]	[mm]	[J]
BR	1930,19 ± 248,22	17,93 ± 2,28	22,10 ± 5,16	18,25 ± 2,18	22,65 ± 5,12
PR	2987,25 ± 128,79	12,02 ± 0,94	21,70 ± 1,83	15,84 ± 0,28	30,88 ± 0,07
NR	3527,38 ± 220,94	10,03 ± 0,51	21,76 ± 1,97	12,57 ± 0,95	28,03 ± 2,67

4.2.2. Unit cell parameters

In order to understand the impact mechanical performance, of each lattice structure, composed by B, P and N topologies, this section makes an individualized characterization of each independent cellular variable, first for the surface thickness and then, for the shell thickness.

(i) Surface thickness, T

Knowing beforehand that the thickness of the unit cells is a parameter with high importance in the mechanical performance of lattice structures when submitted to compressive forces, it was also studied when submitted to an impact force. Despite the different general dimensions between compression and impact samples, thus providing different relative densities, the relative density of the unit cell was maintained in order to compare them.

Before continuing to discuss the results obtained, it is necessary to mention that deformed samples were not accepted due to the force exerted by the closing unit. That said, it is possible to anticipate that only one of the clones of the **BT1** sample underwent a remarkable bending before being tested and was eventually excluded from the study (Figure 45).

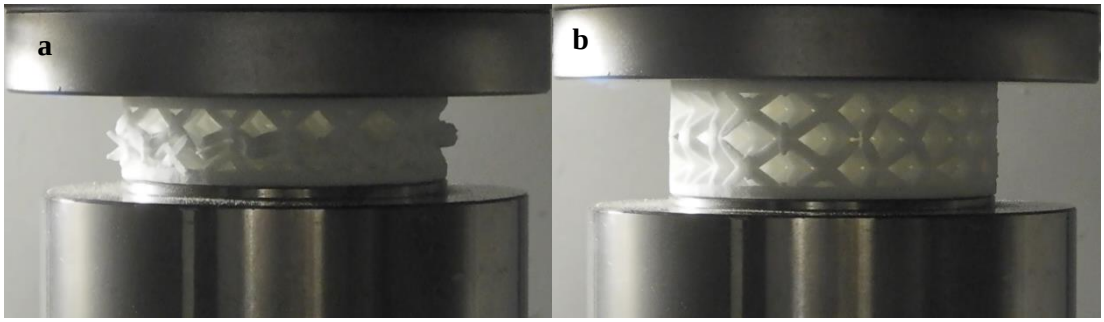

Figure 45 -BT1 test specimen after clamping force: a) with deformation and b) without deformation.

In a quick visual interpretation, it is possible to observe, in Figure 46 and Figure 47 corresponding, respectively, to lower (**T1**) and upper (**T2**) surface thicknesses, that **NT1** resists to higher and **BT1** to lower impact forces for the first ones, and the **PT2** presents the highest and, once again, **BT2** the smallest resistance for the second ones.

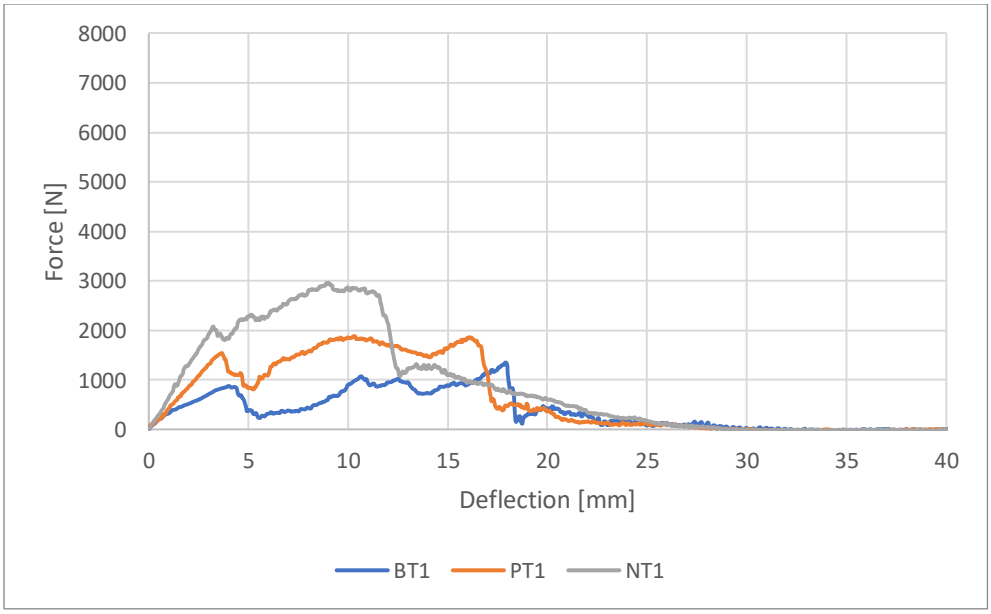

Figure 46 - Impact force-deflection curves of lower surface thickness test samples (T1).

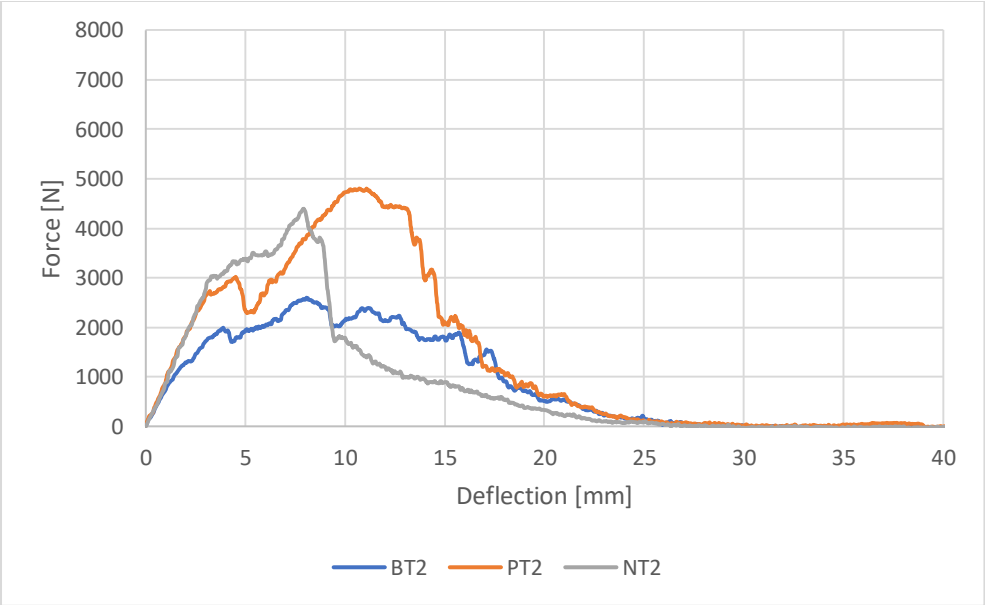

Figure 47 - Impact force-deflection curves of upper surface thickness test samples (T2).

In a more detailed analysis, Table 18 presents the impact properties of greater relevance according to the results obtained.

As for the T1 thickness, the **NT1** has the highest impact rigidity, reaching a maximum force of 2978 N, when the dart penetrates half of the structure. It has the capacity to absorb the highest amount of energy at the peak of maximum force (20,9 J) and its drilling deflection occurs about 2 mm after this peak, capable of absorbing 25,7 J. Secondly, is **PT1,** with 2068 N of maximum force when the dart penetrates 13 mm of the structure. At this point, it has the capacity to absorb 16,9 J. The perforation deflection occurs at approximately 4 mm after this peak of maximum force with an absorption energy of 23,3 J. The use of this cellular topology becomes advantageous due to the greater delay of the perforation deflection, which allows it to absorb a greater amount of energy. Finally, between the three different topologies, **BT1** is the structure that presents lower impact properties. This less rigid structure, besides supporting an impact load of 1348 N, is reached even at the end of the drilling of the dart, at approximately 18 mm. Its energy absorption capacity is around 12,5 J. Due to the initial and final peaks, represented by the curves, it is possible to conclude that the impact failure of the **T1** samples occurred in its entirety. For **NT1**, the final peak is of lesser amplitude and it may be justified by the fact that the lower shell is not able to withstand the impact imposed by the strike, ending up breaking by drag force.

As far as **T2** thickness is concerned, the order of leadership has changed. The result of this increase in surface thickness, allowed **PT2** to reach the greater rigidity with the capacity to withstand 4799 N of maximum force. With about 100 N less, it follows **NT2**. Although **PT2** has a maximum impact force higher than **NT2**, the latter reaches such a force at a lower impactor

deflection, just over 2 mm difference. At the end of the table there is **BT2,** with the capacity to support 2655 N. In terms of energy absorbed, **PT2** is the structure that absorbs the most energy reaching 30,1 J, followed by **NT2** with 23,8 J and, finally, **BT2** with 20,9 J. Once the maximum peak is exceeded, the puncture deflection is analyzed. At this point, it is possible to verify that, among the three topologies, the **PT2** reaches 42,6 J of maximum absorbed energy, after deforming 3 mm. This potentiality lies in the fact that the constituent cells are able to deform easily, leading to a slightly longer shell break than an abrupt one. Regarding **BT2** and **NT2**, **BT2** is able to prolong its deformation in relation to **NT2**, which allows it to absorb more energy before the rupture is complete. The inability of **NT2** to prolong the penetration of the dart and, thus, absorb a greater amount of energy falls on the complex form of the constituent cellular unit. Once again, the resistance that the cell walls exert as the dart pierces the sample is such that, upon reaching a certain point of compaction of the constituent cells, this force is capable of breaking the nearby cells before the dart reaches them. Graphically, this effect is represented by the abrupt post-peak drop of maximum force. Experimentally, the dart is not able to break the sample in its entirety but, by drag force, it ends up doing so.

Table 18 – Impact mechanical properties varying the surface thickness parameter (T).

	Maximum force	**Deflection at maximum force**	**Energy to maximum force**	**Puncture deflection**	**Puncture energy**
Units	[N]	[mm]	[J]	[mm]	[J]
BT1	1348,79 ± 101,57	17,91 ± 0,06	12,47 ± 0,09	18,20 ± 0,17	12,85 ± 0,26
BR	1930,19 ± 248,22	17,93 ± 2,28	22,10 ± 5,16	18,25 ± 2,18	22,65 ± 5,12
BT2	2655,32 ± 348,54	11,62 ± 3,21	20,87 ± 6,25	15,50 ± 1,78	30,34 ± 7,21
PT1	2068,14 ± 38,78	13,04 ± 2,24	16,97 ± 3,68	16,94 ± 0,14	23,39 ± 0,52
PR	2987,25 ± 128,79	12,02 ± 0,94	21,70 ± 1,83	15,84 ± 0,28	30,88 ± 0,07
PT2	4799,11 ± 258,63	10,66 ± 0,58	30,11 ± 3,74	13,71 ± 0,66	42,63 ± 4,95

NT1	2978,45 ± 97,57	10,29 ± 1,18	20,91 ± 3,75	12,14 ± 0,27	25,74 ± 0,80
NR	3527,38 ± 220,94	10,03 ± 0,51	21,76 ± 1,97	12,57 ± 0,95	28,03 ± 2,67
NT2	4695,87 ± 177,34	8,49 ± 0,47	23,75 ± 2,48	8,97 ± 0,43	25,50 ± 2,37

In short, regarding to **T1** thickness, **N** is the most rigid topology, ideal for absorbing impacts. For **T2** thickness, **P** is the ideal lattice structure. Between **T1** and **R** thicknesses, there is a turning point that makes **P**, despite resisting a lower maximum impact force, capable in absorbing a great amount of energy. Between the **R** and **T2** thicknesses there is another turning point. From a certain thickness, **B** is capable of absorbing a greater amount of energy comparing to **N**, and despite having a lower maximum impact force peak. Generally, the greater the cell surface thickness, the greater the stiffness of the cellular structure and, consequently, the lower its deflection. As for the energy absorbed by this type of structures, it also increases with the increase in surface thickness, with the exception of **N**. In topological terms, the unit cell **P** presents a very interesting performance. The use of the ideal topological unit takes into account the specifications of the final product.

(ii) Shell thickness, S

In order to complement the optimization of a cellular structure, the study of the shell thickness appears. To this end, the thickness of the shell was varied in relation to the reference thickness of 1 mm.

The first increase in shell thickness corresponds to 2 mm, **S1**, where the respective curves obtained from the tests performed are represented in the Figure 48. From this, it is possible to verify that the three cellular topologies present a remarkable first damage peak. Focusing individually on each curve, the **BS1** structure presents a decrease in the impact force after the peak, due to the change in the integrity of the first cellular layer by the deflection of the shell. Once the first layer is broken, the impact force tends to stabilize until the end of the test. The force required for the lower and upper shell breakage are similar, which indicates that the cellular compaction is scarce. This effect is noticeably reflected in the absolute deformation of the sample. In **PS1**, the lower shell is the one that most hinders the penetration of the dart (rise of the curve at the end of the test), requiring greater impact force from the striker. Its total rupture occurs through the drag force caused by successive compaction of the cellular layers. In **NS1**, the impact force

achieved by the sample is mostly concentrated in the constituent core that eventually ruptured under the action of the drag force, after reaching maximum compaction. The opportunity for the core to reach such values is contemplated by the presence of the bottom shell. From the curves drawn, Table 19 presents the mechanical properties relative to each cellular sample. From this, it can be seen that **PS1** is the most rigid structure, presenting the highest impact force (4204 N) after a striker penetration of 13 mm. With an intermediate capacity of 4057 N, it follows **NS1** when it is reached by a penetration of, approximately, 10 mm. Finally, with a lower capacity is **BS1** with 1944 N and 17,5 mm of deflection. In the same order, each structure presents 35,1 J, 26,8 J and 21,8 J. After the maximum force peak, at a puncture deflection, **BS1** remained practically unchanged with the rise of approximately 1 J suffering the deflection of 1 mm. **PS1** suffered 1,7 mm of deflection reaching 41 J of absorbed energy. **NS1** suffered a significant deformation in relation to the other structures (4 mm), surprising **PS1** with an impact absorption energy close to 40 J. Although **PS1** is the most rigid cell structure, the parameter **S1** had a greater impact on **NS1**.

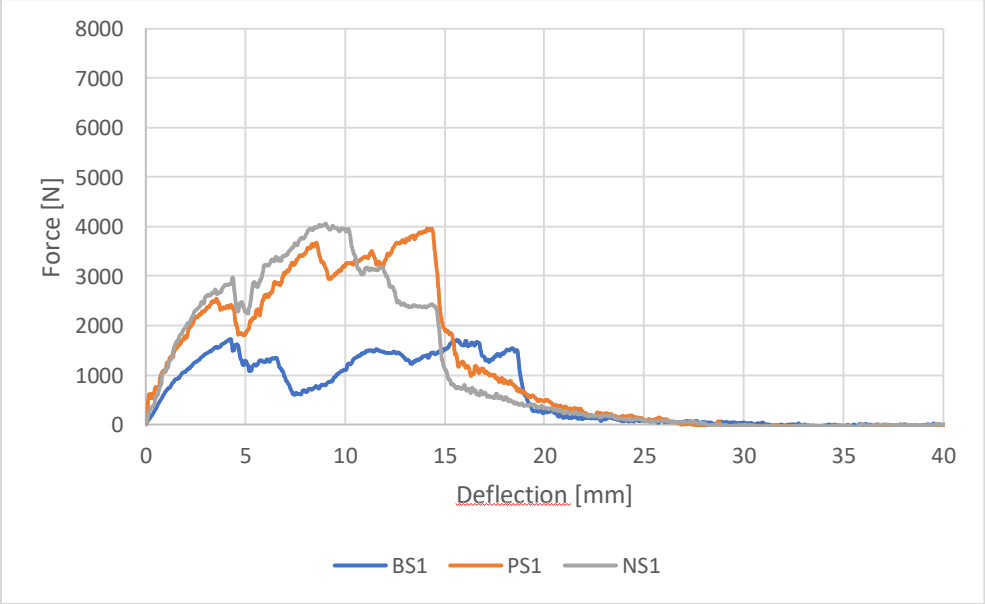

Figure 48 - Impact force-deflection curves of 2 mm shell thickness (S1).

According to the increase in shell thickness corresponding to 3 mm, **S2**, the impact properties for samples **BS2**, **PS2** and **NS2** were not very consistent, and this can be verified from the large standard deviation values presented (Figure 49). Regarding **PS2**, despite the large deviation, it is possible to verify some coherence by the overlapping of the curves of the three clones tested in the first damage peak and in the puncture deflection. In the **BS2** and **NS2** clones' curves, there is little repeatability between samples. To try to decipher the interference of the shell thickness in **NS2,** five samples were tested. Initially 3 samples were tested and NS1_1 sample

was found to be very different from the other ones. In order to understand the exact behavior of **NS2**, two more samples were tested. After all, the behavior tends to the NS1_1 side, but the discrepancy between values is very large. That said, all the samples tested were kept predicting its impact properties.

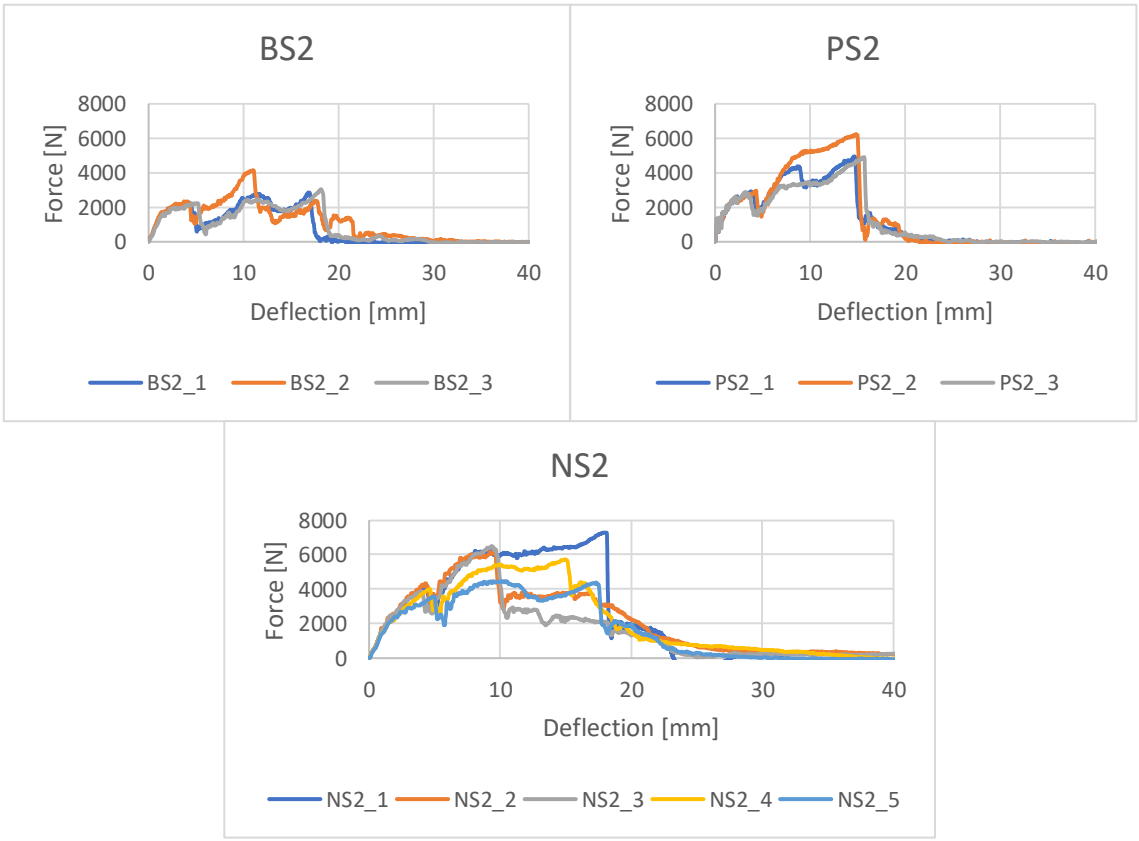

Figure 49 – Impact force versus deflection of the clones of 3 mm shell thickness parameter (S2) in each topology.

From the curves represented in the Figure 50, it is possible to observe the average curves of each structure corresponding to **S2**. From the **BT2** and **PT2** curves it is possible to clearly verify the penetration of the dart through the upper shell (first peak), the core of the samples (second peak) and the lower shell (last peak). For **NT2**, the lower shell is not represented by a last peak, but it is noticed by the decrease of the impact force with negative slope, practically, constant before the sample is penetrated in its totality. The negative slope of the curve is due to a mixture of the breakage of the constituent cells with the help of support of the lower shell. This delays the complete penetration of the striker, which eventually occurs by drag force. According to the values presented in Table 19, it is possible to conclude that **NS2** is the most rigid structure, supporting 6017 N when the structure suffers a deflection of 12,5 mm. At this maximum peak, an amount of energy of 51,3 J is absorbed. When it reaches the perforation deflection, the sample is capable of absorbing 60,9 J after deforming another 2,3 mm. This absorption is possible due to the fact that the sample does not break right after the maximum peak force. Labelled as the second

most rigid, **PS2** is capable of resisting impact forces of 5363 N, deforming 15 mm and absorbing 50,8 J of energy. Finally, **BS2** resists impacts of 3348 N, after penetration of 15 mm of dart. At this point, it is capable of absorbing 21,8 J of energy.

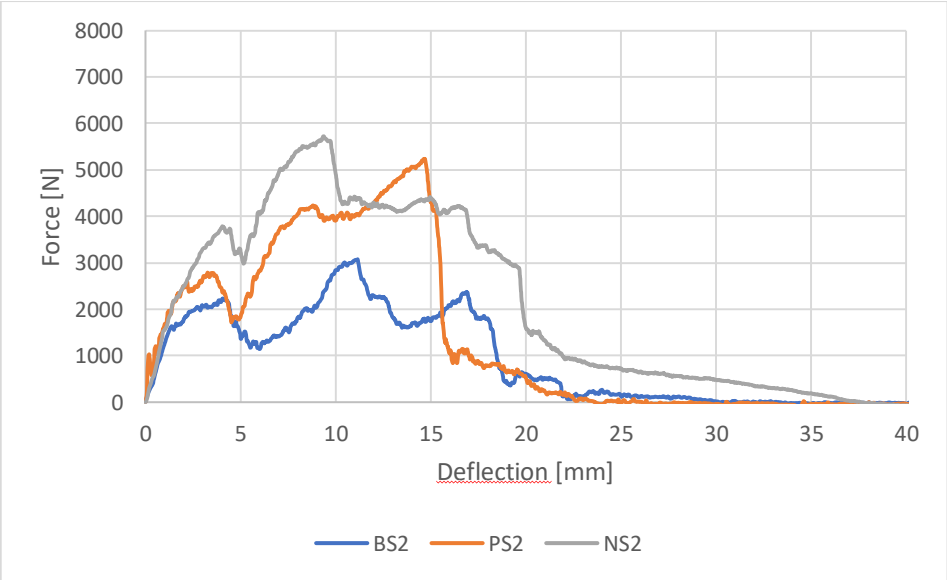

Figure 50 - Impact force-deflection curves of 3 mm shell thickness (S2).

Conclusively, as thickness increases, the greater the standard deviation values obtained. Despite these enormous deviations, the **NS2** cellular structure was still contemplated as the structure with increased mechanical performance. Thus, an increase in a shell thickness leads to an increase in the maximum impact force. The energy absorbed is also greater the greater is its thickness. In terms of deformation of the structure, it is dependent on the cellular topology to be used.

Table 19 - Impact mechanical properties varying the shell thickness parameter (S).

	Maximum force	Deflection at maximum force	Energy to maximum force	Puncture deflection	Puncture genergy
Units	[N]	[mm]	[J]	[mm]	[J]
BR	1930,19 ± 248,22	17,93 ± 2,28	22,10 ± 5,16	18,25 ± 2,18	22,65 ± 5,12
BS1	1944,09 ± 234,77	17,56 ± 0,85	21,76 ± 2,25	18,18 ± 0,92	22,86 ± 2,46
BS2	3348,93 ± 568,72	15,35 ± 3,11	29,38 ± 3,65	15,80 ± 3,03	30,60 ± 3,32
PR	2987,25 ± 128,79	12,02 ± 0,94	21,70 ± 1,83	15,84 ± 0,28	30,88 ± 0,07
PS1	4204,35 ± 65,18	13,25 ± 1,41	35,14 ± 4,78	14,95 ± 0,39	41,12 ± 1,62
PS2	5363,69 ± 617,87	15,09 ± 0,45	50,84 ± 5,17	15,36 ± 0,38	52,10 ± 5,68
NR	3527,38 ± 220,94	10,03 ± 0,51	21,76 ± 1,97	12,57 ± 0,95	28,03 ± 2,67
NS1	4056,59 ± 380.17	9,92 ± 0,24	26,82 ± 1,72	14,01 ± 1,23	39,98 ± 2,31
NS2	6017,34 ± 929,34	12,45 ± 3,53	51,30 ± 22,59	14,78 ± 3,79	60,91 ± 19,68

5. CONCLUSION REMARKS

The manufacture of designed lattice structures from PA 2200 powder is allowed by using the SLS additive manufacturing technique. However, the evaluation of the geometric accuracy revealed some drawbacks of the production and post-production process. According to the modelled and experimental volumes, the dimensional accuracy of the compressive samples shrink in a maximum value of 0,08% ± 0,33 belonging to **N** samples and the impact samples expand in a maximum value of 0,67% ± 0,10 belonging to **N** samples too. The discrepancies between the modeled and produced parts and, consequently, discrepancies in their relative densities, are generally caused by the additive nature of the manufacturing process but can potentially be reduced by optimizing process parameters and/or using powders with different grain size distribution. Besides this effect, being directly related to the relative density, it is also associated to the cellular topology to be used, as well as the variation of each cellular parameters. At issue is the cleaning of samples **B**, **P** and **N**, in which in the first two it is facilitated due to their geometries and in the last one it becomes easier for unit cells above 13,33 mm of side.

This experimental study has presented, detailed compressive and impact mechanical behavior of lattice specimens base on strut-based and TPMS. Regarding compression efforts, for a given relative density, the higher, the more stable (nearly constant) and the longer the stress plateau is, the better is the energy absorption performance. With this, **N** is the topology with the best mechanical performance (NT2: E = 116,61 ± 5,81 MPa; W_D = 208,31 ± 12,12 J), although it has suffered slipping due to the reduction of friction between the contact surfaces of the sample and the compressive plate and, consequently, non-parallel overlapping of the underlying layers. In cellular terms, the parameter that most influences the structural performance is the thickness of the unit cell. In an impact way, the presence of the lattice structure significantly attenuates the peak impact stress transmitted to the specimen, and significantly extends the duration of the load pulse. Although **N** topology is the best structure that adapts best to a mechanical impact response, its strength is improved by the greater the shell thickness (NS2- 60,91 ± 19,68). This is the cellular parameter with greater relevance in the rigidity of a lattice structure. Beside relative densities, it was found that the geometrical design of the cellular cores could also significantly influence the impact energy absorption performance of the LS. It was also found that the impact energy absorption of the cellular structures investigated in this study does not have a significant correlation with compressive mechanical properties.

6. FURTHER RESEARCH

One of the further works of the current research consists, fundamentally, in simulating the samples studied here. From the comparison between the theoretical and experimental values obtained, it will become possible to create a computational model capable of responding to any type of variation at cellular level. Once the specifications of the product in question have been established, the advantage of obtaining relatively close theoretical and experimental results makes it possible to optimize the unit cell and, consequently, the lattice structure formed by it. Do not forget the applied process parameters and mixture powder used in this research, which remained constant for all builds.

Regarding the compression tests, another future work may consist in the elaboration of an equation describing the exponential growth of the mechanical properties as the thickness of the unit cell increases. This will facilitate the implementation of lattice structures in the most diverse applications.

On an experimental level, one of the future challenges lies in finding a way to maintain perpendicularity in the compression of **N** lattice structures. In impact tests, it is necessary to extend the number of samples tested on each cell parameter in order to reduce the sampling error of the mechanical properties obtained. From here, it will be possible to improve the adjustment of the experimental results to the theoretical algorithms.

In addition, the Scanning Electron Microscopy (SEM) analysis on the produced specimens is advised to better understand its morphology, the powders' consolidation and the connection mechanism between the powders in order to optimize the AM process parameters.

REFERENCES

[1] J. Gardan, "Additive manufacturing technologies: State of the art and trends," *Int. J. Prod. Res.*, vol. 54, no. 10, pp. 3118–3132, 2016.

[2] J.-P. Kruth, M. C. Leu, and T. Nakagawa, "Progress in Additive Manufacturing and Rapid Prototyping," *CIRP Ann.*, vol. 47, no. 2, pp. 525–540, 1998.

[3] H. K. D. H. Bhadeshia, *Additive manufacturing*, vol. 32, no. 7. 2016.

[4] W. Gao *et al.*, "The status, challenges, and future of additive manufacturing in engineering," *CAD Comput. Aided Des.*, vol. 69, pp. 65–89, 2015.

[5] D. Bourel, J. Beaman, M. Leu, and D. Rosen, "RAPID History of AM and 2009 Roadmap," *RapidTech 2009 US-TURKEY Work. Rapid Technol.*, pp. 1–8, 2009.

[6] Wohlers Associates Inc., "Wohler's report 2015 - 3D printing and additive manufacturing state of the industry. Annual Worldwide Progress Report.," *Wohlers Rep. 2012*, pp. 32–42, 2015.

[7] M. Richardson, "Designer/Maker: The Rise of Additive Manufacturing, Domestic-Scale Production and the Possible Implications for the Automotive Industry," *Comput. Aided. Des. Appl.*, vol. PACE, no. 2, pp. 33–48, 2012.

[8] T. D. Ngo, A. Kashani, G. Imbalzano, K. T. Q. Nguyen, and D. Hui, "Additive manufacturing (3D printing): A review of materials, methods, applications and challenges," *Compos. Part B Eng.*, vol. 143, no. December 2017, pp. 172–196, 2018.

[9] ASTM International, "F2792-12a - Standard Terminology for Additive Manufacturing Technologies," *Rapid Manuf. Assoc.*, pp. 10–12, 2013.

[10] V. Petrovic, J. Vicente Haro Gonzalez, O. Jordá Ferrando, J. Delgado Gordillo, J. Ramon Blasco Puchades, and L. Portoles Grinan, "Additive layered manufacturing: Sectors of industrial application shown through case studies," *Int. J. Prod. Res.*, vol. 49, no. 4, pp. 1061–1079, 2011.

[11] G. N. Levy, R. Schindel, and J. P. Kruth, "Rapid manufacturing and rapid tooling with layer manufacturing (LM) technologies, state of the art and future perspectives," *CIRP Ann. - Manuf. Technol.*, vol. 52, no. 2, pp. 589–609, 2003.

[12] J. A. Slotwinski, "Additive manufacturing: Overview and NDE challenges," *AIP Conf. Proc.*, vol. 1581 33, no. 2014, pp. 1173–1177, 2014.

[13] I. Gibson, D. Rosen, and B. Stucker, *Directed Energy Deposition Processes. In: Additive Manufacturing Technologies*. 2015.

[14] D. Bourell *et al.*, "Materials for additive manufacturing," *CIRP Ann. - Manuf. Technol.*, vol. 66, no. 2, pp. 659–681, 2017.

[15] N. Guo and M. C. Leu, "Additive manufacturing: Technology, applications and research needs," *Front. Mech. Eng.*, vol. 8, no. 3, pp. 215–243, 2013.

[16] W. E. Frazier, "Metal additive manufacturing: A review," *J. Mater. Eng. Perform.*, vol. 23, no. 6, pp. 1917–1928, 2014.

[17] K. V. Wong and A. Hernandez, "A Review of Additive Manufacturing," *ISRN Mech. Eng.*, vol. 2012, pp. 1–10, 2012.

[18] J. R. C. Dizon, A. H. Espera, Q. Chen, and R. C. Advincula, "Mechanical characterization of 3D-printed polymers," *Addit. Manuf.*, vol. 20, no. December, pp. 44–67, 2018.

[19] J. P. Kruth, "Material Incress Manufacturing by Rapid Prototyping Techniques," *CIRP Ann. - Manuf. Technol.*, vol. 40, no. 2, pp. 603–614, 1991.

[20] F. Calignano *et al.*, "Overview on additive manufacturing technologies," *Proc. IEEE*, vol. 105, no. 4, pp. 593–612, 2017.

[21] C. M. González-Henríquez, M. A. Sarabia-Vallejos, and J. Rodriguez-Hernandez, "Polymers for additive manufacturing and 4D-printing: Materials, methodologies, and biomedical applications," *Prog. Polym. Sci.*, vol. 94, pp. 57–116, 2019.

[22] "Home - Optomec." [Online]. Available: https://optomec.com/. [Accessed: 17-Sep-2020].

[23] "About Arcam | GE Additive." [Online]. Available: https://www.ge.com/additive/who-we-are/about-arcam. [Accessed: 17-Sep-2020].

[24] "Concept Laser | GE Additive." [Online]. Available: https://www.ge.com/additive/de/who-we-are/concept-laser. [Accessed: 17-Sep-2020].

[25] "GE Aviation acquires Morris Technologies and Rapid Quality Manufacturing | GE Aviation." [Online]. Available: https://www.geaviation.com/press-release/other-news-information/ge-aviation-acquires-morris-technologies-and-rapid-quality. [Accessed: 17-Sep-2020].

[26] R. Leal *et al.*, "Additive manufacturing tooling for the automotive industry," *Int. J. Adv. Manuf. Technol.*, vol. 92, no. 5, pp. 1671–1676, 2017.

[27] M. Salmi, K. S. Paloheimo, J. Tuomi, J. Wolff, and A. Mäkitie, "Accuracy of medical

models made by additive manufacturing (rapid manufacturing)," *J. Cranio-Maxillofacial Surg.*, vol. 41, no. 7, pp. 603–609, 2013.

[28] M. Javaid and A. Haleem, "Additive manufacturing applications in medical cases: A literature based review," *Alexandria J. Med.*, vol. 54, no. 4, pp. 411–422, 2018.

[29] C. M. González-Henríquez, M. A. Sarabia-Vallejos, and J. R. Hernandez, "Antimicrobial polymers for additive manufacturing," *Int. J. Mol. Sci.*, vol. 20, no. 5, 2019.

[30] R. Huang *et al.*, "Energy and emissions saving potential of additive manufacturing: the case of lightweight aircraft components," *J. Clean. Prod.*, vol. 135, pp. 1559–1570, 2016.

[31] A. Zhakeyev, P. Wang, L. Zhang, W. Shu, H. Wang, and J. Xuan, "Additive Manufacturing: Unlocking the Evolution of Energy Materials," *Adv. Sci.*, vol. 4, no. 10, 2017.

[32] B. Berman, "3-D printing: The new industrial revolution," *Bus. Horiz.*, vol. 55, no. 2, pp. 155–162, 2012.

[33] D. Mac Sithigh, "When the Dealin's Done: Recent Developments in Online Gambling Law and Policy.," *SCRIPTed*, vol. 11(2), no. 1, p. 171, 2014.

[34] M. Attaran, "The rise of 3-D printing: The advantages of additive manufacturing over traditional manufacturing," *Bus. Horiz.*, vol. 60, no. 5, pp. 677–688, 2017.

[35] G. Harsha Vardhan, G. H. Charan, P. V. S. Reddy, and K. Sampath Kumar, "International Journal on Recent and Innovation Trends in Computing and Communication 3D Printing: The Dawn of a New Era in Manufacturing," no. August, pp. 2373–2376, 2014.

[36] B. Sedacca, "Hand built by lasers," *Eng. Technol.*, vol. 6, no. 1, pp. 58–59, 2011.

[37] M. Leino, J. Pekkarinen, and R. Soukka, "The role of laser additive manufacturing methods of metals in repair, refurbishment and remanufacturing - Enabling circular economy," *Phys. Procedia*, vol. 83, pp. 752–760, 2016.

[38] *Series Editors*. 2002.

[39] D. L. (The U. of T. at A.) Bourell, M. C. (Missouri U. of S. and T.) Leu, and D. W. (Georgia I. of T.) Rosen, "Roadmap for Additive Manufacturing," *Univ. Texas Austin*, p. 92, 2009.

[40] X. Wang, M. Jiang, Z. Zhou, J. Gou, and D. Hui, "3D printing of polymer matrix composites: A review and prospective," *Compos. Part B Eng.*, vol. 110, pp. 442–458,

2017.

[41] J. Z. Manapat, Q. Chen, P. Ye, and R. C. Advincula, “3D Printing of Polymer Nanocomposites via Stereolithography,” *Macromol. Mater. Eng.*, vol. 302, no. 9, pp. 1–13, 2017.

[42] B. Stucker, “Additive Manufacturing Technologies: Technology Introduction and Business Implications,” *Front. Eng. 2011 Reports Leading-Edge Eng. from 2011 Symp.*, vol. 0, p. pages 1-9, 2012.

[43] J. Klingelnberg, *Manufacturing Process*. Elsevier Inc., 2016.

[44] P. Calvert, “Inkjet printing for materials and devices,” *Chem. Mater.*, vol. 13, no. 10, pp. 3299–3305, 2001.

[45] Hue P. Le, “Progress and Trends in Ink-jet Printing Technology,” *J. Imaging Sci. Technol.*, vol. 42, no. 1, pp. 49–62, 1998.

[46] B. J. De Gans, P. C. Duineveld, and U. S. Schubert, “Inkjet printing of polymers: State of the art and future developments,” *Adv. Mater.*, vol. 16, no. 3, pp. 203–213, 2004.

[47] Redwood Ben, “Additive Manufacturing Technologies: An Overview | 3D Hubs,” *Knowledge base*, 2017. [Online]. Available: https://www.3dhubs.com/knowledge-base/additive-manufacturing-technologies-overview/. [Accessed: 17-Sep-2020].

[48] “Material jetting - MJ, NPJ, DOD | Make.” [Online]. Available: https://make.3dexperience.3ds.com/processes/material-jetting. [Accessed: 03-Mar-2021].

[49] “Sheet Lamination| Additive Manufacturing Research Group | Loughborough University,” 2019. [Online]. Available: https://www.lboro.ac.uk/research/amrg/about/the7categoriesofadditivemanufacturing/sheetlamination/. [Accessed: 17-Sep-2020].

[50] I. Gibson, D. W. Rosen, and B. Stucker, “Additive manufacturing technologies: Rapid prototyping to direct digital manufacturing,” *Addit. Manuf. Technol. Rapid Prototyp. to Direct Digit. Manuf.*, no. 1991, pp. 1–459, 2010.

[51] E. MacDonald and R. Wicker, “Multiprocess 3D printing for increasing component functionality,” *Science (80-.).*, vol. 353, no. 6307, 2016.

[52] J. Y. Lee, J. An, and C. K. Chua, “Fundamentals and applications of 3D printing for novel materials,” *Appl. Mater. Today*, vol. 7, pp. 120–133, 2017.

[53] S. H. Huang, P. Liu, A. Mokasdar, and L. Hou, “Additive manufacturing and its societal

impact: A literature review," *Int. J. Adv. Manuf. Technol.*, vol. 67, no. 5–8, pp. 1191–1203, 2013.

[54] J. Shah, B. Snider, T. Clarke, S. Kozutsky, M. Lacki, and A. Hosseini, "Large-scale 3D printers for additive manufacturing: design considerations and challenges," *Int. J. Adv. Manuf. Technol.*, vol. 104, no. 9–12, pp. 3679–3693, 2019.

[55] R. Langdon, *Rapid prototyping*, vol. 23, no. 5. 1998.

[56] P. Kocovic, *3D Printing and Its Impact on the Production of Fully Functional Components*. 2017.

[57] "Selective Laser Sintering Equipment Market by Material & Industry - Global Forecast to 2023 | MarketsandMarkets." [Online]. Available: https://www.marketsandmarkets.com/Market-Reports/selective-laser-sintering-equipment-market-27853684.html. [Accessed: 17-Sep-2020].

[58] D. King and T. Tansey, "Alternative materials for rapid tooling," *J. Mater. Process. Technol.*, vol. 121, no. 2–3, pp. 313–317, 2002.

[59] M. Król, M. Kujawa, L. A. Dobrzański, and T. Tański, "Influence of technological parameters on additive manufacturing steel parts in Selective Laser Sintering," *Arch. Mater. Sci. Eng.*, vol. 67, no. 2, pp. 84–92, 2014.

[60] S. Singh, S. Ramakrishna, and R. Singh, "Material issues in additive manufacturing: A review," *J. Manuf. Process.*, vol. 25, pp. 185–200, 2017.

[61] X. Li *et al.*, "Thermal simulation of the cooling down of selective laser sintered parts in PA12," *Rapid Prototyp. J.*, vol. 24, no. 7, pp. 1117–1123, 2018.

[62] D. T. Pham, K. D. Dotchev, and W. A. Y. Yusoff, "Deterioration of polyamide powder properties in the laser sintering process," *Proc. Inst. Mech. Eng. Part C J. Mech. Eng. Sci.*, vol. 222, no. 11, pp. 2163–2176, 2008.

[63] "How does additive manufacturing work?" [Online]. Available: https://www.eos.info/en/industrial-3d-printing/additive-manufacturing-how-it-works. [Accessed: 07-Jan-2021].

[64] S. Kumar, "Selective Laser Sintering: A Qualitative and Objective Approach," *Jom*, vol. 55, no. 10, pp. 43–47, 2003.

[65] M. Schmid, A. Amado, and K. Wegener, "Polymer powders for selective laser sintering (SLS)," *AIP Conf. Proc.*, vol. 1664, 2015.

[66] A. T. Sutton, C. S. Kriewall, M. C. Leu, and J. W. Newkirk, “Powder characterisation techniques and effects of powder characteristics on part properties in powder-bed fusion processes,” *Virtual Phys. Prototyp.*, vol. 12, no. 1, pp. 3–29, 2017.

[67] G. M. Vasquez, C. E. Majewski, B. Haworth, and N. Hopkinson, “A targeted material selection process for polymers in laser sintering,” *Addit. Manuf.*, vol. 1, pp. 127–138, 2014.

[68] J. Kruth, G. Levy, R. Schindel, T. Craeghs, and E. Yasa, “Consolidation of Polymer Powders by Selective Laser Sintering_PMI08_Kruth_Levy_Keynote.”

[69] S. Singh, V. S. Sharma, and A. Sachdeva, “Progress in selective laser sintering using metallic powders: A review,” *Mater. Sci. Technol. (United Kingdom)*, vol. 32, no. 8, pp. 760–772, 2016.

[70] S. Berretta, O. Ghita, and K. E. Evans, “Morphology of polymeric powders in Laser Sintering (LS): From Polyamide to new PEEK powders,” *Eur. Polym. J.*, vol. 59, pp. 218–229, 2014.

[71] J. D. Williams and C. R. Deckard, “Emerald Article : Advances in modeling the effects of selected parameters on the SLS process Advances in modeling the effects of selected parameters on the SLS process,” *Group*, vol. 4, no. 2, pp. 90–100, 2011.

[72] W. S. Tan, C. K. Chua, T. H. Chong, A. G. Fane, and A. Jia, “3D printing by selective laser sintering of polypropylene feed channel spacers for spiral wound membrane modules for the water industry,” *Virtual Phys. Prototyp.*, vol. 11, no. 3, pp. 151–158, 2016.

[73] S. Singh, V. S. Sharma, A. Sachdeva, and S. K. Sinha, “Optimization and analysis of mechanical properties for selective laser sintered polyamide parts,” *Mater. Manuf. Process.*, vol. 28, no. 2, pp. 163–172, 2013.

[74] D. L. Bourell, T. J. Watt, D. K. Leigh, and B. Fulcher, “Performance limitations in polymer laser sintering,” *Phys. Procedia*, vol. 56, no. C, pp. 147–156, 2014.

[75] C. A. Chatham, T. E. Long, and C. B. Williams, “A review of the process physics and material screening methods for polymer powder bed fusion additive manufacturing,” *Prog. Polym. Sci.*, vol. 93, pp. 68–95, 2019.

[76] B. Leutenecker-Twelsiek, C. Klahn, and M. Meboldt, “Considering Part Orientation in Design for Additive Manufacturing,” *Procedia CIRP*, vol. 50, pp. 408–413, 2016.

[77] U. Ajoku, N. Hopkinson, and M. Caine, “Experimental measurement and finite element modelling of the compressive properties of laser sintered Nylon-12,” *Mater. Sci. Eng. A*,

vol. 428, no. 1–2, pp. 211–216, 2006.

[78] B. Caulfield, P. E. McHugh, and S. Lohfeld, “Dependence of mechanical properties of polyamide components on build parameters in the SLS process,” *J. Mater. Process. Technol.*, vol. 182, no. 1–3, pp. 477–488, 2007.

[79] P. Titanium and I. Anisotropy, “<MECHANICAL PROPERTIES OF SELECTIVE LASER MELTED AlSi10Mg.pdf>,” 2020.

[80] I. Gibson and D. Shi, “Material properties and fabrication parameters in selective laser sintering process,” *Rapid Prototyp. J.*, vol. 3, no. 4, pp. 129–136, 1997.

[81] X. Wang and T. Laoui, “To cite this document : Lasers and materials in selective laser sintering,” vol. 23, no. 4, pp. 357–371, 2006.

[82] E. O. Olakanmi, R. F. Cochrane, and K. W. Dalgarno, “A review on selective laser sintering/melting (SLS/SLM) of aluminium alloy powders: Processing, microstructure, and properties,” *Prog. Mater. Sci.*, vol. 74, pp. 401–477, 2015.

[83] S. C. Ligon, R. Liska, J. Stampfl, M. Gurr, and R. Mülhaupt, “Polymers for 3D Printing and Customized Additive Manufacturing,” *Chem. Rev.*, vol. 117, no. 15, pp. 10212–10290, 2017.

[84] C. Y. Yap *et al.*, “Review of selective laser melting: Materials and applications,” *Appl. Phys. Rev.*, vol. 2, no. 4, 2015.

[85] F. W. Zok, R. M. Latture, and M. R. Begley, “Periodic truss structures,” *J. Mech. Phys. Solids*, vol. 96, pp. 184–203, 2016.

[86] D. Mahmoud and M. Elbestawi, “Lattice Structures and Functionally Graded Materials Applications in Additive Manufacturing of Orthopedic Implants: A Review,” *J. Manuf. Mater. Process.*, vol. 1, no. 2, p. 13, Oct. 2017.

[87] S. C. Han, J. W. Lee, and K. Kang, “A New Type of Low Density Material: Shellular,” *Adv. Mater.*, vol. 27, no. 37, pp. 5506–5511, 2015.

[88] K. J. Kang, “Wire-woven cellular metals: The present and future,” *Prog. Mater. Sci.*, vol. 69, pp. 213–307, 2015.

[89] H. N. G. Wadley, N. A. Fleck, and A. G. Evans, “Fabrication and structural performance of periodic cellular metal sandwich structures,” *Compos. Sci. Technol.*, vol. 63, no. 16, pp. 2331–2343, 2003.

[90] T. Maconachie *et al.*, “SLM lattice structures: Properties, performance, applications and

challenges," *Mater. Des.*, vol. 183, p. 108137, 2019.

[91] D. Li, W. Liao, N. Dai, G. Dong, Y. Tang, and Y. M. Xie, "Optimal design and modeling of gyroid-based functionally graded cellular structures for additive manufacturing," *CAD Comput. Aided Des.*, vol. 104, pp. 87–99, 2018.

[92] M. Helou and S. Kara, "Design, analysis and manufacturing of lattice structures: An overview," *Int. J. Comput. Integr. Manuf.*, vol. 31, no. 3, pp. 243–261, 2018.

[93] T. Tancogne-Dejean, A. B. Spierings, and D. Mohr, "Additively-manufactured metallic micro-lattice materials for high specific energy absorption under static and dynamic loading," *Acta Mater.*, vol. 116, pp. 14–28, 2016.

[94] P. Dziewit, P. Paweł, J. Janiszewski, M. Sarzyński, M. Grązka, and P. Robert, "Mechanical Response of Additive Manufactured Regular Cel Structures in Quasi-Static Loading Conditions - Part I Experimental Investigations," *Chest*, vol. 148, no. 4, p. 558A, 2017.

[95] M. G. Rashed, M. Ashraf, R. A. W. Mines, and P. J. Hazell, "Metallic microlattice materials: A current state of the art on manufacturing, mechanical properties and applications," *Mater. Des.*, vol. 95, pp. 518–533, 2016.

[96] G. Dong, Y. Tang, and Y. F. Zhao, "A survey of modeling of lattice structures fabricated by additive manufacturing," *J. Mech. Des. Trans. ASME*, vol. 139, no. 10, 2017.

[97] X. Zheng *et al.*, "Ultralight, ultrastiff mechanical metamaterials," *Science (80-.).*, vol. 344, no. 6190, pp. 1373–1377, 2014.

[98] P. K. Misra, *Physics of Condensed Matter*. Elsevier, 2012.

[99] N. E. Mealy and M. Bayés, "Asm-8," *Drugs Future*, vol. 30, no. 1, p. 63, 2005.

[100] B. K. Nagesha, V. Dhinakaran, M. Varsha Shree, K. P. Manoj Kumar, D. Chalawadi, and T. Sathish, "Review on characterization and impacts of the lattice structure in additive manufacturing," *Mater. Today Proc.*, vol. 21, no. xxxx, pp. 916–919, 2020.

[101] M. McMillan, M. Jurg, M. Leary, and M. Brandt, "Programmatic Lattice Generation for Additive Manufacture," *Procedia Technol.*, vol. 20, no. January 2016, pp. 178–184, 2015.

[102] W. Tao and M. C. Leu, "Design of lattice structure for additive manufacturing," *Int. Symp. Flex. Autom. ISFA 2016*, no. August, pp. 325–332, 2016.

[103] J. Feng, J. Fu, Z. Lin, C. Shang, and B. Li, "A review of the design methods of complex topology structures for 3D printing," *Vis. Comput. Ind. Biomed. Art*, vol. 1, no. 1, pp. 1–

16, 2018.

[104] P. Jorge, *in Virtual and Physical*. .

[105] "Triply Periodic Minimal Surfaces." [Online]. Available: http://facstaff.susqu.edu/brakke/evolver/examples/periodic/periodic.html. [Accessed: 08-Jan-2021].

[106] R. Gümrük and R. A. W. Mines, "Compressive behaviour of stainless steel micro-lattice structures," *Int. J. Mech. Sci.*, vol. 68, pp. 125–139, 2013.

[107] D. W. Abueidda, M. Elhebeary, C. S. (Andrew) Shiang, S. Pang, R. K. Abu Al-Rub, and I. M. Jasiuk, "Mechanical properties of 3D printed polymeric Gyroid cellular structures: Experimental and finite element study," *Mater. Des.*, vol. 165, p. 107597, 2019.

[108] D. J. Yoo, "Computer-aided porous scaffold design for tissue engineering using triply periodic minimal surfaces," *Int. J. Precis. Eng. Manuf.*, vol. 12, no. 1, pp. 61–71, 2011.

[109] G. Dong, D. Tessier, and Y. F. Zhao, "Design of shoe soles using lattice structures fabricated by additive manufacturing," *Proc. Int. Conf. Eng. Des. ICED*, vol. 2019-Augus, no. August, pp. 719–728, 2019.

[110] K. Lee, "2008 International Symposium on Flexible Automation," vol. 2008, pp. 1–8, 2008.

[111] Y. M. Shabana, N. Noda, and K. Tohgo, "Elasto-Plastic Thermal Stresses in Functionally Graded Materials Considering Microstructure Effects," *Curr. Adv. Mech. Des. Prod. VII*, pp. 223–231, 2000.

[112] M. A. Wettergreen, B. S. Bucklen, B. Starly, E. Yuksel, W. Sun, and M. A. K. Liebschner, "Creation of a unit block library of architectures for use in assembled scaffold engineering," *CAD Comput. Aided Des.*, vol. 37, no. 11, pp. 1141–1149, 2005.

[113] S. Hyun, A. M. Karlsson, S. Torquato, and A. G. Evans, "Simulated properties of Kagomé and tetragonal truss core panels," *Int. J. Solids Struct.*, vol. 40, no. 25, pp. 6989–6998, 2003.

[114] M. Abdelhamid and A. Czekanski, "Impact of the lattice angle on the effective properties of the octet-truss lattice structure," *J. Eng. Mater. Technol. Trans. ASME*, vol. 140, no. 4, pp. 1747–1769, 2018.

[115] H. N. G. Wadley, "Multifunctional periodic cellular metals," *Philos. Trans. R. Soc. A Math. Phys. Eng. Sci.*, vol. 364, no. 1838, pp. 31–68, 2006.

[116] H. E. Pettermann and J. Hüsing, “Modeling and simulation of relaxation in viscoelastic open cell materials and structures,” *Int. J. Solids Struct.*, vol. 49, no. 19–20, pp. 2848–2853, 2012.

[117] I. Maskery, A. O. Aremu, L. Parry, R. D. Wildman, C. J. Tuck, and I. A. Ashcroft, “Effective design and simulation of surface-based lattice structures featuring volume fraction and cell type grading,” *Mater. Des.*, vol. 155, pp. 220–232, 2018.

[118] Y. Wang, “Periodic surface modeling for computer aided nano design,” *CAD Comput. Aided Des.*, vol. 39, no. 3, pp. 179–189, 2007.

[119] J. C. Dinis *et al.*, “Open Source Software for the Automatic Design of Scaffold Structures for Tissue Engineering Applications,” *Procedia Technol.*, vol. 16, pp. 1542–1547, 2014.

[120] “Body Centered Cubic Structure (BCC) | MATSE 81: Materials In Today’s World.” [Online]. Available: https://www.e-education.psu.edu/matse81/node/2132. [Accessed: 17-Sep-2020].

[121] P. Platek, J. Sienkiewicz, J. Janiszewski, and F. Jiang, “Investigations on mechanical properties of lattice structures with different values of relative density made from 316L by selective laser melting (SLM),” *Materials (Basel).*, vol. 13, no. 9, 2020.

[122] M. Ross, “Schwarz’ P and D surfaces are stable,” *Differ. Geom. its Appl.*, vol. 2, no. 2, pp. 179–195, 1992.

[123] M. Iqbal Mohammed, “Design and fabrication considerations for three dimensional scaffold structures,” *KnE Eng.*, vol. 2, no. 2, p. 120, 2017.

[124] J. Shin *et al.*, “Finite element analysis of Schwarz P surface pore geometries for tissue-engineered scaffolds,” *Math. Probl. Eng.*, vol. 2012, no. June 2015, 2012.

[125] “Neovius_surface @ wikivisually.com.” .

[126] Robert Ferreol, “Neovius surface,” 2017. [Online]. Available: https://mathcurve.com/surfaces.gb/neovius/neovius.shtml. [Accessed: 17-Sep-2020].

[127] F. N. Habib, P. Iovenitti, S. H. Masood, and M. Nikzad, “Fabrication of polymeric lattice structures for optimum energy absorption using Multi Jet Fusion technology,” *Mater. Des.*, vol. 155, no. 2017, pp. 86–98, 2018.

[128] I. Maskery *et al.*, “An investigation into reinforced and functionally graded lattice structures,” *J. Cell. Plast.*, vol. 53, no. 2, pp. 151–165, 2017.

[129] M. F. Ashby, “The properties of foams and lattices,” *Philos. Trans. R. Soc. A Math. Phys.*

Eng. Sci., vol. 364, no. 1838, pp. 15–30, 2006.

[130] M. Leary *et al.*, "Inconel 625 lattice structures manufactured by selective laser melting (SLM): Mechanical properties, deformation and failure modes," *Mater. Des.*, vol. 157, no. 2017, pp. 179–199, 2018.

[131] L. Warnet and P. E. Reed, "Falling Weight Impact Testing Principles," pp. 66–70, 1999.

[132] A. Beharic, R. Rodriguez Egui, and L. Yang, "Drop-weight impact characteristics of additively manufactured sandwich structures with different cellular designs," *Mater. Des.*, vol. 145, no. 2017, pp. 122–134, 2018.

[133] R. S. Lakes, "Cellular solids," *Journal of Biomechanics*, vol. 22, no. 4. p. 397, 1989.

[134] I. Maskery *et al.*, "Insights into the mechanical properties of several triply periodic minimal surface lattice structures made by polymer additive manufacturing," *Polymer (Guildf).*, vol. 152, pp. 62–71, 2018.

[135] A. S. Dalaq, D. W. Abueidda, and R. K. Abu Al-Rub, "Mechanical properties of 3D printed interpenetrating phase composites with novel architectured 3D solid-sheet reinforcements," *Compos. Part A Appl. Sci. Manuf.*, vol. 84, pp. 266–280, 2016.

[136] C. Yan, L. Hao, A. Hussein, and P. Young, "Ti-6Al-4V triply periodic minimal surface structures for bone implants fabricated via selective laser melting," *J. Mech. Behav. Biomed. Mater.*, vol. 51, pp. 61–73, 2015.

[137] C. Yan, L. Hao, A. Hussein, P. Young, J. Huang, and W. Zhu, "Microstructure and mechanical properties of aluminium alloy cellular lattice structures manufactured by direct metal laser sintering," *Mater. Sci. Eng. A*, vol. 628, pp. 238–246, 2015.

[138] K. Ushijima, W. J. Cantwell, R. A. W. Mines, S. Tsopanos, and M. Smith, "An investigation into the compressive properties of stainless steel micro-lattice structures," *J. Sandw. Struct. Mater.*, vol. 13, no. 3, pp. 303–329, 2011.

[139] S. N. Khaderi, V. S. Deshpande, and N. A. Fleck, "The stiffness and strength of the gyroid lattice," *Int. J. Solids Struct.*, vol. 51, no. 23–24, pp. 3866–3877, 2014.

[140] G. Maliaris, I. T. Sarafis, T. Lazaridis, A. Varoutoglou, and G. Tsakataras, "Random lattice structures. Modelling, manufacture and FEA of their mechanical response," *IOP Conf. Ser. Mater. Sci. Eng.*, vol. 161, no. 1, 2016.

[141] A. Seharing, A. H. Azman, and S. Abdullah, "A review on integration of lightweight gradient lattice structures in additive manufacturing parts," *Adv. Mech. Eng.*, vol. 12, no. 6, pp. 1–21, 2020.

[142] C. Borsellino and G. Di Bella, “Paper-reinforced biomimetic cellular structures for automotive applications,” *Mater. Des.*, vol. 30, no. 10, pp. 4054–4059, 2009.

[143] E. Frulloni, J. M. Kenny, P. Conti, and L. Torre, “Experimental study and finite element analysis of the elastic instability of composite lattice structures for aeronautic applications,” *Compos. Struct.*, vol. 78, no. 4, pp. 519–528, 2007.

[144] Z. Ozdemir *et al.*, “Energy absorption in lattice structures in dynamics: Experiments,” *Int. J. Impact Eng.*, vol. 89, pp. 49–61, 2016.

[145] D. W. Abueidda, M. Bakir, R. K. Abu Al-Rub, J. S. Bergström, N. A. Sobh, and I. Jasiuk, “Mechanical properties of 3D printed polymeric cellular materials with triply periodic minimal surface architectures,” *Mater. Des.*, vol. 122, pp. 255–267, 2017.

[146] S. Singh, A. Sachdeva, and V. S. Sharma, “Investigation of Dimensional Accuracy/Mechanical Proper- ties of Part Produced by Selective Laser Sintering,” *Int. J. Appl. Sci. Eng. Int. J. Appl. Sci. Eng*, vol. 10, no. 10, pp. 59–68, 2012.

[147] Q. Wang, Z. Yang, Z. Lu, and X. Li, “Mechanical responses of 3D cross-chiral auxetic materials under uniaxial compression,” *Mater. Des.*, vol. 186, p. 108226, 2020.

[148] W. A. Y. Yusoff, D. T. Pham, and K. D. Dotchev, “The Impact of Employing Different Quality PA2200 Powder Grades to Shrinkage on Sintered Part in Selective Laser Sintering Process,” *Appl. Mech. Mater.*, vol. 789–790, pp. 126–130, 2015.

[149] S. Gümüs *et al.*, “Failure behavior of PA12 based SLS lattice structure with macro-porosity,” *MATEC Web Conf.*, vol. 188, 2018.

[150] L. Bai *et al.*, “Mechanical properties and energy absorption capabilities of functionally graded lattice structures: Experiments and simulations,” *Int. J. Mech. Sci.*, vol. 182, no. April, p. 105735, 2020.

[151] A. C. Lopes, Á. M. Sampaio, C. S. Silva, and A. J. Pontes, “Study and evaluation of different combinations of virgin and processed PA material for Selective Laser Sintering technology,” *8th Int. Conf. Polym. Mould. Innov.*, 2018.

[152] Q. M. Li, I. Magkiriadis, and J. J. Harrigan, “Compressive strain at the onset of densification of cellular solids,” *J. Cell. Plast.*, vol. 42, no. 5, pp. 371–392, 2006.

APPENDICES

APPENDIX 1: Relative densities of each variable independent parameter of unit cell.

APPENDIX 1.A

	Body Centered Cubic (BCC)								
	Lattice parameters			Unit cell			Overall structure		
	Shell thickness [mm]	Strut diameter [mm]	Cell size (WxDxH) [mm]	Lattice mass [mm³]	Density [%]	Relative density [%]	Lattice mass [mm³]	Density [%]	Relative density [%]
BR	1	2,00	10 x 10 x 10	18	18	19	25634	20	22
Parameter: strut diameter									
BT1	1	1,70	10 x 10 x 10	133	13	14	19927	16	17
BT2	1	2,30	10 x 10 x 10	228	23	25	31889	25	27
Parameter: cell size									
BC1	1	2,66	13,33 x 13,33 x 13,33	421	18	19	25549	20	21
BC2	1	3,99	20 x 20 x 20	1421	18	19	25610	20	22
Parameter: shell thickness									
BS1	0	2,00	10 x 10 x 10	178	18	19	22843	18	19
BS2	2	2,00	10 x 10 x 10	178	18	19	28174	22	24

APPENDIX 1.B

	Schwarz-P (P)								
	Lattice parameters			Unit cell			Overall structure		
	Shell thickness [mm]	Surface thickness [mm]	Cell size (WxDxH) [mm]	Lattice mass [mm³]	Density [%]	Relative density [%]	Lattice mass [mm³]	Density [%]	Relative density [%]
PR	1	0,76	10 x 10 x 10	177	18	19	25492	20	21
Parameter: surface thickness									
PT1	1	0,57	10 x 10 x 10	133	13	14	19956	16	17
PT2	1	0,98	10 x 10 x 10	228	23	25	31840	25	27
Parameter: cell size									
PC1	1	1,02	13,33 x 13,33 x 13,33	423	18	19	25631	20	22
PC2	1	1,52	20 x 20 x 20	1419	18	19	25517	20	21
Parameter: shell thickness									
PS1	0	0,76	10 x 10 x 10	177	18	19	22706	18	19
PS2	2	0,76	10 x 10 x 10	177	18	19	28140	22	24

APPENDIX 1.C

	Neovius (N)								
	Lattice parameters			Unit cell			Overall structure		
	Shell thickness [mm]	Surface thickness [mm]	Sell size (WxDxH) [mm]	Lattice mass [mm³]	Density [%]	Relative density [%]	Lattice mass [mm³]	Density [%]	Relative density [%]
NR	1	0,51	10 x 10 x 10	178	18	19	25441	20	21
Parameter: surface thickness									
NT1	1	0,38	10 x 10 x 10	134	13	14	19380	15	16
NT2	1	0,65	10 x 10 x 10	227	23	24	31467	25	26
Parameter: cell size									
NC1	1	0,68	13,33 x 13,33 x 13,33	423	18	19	25536	20	21
NC2	1	1,02	20 x 20 x 20	1429	18	19	25635	20	22
Parameter: shell thickness									
NS1	0	0,51	10 x 10 x 10	178	18	19	22812	18	19
NS2	2	0,51	10 x 10 x 10	178	18	19	28047	22	24

APPENDIX 2: PA 2200 Balance 1.0 Datasheet.

e-Manufacturing Solutions

PA 2200 Balance 1.0

PA12 — EOS GmbH - Electro Optical Systems

Product Texts

Product Texts

This whitish fine powder PA 2200 on the basis of polyamide 12 serves with its very well-balanced property profile a wide variety of applications. Laser-sintered parts made from PA 2200 possess excellent material properties:

- high strength and stiffness
- good chemical resistance
- excellent long-term constant behaviour
- high selectivity and detail resolution
- various finishing possibilities (e.g. metallisation, stove enamelling, vibratory grinding, tub colouring, bonding, powder coating, flocking)
- bio compatible according to EN ISO 10993-1 and USP/level VI/121 °C
- approved for food contact in compliance with the EU Plastics Directive 2002/72/EC (exception: high alcoholic foodstuff)

Typical applications of the material are fully functional plastic parts of highest quality. Due to the excellent mechanical properties the material is often used to substitute typical injection moulding plastics. The biocompatibility allows its use e.g. for prostheses, the high abrasion resistance allows e.g. the realisation of movable part connections.

120 µm layer thickness
The advantage of the Balance parameter set is equilibrium. The layer thickness of 120 µm offers a perfect balance between production costs, mechanical properties, surface quality and accuracy. It is therefore suitable for parts with varying geometries, dimensions and requirements.

Mechanical properties	Value	Unit	Test Standard
Izod Impact notched (23°C)	**4.4**	kJ/m²	ISO 180/1A
Shore D hardness (15s)	**75**	-	ISO 7619-1

3D Data	Value	Unit	Test Standard
The properties of parts manufactured using additive manufacturing technology (e.g. laser sintering, stereolithography, Fused Deposition Modelling, 3D printing) are, due to their layer-by-layer production, to some extent direction dependent. This has to be considered when designing the part and defining the build orientation.			
Tensile Modulus			ISO 527-1/-2
X Direction	**1650**	MPa	
Y Direction	**1650**	MPa	
Z Direction	**1650**	MPa	
Tensile Strength			ISO 527-1/-2
X Direction	**48**	MPa	
Y Direction	**48**	MPa	
Z Direction	**42**	MPa	
Strain at break			ISO 527-1/-2
X Direction	**18**	%	
Y Direction	**18**	%	
Z Direction	**4**	%	
Charpy impact strength (+23°C, X Direction)	**53**	kJ/m²	ISO 179/1eU
Charpy notched impact strength (+23°C, X Direction)	**4.8**	kJ/m²	ISO 179/1eA
Flexural Modulus (23°C, X Direction)	**1500**	MPa	ISO 178

Thermal properties	Value	Unit	Test Standard
Melting temperature (20°C/min)	**176**	°C	ISO 11357-1/-3
Vicat softening temperature (50°C/h 50N)	**163**	°C	ISO 306
Burning behavior			UL 94
Test passed, HB	**0.5**	mm	
Test passed, HB	**1.6**	mm	
Test passed, HB	**3.2**	mm	

Other properties	Value	Unit	Test Standard
Density (lasersintered)	**930**	kg/m³	EOS Method
Powder colour (ac. to safety data sheet)	**White**	-	-

Characteristics

Processing
Laser Sintering, Rapid Prototyping

Chemical Resistance
General Chemical Resistance

Certifications
FDA approval acc. to USP Biological test (classification VI/121°C)

APPENDIX 3: Technical Data of EOS P 396 machine.

EOS P 396

Reliable Production with the Industry's Largest Material Portfolio

The medium-sized bestselling EOS P 396 enables a flexible and tool-free production of everything from spare parts on-demand, to serial production.

- All 3D printed parts with excellent mechanical properties and dimensional accuracy due to software features such as Smart Scaling, EOSAME and a continuous temperature monitoring.
- Highest productivity ensured by its powerful laser plus high scanning and recoating speed.
- A multitude of applications that fully meet industry requirements is possible with the 14 materials and their 26 parameter sets.
- Full integration into the IIoT environment with EOSCONNECT Core resulting in an entirely digital process chain from the CAD model, through ERP and MES connection, to the finished part.
- Maximum machine park uptime with digital track and trace from everywhere and at any time.
- Continuous optimization of the entire production workflow made possible with the evaluation and documentation of all build cycles.

Technical Data EOS P 396

* for PA 2200 at 120 µm layer thickness and 5% nesting density

Building volume	340 x 340 x 600 mm (13.4 x 13.4 x 23.6 in)
Laser type	CO_2; 70 W
Building rate	up to 3,0 l/h*
Layer thickness (depending on material)	0.06 – 0.10 – 0.12 – 0.15 – 0.18 mm (0.0024 - 0.0039 - 0.0047 - 0.0059 - 0.0071 in)
Precision optics	F-theta lens, high-speed scanner
Scan speed during build process	up to 6 m/s (19.7 ft/s)
Power supply	400 V / 32 A, max. power supply 16 A
Power consumption	typical 2.1 kW; maximum 10 kW
Dimensions (W x D x H)	1 840 x 1 175 x 2 100 mm (72.4 x 46.3 x 82.7 in)
Recommended installation space	ca. 4.3 x 3.9 x 3.0 m (169.3 x 153.5 x 118.1 in)
Weight	ca. 1 060 kg (2 337 lb)

Software

PSW 3.8, EOSCONNECT (open interface OPC-UA, Web API), Smart Scaling

Materials

PA 1101, PA 1102 black, PA 2200, PA 2201, PA 2210 FR, PrimePart FR (PA 2241 FR), PA 3200 GF, Alumide, EOS TPU 1301, PP 1101, PrimeCast 101, ALM FR-106, ALM HP 11-30, ALM PA 640 GSL

Optional Accessories

IPCM P plus, Big Bag emptying station, unpack- and sieving station, blasting cabinet